A STUDY OF INELASTIC EFFECTS IN NUCLEON PICKUP REACTIONS ON ^{24}MG AND THE STRUCTURE OF ^{23}NA AND ^{23}MG

by

Ronald Orville Nelson

Department of Physics
Duke University

Date: 21 Dec 1971

Approved:

N. Russell Roberson, Supervisor

J. Sykes

A dissertation submitted in partial fulfillment of the requirements for the degree of Doctor of Philosophy in the Department of Physics in the Graduate School of Arts and Sciences of Duke University

1971

ABSTRACT

(Physics)

A STUDY OF INELASTIC EFFECTS IN NUCLEON PICKUP REACTIONS ON ^{24}MG AND THE STRUCTURE OF ^{23}NA AND ^{23}MG

by

Ronald Orville Nelson

Department of Physics
Duke University

Date: _____

Approved:

_____
N. Russell Roberson, Supervisor

_____

_____

_____

_____

An abstract of a dissertation submitted in partial fulfillment of the requirements for the degree of Doctor of Philosophy in the Department of Physics in the Graduate School of Arts and Sciences of Duke University

1971

A STUDY OF INELASTIC EFFECTS IN NUCLEON PICKUP REACTIONS ON ^{24}MG AND THE STRUCTURE OF ^{23}NA AND ^{23}MG

by

Ronald Orville Nelson

Thirteen states of ^{23}Na with excitation energies < 5.5 MeV and their analog states in ^{23}Mg have been studied with the ^{24}Mg(d, ^{3}He)^{23}Na and ^{24}Mg(d,t)^{23}Mg reactions at the deuteron bombarding energy of 21.1 MeV. From a Coupled-Channel Born Approximation (CCBA) analysis of the angular distributions, it was possible to identify mirror states of the nuclei and to establish for ^{23}Mg spin and parity assignments of $^{9}/_{2}^{+}$, $^{3}/_{2}^{+}$, $(^{5}/_{2}^{+})$, $(^{5}/_{2}^{-})$, $(^{7}/_{2}^{+})$ and $(^{5}/_{2}^{+})$ for the levels at 2.71, 2.90, 3.86, 3.97, 4.68 and 5.29 MeV, respectively.

Initial attempts to fit the distributions with the Distorted Wave Born Approximation (DWBA) could not reproduce the pronounced differences observed between known $\ell = 2$ angular distributions. A subsequent measurement of the differential cross section for inelastic scattering for 21.1-MeV deuterons on

^{24}Mg revealed that at back angles the inelastic cross sections were frequently greater than the cross section for elastic scattering. Since this fact violates the assumption of DWBA theory that elastic scattering is the predominant interaction process, a CCBA analysis was performed explicitly including effects from inelastic scattering.

The calculations of the present study imply that the experimental angular distribution for the ^{24}Mg(d,^{3}He) and ^{24}Mg(d,t) reactions are generally consistant with a Nilsson strong-coupling model of ^{23}Na and ^{23}Mg if band-mixing is included. This conclusion is critically dependent on the inclusion of inelastic effects without which agreement with the data is not possible.

ACKNOWLEDGEMENTS

I wish to express my gratitude to my advisor, Dr. N. R. Roberson, for his interest and support during my graduate career. I am also indebted to Dr. T. G. Dzubay for his assistance in data collection for many helpful discussions. I also wish to thank Dr. C. R. Gould for his assistance in data collection.

I extend my appreciation to Drs. T. Tamura and T. Udagawa for supplying me with copies of their coupled-channel Born approximation computer code, and to the latter a special thanks for several helpful conversations. I wish to thank Dr. W. J. Thompson for his enlightening discussions of the reaction theory. I also wish to thank Dr. J. R. Erskine for sending a copy of his bandmixing code. I extend my appreciation to Mr. R. A. Hilko for his assistance in data collection and for helpful discussions concerning the analysis. I wish to thank the entire technical staff for assistance with the accelerator and electronic systems. I am grateful to Dr. H. W. Newson and Dr. E. G. Bilpuch for providing me with the research assistantship.

Special thanks are extended to my wife, Merrell, for her continued encouragement and assistance in preparing the illustrations. I also wish to thank my parents for their encouragement.

This work was supported in part by the U. S. Atomic Energy Commission.

R. O. N.

CONTENTS

LIST OF FIGURES

LIST OF TABLES

A STUDY OF INELASTIC EFFECTS IN NUCLEON PICKUP REACTIONS ON ^{24}MG AND THE STRUCTURE OF ^{23}NA AND ^{23}MG

Chapter I

INTRODUCTION

Although the collective model was originally proposed to describe heavy deformed nuclei (Bohr, 1952; Bohr and Mottelson, 1953; Nilsson, 1955), it has been used to interpret the properties of sd-shell nuclei as well. The great volume of experimental data accumulated and compared with the model predictions indicate that while generally less successful for light nuclei, the collective model does provide a reasonable description of the low-lying levels within these nuclei. This is particularly true for nuclei with mass A in the region $19 \leq A \leq 25$.

Within this region the mirror nuclei ^{23}Na and ^{23}Mg, have been subjects of much experimental work. Using the ^{24}Mg(^{3}He, α)^{23}Mg reaction, Dubois et al. (1967[b]) and Haun et al. (1970) have performed angular distribution measurements and particle-gamma angular correlations to obtain assignments (or limits) of spins and parities for 11 states in ^{23}Mg. These studies revealed an energy spectrum which could be interpreted as rotational bands built upon single-particle states as described by the Nilsson model (see Chapter IV).

Comparisons of the $^{E2}/_{M1}$ mixing ratios and branching ratios for γ-transitions within the ground-state band with those predicted by the model gave good agreement. However, this simple model failed to describe the interband transitions. Dubois (1968) and Kanestrøm (1971) have shown that these transitions may be explained within the collective model if bandmixing and isospin effects are treated properly.

Spectroscopic factors for single nucleon transfers to ^{23}Mg have been measured using the (^{3}He, α) reaction at 15.0 MeV (J. M. Joyce et al., 1969) and the (p,d) reaction at 33.6 MeV (R. L. Kozub, 1968).

Considerably more experimental investigations have been performed for the ^{23}Na nucleus. Employing the ^{22}Ne (^{3}He,d)^{23}Na reaction at 10 and 12 MeV, Dubois (1967[a]) determined the angular momentum transfers (ℓ-values) and spectroscopic factors for many states below 7.0 MeV. All states below 5.5 MeV were tentatively identified as members of various mixed rotational bands. Dubois found that bandmixing was necessary to give agreement of the Nilsson model with the experimental energy spectrum. However, the spectroscopic factors from his calculations were not in agreement with some of the measured values. Recently J. R. Powers et al. (1971) have repeated this experiment at 15 MeV and obtained essentially the same spectroscopic factors indicating some difficulty for the model.

Using the ^{24}Mg(t, $\alpha\gamma$)^{23}Na reaction for angular correlation measurements, A. R. Poletti et al. (1970) recently made spin and parity assignments for the states between 2.5 and 5.8 MeV. Only a few assignments for higher states remain tentative. After combining results for the correlation experiment

and previous lifetime measurements (A. R. Poletti et al., 1969), comparisons of the transition strengths in the ground-state band with the results of a Nilsson model calculation without bandmixing indicated reasonable agreement.

Since the applicability of the Nilsson model for the mass-23 mirror nuclei required further investigation and since uncertainties remained as to spin and parity assignments for several levels between 3.0 and 5.5 MeV in ^{23}Mg, the present work was undertaken to study both mirror nuclei in one experiment utilizing the (d, ^{3}He) and (d,t) reactions on ^{24}Mg. If the kinematics for these reactions do not differ greatly, then the angular distributions for reactions populating mirror states should have similar shapes (M. Gaillard et al., 1968 and T. G. Dzubay et al., 1971). Direct identification of mirror states below 3 MeV in excitation energy was possible on this basis. Other mirror states were identified through comparisons of the data with the predictions of the coupled-channel Born approximation (CCBA). The establishment of mirror pairs enabled the known spins and parities of ^{23}Na to be applied in ^{23}Mg.

The CCBA treatment (S. K. Penny et al., 1964; R. J. Ascuitto et al., 1969) of nucleon transfer reactions includes inelastic effects ignored by the usual distorted-wave Born approximation (DWBA). The enhanced inelastic scattering of projectiles from strongly overlapping states within a collective nucleus create what may be pictured as an excited target. Subsequent nucleon transfer reactions combined with the inelastic scattering give rise to angular momentum transfers which may populate levels forbidden to the direct reaction. In practice these two-step processes were also found to be important in the population

of many states where the direct reaction was allowed. Consequently, the information extracted from a DWBA analysis may differ from that of the CCBA analysis. It is believed the latter analysis will provide a more reliable means to evaluate the spectroscopic factors predicted by the Nilsson model.

Since this study was begun, E. Krämer et al. (1971) and M. Arditi et al. (1971) have completed studies of the $^{24}Mg(d, ^{3}He)^{23}Na$ reaction at deuteron energies of 52 and 82 MeV, respectively. Thus, it is possible to compare the spectroscopy derived from the CCBA calculation for the 21-MeV data with results obtained from the usual DWBA analysis of data taken at higher energies where inelastic effects are thought to be less important (S. K. Penny, 1964).

Chapter II

EXPERIMENTAL APPARATUS AND PROCEDURE

A. Ion Beams

The deuteron beams employed for the differential cross section measurements of this study were obtained from the Triangle Universities Nuclear Laboratory Cyclo-Graaff accelerator (F. O. Purser et al., 1969). Negative 8-MeV D^- ions were produced in a cyclotron and were further accelerated by a FN tandem. After acceleration the beam was momentum analyzed by a switching magnet. At the exit of the magnet, adjustable verticle and horizontal slits defined the beam and limited the beam currents on the slits in the chamber. The beam then passed down the beam tube through a combination of steering magnets and magnetic quadrupole lenses and into the 60 cm scattering chamber.

The time structure associated with a beam burst was monitored through the time delay between the zero-crossing of the cyclotron dee voltage and the detection of gamma rays with a plastic scintillator located near the Faraday cup. Knowledge of this structure allowed adjustment of the cyclotron parameters to minimize the energy spread of the extracted ions. During most of the measure-

ments, the beam spread was believed to be < 15 keV.

Helium beams for the elastic scattering cross section measurements were obtained by inflecting 40-keV $^{3}He^{-}$ or $^{4}He^{-}$ ions from the negative ion source into the FN tandem.

B. Target Chamber

All angular distribution measurements were performed in a 60 cm scattering chamber. Since this chamber has been discussed elsewhere (W. McEver, 1970) only the most important features are mentioned here.

The internal diameter and depth are 60 cm and 13 cm, respectively. Two independently rotating tables have tracks for detector mounts placed at 20° increments. The tracks may be cooled by a Freon refrigeration system. Angular scales marked at the rim of each table are read with a vernier to $\pm 0.05^{\circ}$.

The target ladder for the scattering chamber has positions for five targets mounted on 1.9 cm diameter rings. The ladder system is designed so that either the targets may be stored, without damage, in a vacuum while the detector setup is modified, or the target ladder may be removed leaving the detectors undisturbed.

Beam collimation for the chamber consists of adjustable horizontal and vertical slits 93 cm in front of the chamber wall and insulated slits at the end of a snout whose distance from the target is adjustable. This distance was set at 15 cm for these measurements. Currents from each side of the two slits

in the snout are monitored by an automatic steering circuit which minimizes beam currents on the slits. An anti-scattering slit is located 5 cm beyond the insulated slits.

After passing through the target, the beam is stopped in a tantalum-lined Faraday beam cup located 4 m beyond the chamber wall. The Faraday cup and 3 m of adjacent beam line are electrically insulated from the chamber and are used for beam charge collection and integration. Shielding is provided by a water filled tank which surrounds the Faraday cup.

C. Targets

The magnesium-24 targets were prepared using MgO (with 99.96% enrichment) purchased from the Isotopes Division of the Oak Ridge National Laboratory. During evaporation from a Ta boat the oxide was partially reduced by an admixture of Ta powder. The magnesium was deposited on glass slides coated with a carbon film with a thickness of $\sim 10\ \mu g/cm^2$. The composite foils were floated from the slides in a water bath and mounted on stainless steel target rings. Using the surface tension of a water droplet suspended between a piece of cotton and the carbon backing, the carbon was fragmented and separated from the magnesium target. A few self-supporting targets were produced in this way. With a 4.0-MeV alpha-particle beam, the target thickness was determined from comparisons of the elastic scattering cross section with Rutherford scattering predictions. These measurements were based on data at forward angles where the assumption of Rutherford scattering is most valid. A typical target

was 400 $\mu g/cm^2$ thick in ^{24}Mg.

D. Particle Detectors

Silicon surface-barrier detectors were used throughout this study for charged particle detection. They offered excellent resolution, long term stability and small size. Since the detectors were operated in a high radiation environment, silicon surface-barrier devices were preferred to silicon lithium-drifted detectors which show greater sensitivity to radiation damage.

For data collection the detectors were placed in detector mounts which were attached to the Freon-cooled tracks in the chamber. Thermal conduction through the mounts cooled the detectors which reduced the electronic noise from these devices. With the detectors cooled and biased at the rated voltages, the intrinsic resolution of the system for alpha-particles emitted by an ^{241}Am source was determined to be $\sim$25 keV FWHM.

Except for the elastic scattering of alpha beams, all data in this study required particle identification. This was accomplished through use of counter telescopes consisting of a thin totally-depleted transmission ΔE detector and a thick totally-depleted E detector. The ΔE detectors were chosen to be as thick as possible without stopping the least energetic particles of interest. For the (d, ^3He) reactions and the ^3He elastic scattering distributions the telescopes employed ΔE detectors with thickness $\leq 50\,\mu m$ and E detectors with thickness 1500 to 2000 μm. Cross section measurements of deuteron elastic scattering by ^{24}Mg at 21 MeV required thicker ΔE detectors (200 μm). The

larger pulses provided more accurate mass identification of the deuterons.

A 2000 μm partially-depleted surface barrier detector was used at a fixed angle during data collection to check the beam integration and monitor the target composition. This detector did not require cooling.

E. Electronics

The block diagram of the electronic apparatus is shown in fig. 1. For each telescope the ΔE (E) signals shown in fig. 1(a) originated in the totally-depleted transmission detectors, passed through separate charge sensitive pre-amplifiers and through separate linear amplifiers. The prompt bipolar output pulses were sent to a timing single channel analyzer which gave outputs suitable for a slow (micro-second) coincidence. A ΔE - E coincidence generated both a gate for the linear pulse stretchers and a logic pulse for the router. The de-layed amplifier outputs for ΔE (E) signals passed through separate stretchers where delay and output pulse width adjustments were used to match the ΔE - E pulses before summing.

The ΔE, E and routing signals produced by each telescope were pro-cessed as shown in fig. 1(b). Since the small pulses from the thin ΔE detector required more amplification to exceed the minimum pulse height discriminator of the timing single channel analyzers, the ΔE pulses were attenuated after mixing. After attenuation the ΔE signals were fanned out, one part was sent through an amplifier straight to an analog to digital converter (ADC), while the

Figure 1. Block diagram of the particle identification electronic setup. Part (a) indicates what apparatus is necessary for each counter telescope. For each coincident event energy pulses, E_n and ΔE_n, and a routing pulse, R_n, are sent from (a) into the mixing circuit illustrated in (b). This circuit stores in the computer a binary number representing the ΔE and full-energy ($E + \Delta E$) pulses and identification information from the router. The computer is programmed to identify the particle from the ΔE and $E + \Delta E$ inputs and store the event (see Appendix A). Also shown in the figure is the pulse processing system for the monitor detector.

(a)

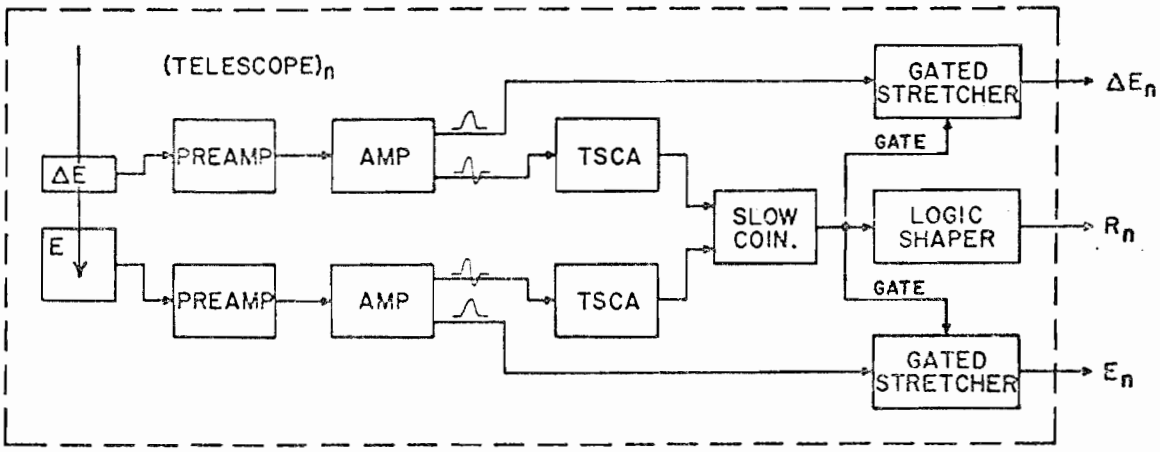
(TELESCOPE)n
ΔE
E
PREAMP
PREAMP
AMP
AMP
TSCA
TSCA
SLOW COIN.
GATED STRETCHER
GATE
LOGIC SHAPER
GATE
GATED STRETCHER
ΔEn
Rn
En

(b)

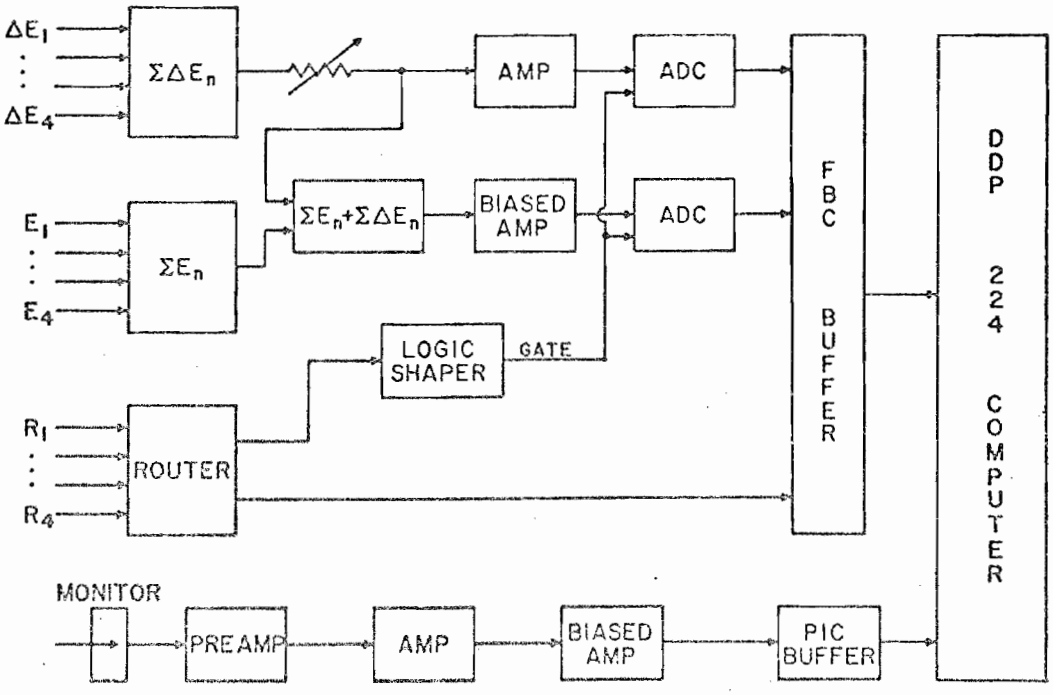
ΔE1
ΔE4
ΣΔEn
AMP
ADC
E1
E4
ΣEn
ΣEn+ΣΔEn
BIASED AMP
ADC
LOGIC SHAPER
GATE
R1
R4
ROUTER
FBC BUFFER
DDP 224 COMPUTER
MONITOR
PREAMP
AMP
BIASED AMP
PIC BUFFER

other was summed with the mixed E signals yielding full-energy E + ΔE pulses. These pulses were sent through a biased amplifier to another ADC.

The routing pulses went to a device which identified the detector telescope in which the coincidence event occurred. This router also generated a gate signal used to enable pulse height analysis at the ΔE and E + ΔE ADC's. Binary numbers produced by these ADC's and the router were transferred into a 24 bit buffer in the computer interface and inserted into the memory of the computer by a fully buffered channel (FBC).

The on-line computer, a DDP-224, was programmed to allow options for singles storage of either ΔE or E + ΔE signals, particle identification with mass storage or energy storage for selected mass groups (J. M. Joyce et al., 1969). Detailed descriptions of the on-line programs are given in Appendix A. Spectra accumulated during a run were recorded on magnetic tape for off-line analysis at a later time. An option for buffered-tape storage of all or selected masses enabled off-line accumulation of energy spectra for particle groups not selected during an on-line run, changes in the range table used in particle identification and energy dependent mass windows for particle groups.

During data collection the beam was integrated by an electronic current indicator and integrator. For each unit of charge collected, a pulse was generated and counted on three separate scalers. One of these scalers was gated off while the FBC was busy analyzing events from the telescopes, and thus it recorded the live charge for the FBC. Similarly, using the parallel input channel (PIC) busy signal, another scaler measured live charge for the monitor while the third scaler simply counted all pulses from the current integrator.

The ratios of total charge to live charge were used to correct the spectra for dead-time counting losses. A fourth scaler was used as a timer. At the end of each run, these four scalers were read into the computer and written on magnetic tape along with the other data.

For the cross section measurements at angles forward of 15^{o}, the electronic apparatus was modified to improve the mass and energy spectra and to give a more accurate measure of the dead-time in the pulse processing system. At these angles the elastic scattering increased the count rate so that, to obtain good energy resolution, pile-up rejection was used to eliminate events occuring in the interval between 200 ns and 30 μs after a previous event. This rejection system introduced dead-time not measured in the system discussed above, and it was necessary to use a technique developed by H. Bolotin et al. (1970) which determined the counting losses for the entire system.

The block diagram for the electronics in fig. 2 shows that only one particle telescope was used and that it differed from those of fig. 1 in three ways: (1) pulses at the input of the ΔE and E preamps came from a pulser as well as the detector, (2) signals from the E preamp were divided and sent through both a fast timing amplifier and a linear amplifier, and (3) a pile-up event detected in the E signal would veto the coincidence. To measure the dead time of the system, pulses from nuclear events were counted, and for each 100 events a delayed test pulse was sent to the ΔE and E preamps. The delay insured that the test pulse would be inserted in random sequence with respect to the nuclear events. The pulser signals underwent the same processing and were subjected to the same counting losses as the nuclear events. Since the

Figure 2. Block diagram of circuit used for accurate determination of dead-time loses in a counter telescope system with pile-up rejection. For every 100 pulses produced by nuclear events in the E detector, one E-ΔE pair of pulses was inserted into the counter system. A delay of $\sim$300 μs insured that these pulses were entered in random sequence with respect to nuclear events. Output signals from this telescope were fed into the mixing circuit of fig. 2(b). The dead-time of the system was the fraction of test pulses that were generated and sent to the preamplifiers but were not stored in the computer.

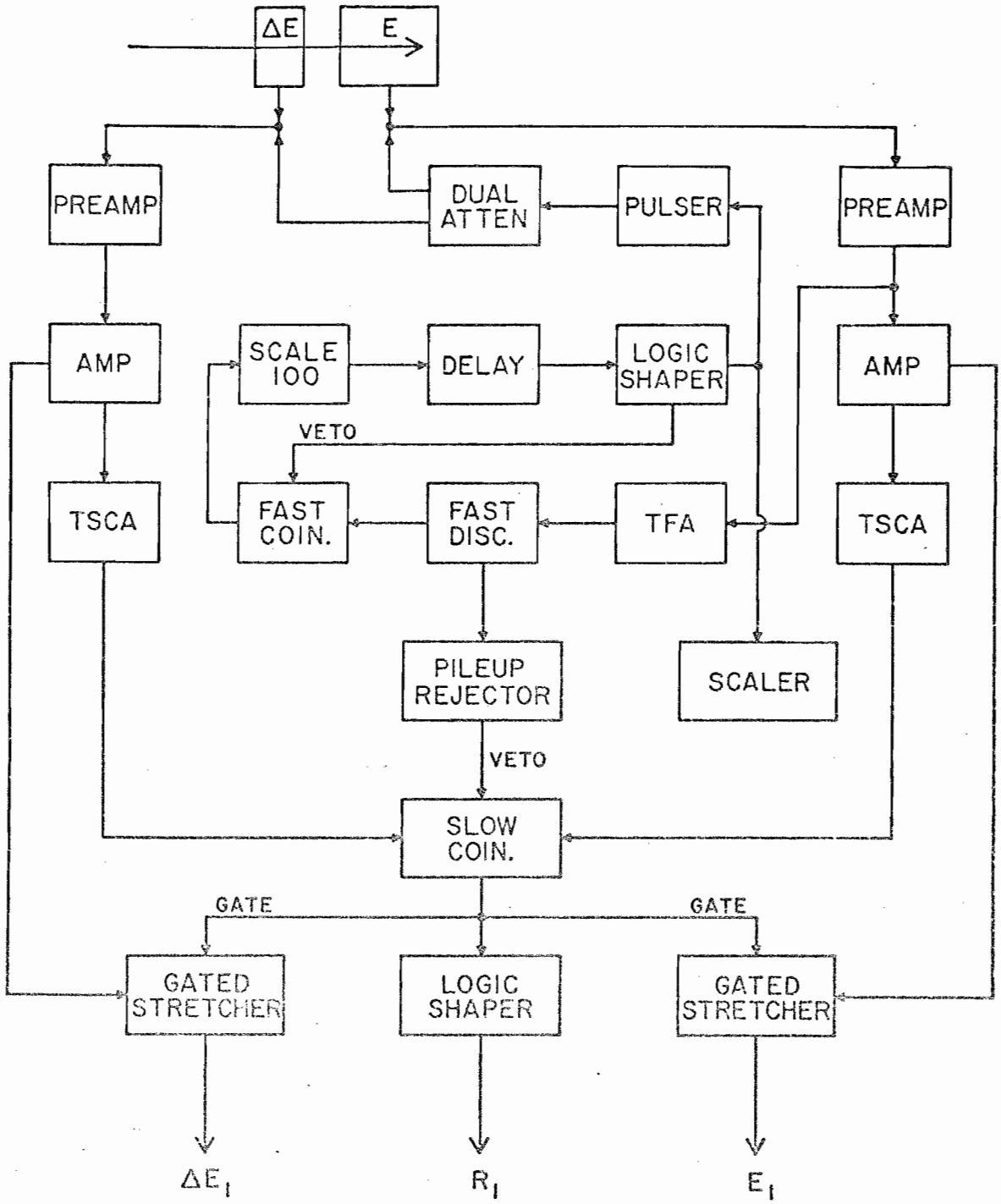
ΔE
E
PREAMP
DUAL ATTEN
PULSER
PREAMP
AMP
SCALE 100
DELAY
LOGIC SHAPER
AMP
VETO
TSCA
FAST COIN.
FAST DISC.
TFA
TSCA
PILEUP REJECTOR
SCALER
VETO
SLOW COIN.
GATE
GATE
GATED STRETCHER
LOGIC SHAPER
GATED STRETCHER
ΔE1
R1
E1

rate of test pulses was proportional to the rate of nuclear events, the ratio of the number of pulser signals stored in the computer to the number of pulses generated and counted by a scaler was identical to the ratio of nuclear events recorded to the actual number of events in the detector. Hence, the true number of nuclear events was easily calculated.

F. Procedure

1. General. The targets and detectors were placed in the scattering chamber, and the chamber was evacuated. When a vacuum of 5×10^{-5} Torr was obtained, the Freon refrigeration system was started, and a period of $\sim$45 minutes was required before the detectors were cooled to about -25°C. Bias voltage was then applied to the detectors.

With the detectors cooled and biased the electronic circuits for the telescopes were set up using a pulser system which sent test signals to both the ΔE and E preamps. First the timing single channel analyzers were adjusted to minimize time jitter in the output signals for input amplitudes between 0.25 and 10.0 volts. Output delays were set to give a ΔE - E coincidence. In the pulse stretchers the gate period initiated by the coincidence signal was set at 2 μs and checked to verify that it preceded the peak of the linear input. Widths and delays for output pulses from the stretchers were adjusted to give overlapping ΔE and E signals. All the DC levels of the linear amplifiers and pulse stretchers were fixed at zero volts.

The use of counter telescopes requires that the ΔE and E signal amplification systems have identical gains. Any gain mismatch results in a degradation of quality of the mass identification (D. D. Armstrong et al., 1969). After making pole-zero adjustments for each amplifier with the beam on target, a test pulse was applied in turn to the input of each preamplifier through the same charge terminator. The gain of each linear amplifier was adjusted so that this test pulse was stored in the same channel in the E + ΔE spectrum. Since the test signals were calibrated with an ^{241}Am alpha source, the dynamic range of the amplifier systems was selected when the gains were matched. Normally this range was between 0 and 24 MeV for the E and between 0 and 15 MeV for the ΔE signals.

A biased amplifier after the E + ΔE summing amplifier was adjusted to select a portion of the total energy spectrum for storage in the computer. The gain and intercept for the recorded E + ΔE spectrum were determined, and the amplifier and ADC for ΔE signals were adjusted to give a ΔE spectrum with an equal gain but with an intercept of zero. Before the mass spectra were accumulated, the measured E + ΔE intercept was entered in the computer by typewriter command.

With the beam on target the coincidence timing for each telescope was rechecked, and only slight adjustments, if any, were ever required. The shape of the summed E + ΔE pulses was also checked to see if any changes in delay or pulse width were necessary in the pulse stretchers.

Data acquisition began with the accumulation of mass spectra similar

to that shown in fig. 3. After the exponent defining the range table (see Appendix A) was varied to optimize the resolution of the mass peaks, then mass windows were selected for particle energy spectra. All energy spectra obtained during the angular distribution measurements were written on magnetic tape for later off-line analysis.

2. $^{24}Mg(d,t)^{23}Mg$ and $^{24}Mg(d,{}^{3}He)^{23}Na$ Angular Distributions.

Using a 21.1-MeV deuteron beam, differential cross sections were measured simultaneously for the $^{24}Mg(d,t)$ and $^{24}Mg(d,{}^{3}He)$ reactions in steps of four or five degrees at laboratory angles from 9^{o} to 85^{o}. Angular distributions were obtained for thirteen states in ^{23}Mg and their analog states in ^{23}Na. Two counter telescopes were employed except at the most forward angles where special attention was given to pile-up rejection and dead-time measurements in one telescope. Each telescope subtended a solid angle of 0.41×10^{-3} steradians.

Typical energy spectra for the $^{24}Mg(d,t)^{23}Mg$ and $^{24}Mg(d,{}^{3}He)^{23}Na$ reactions are illustrated in fig. 4. They have been shifted by an amount comparable to the difference in Q values for these reactions to emphasize the similarities of transitions to mirror states. The overall energy resolution was 42 to 55 keV for the tritons and 80 to 100 keV for the ^{3}He. At some angles the (d,t) reactions with ^{12}C or ^{16}O contaminants in the target obscured the peaks in the energy spectrum for states of ^{23}Mg. Only the $^{12}C(d,{}^{3}He)$ reaction interferred with states of ^{23}Na.

3. $^{24}Mg(d,d)^{24}Mg$ and $^{24}Mg(d,d')^{24}Mg$ Angular Distributions.

Elastic and inelastic scattering cross sections were measured for 21.1-MeV

Figure 3. Typical mass spectra taken during the $^{24}Mg(d,{}^{3}He)^{23}Na$ and $^{24}Mg(d,t)^{23}Mg$ angular distribution measurements. The counter telescope employed for this data consisted of a 50 μm ΔE detector and a 1500 μm E detector. The exponent describing the energy dependence of the range of charged particles in Silicon (see Appendix A) was taken as n = 1.65 for this spectrum.

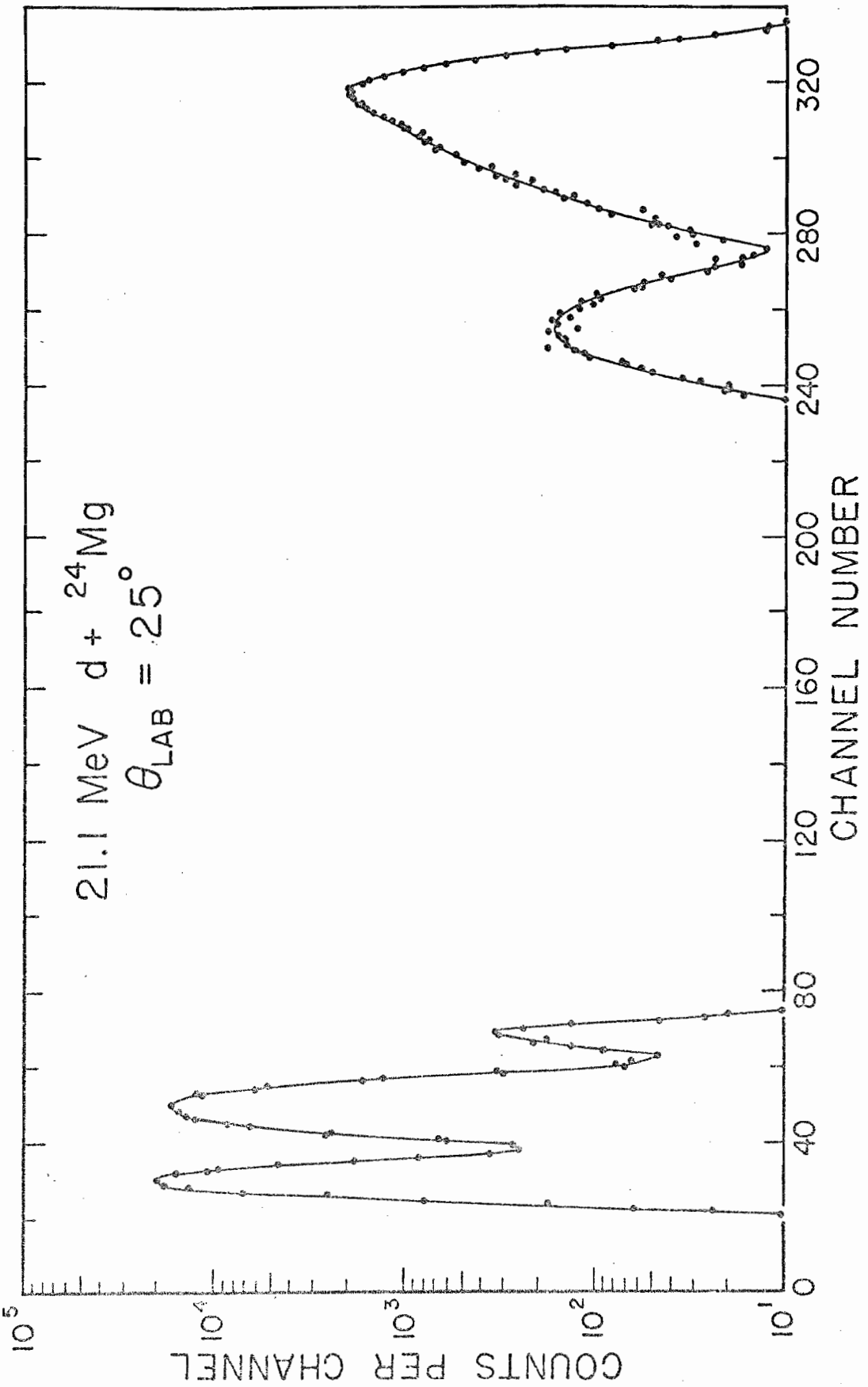
21.1 MeV d + ^{24}Mg
$\theta_{LAB} = 25°$
COUNTS PER CHANNEL
CHANNEL NUMBER
10^5
10^4
10^3
10^2
10^1
0
40
80
120
160
200
240
280
320

Figure 4. Sample energy spectra of (d, ^{3}He) and (d,t) reaction data. The energy spectrum for the ^{24}Mg(d,t)^{23}Mg reaction is displayed in the upper portion of this figure. The solid lines are meant only to guide the eye. The ^{24}Mg(d, ^{3}He)^{23}Na, shown in the lower portion, has been shifted to emphasize the similarities of transitions to mirror states. Peaks in the spectra are identified by excitation values (in MeV).

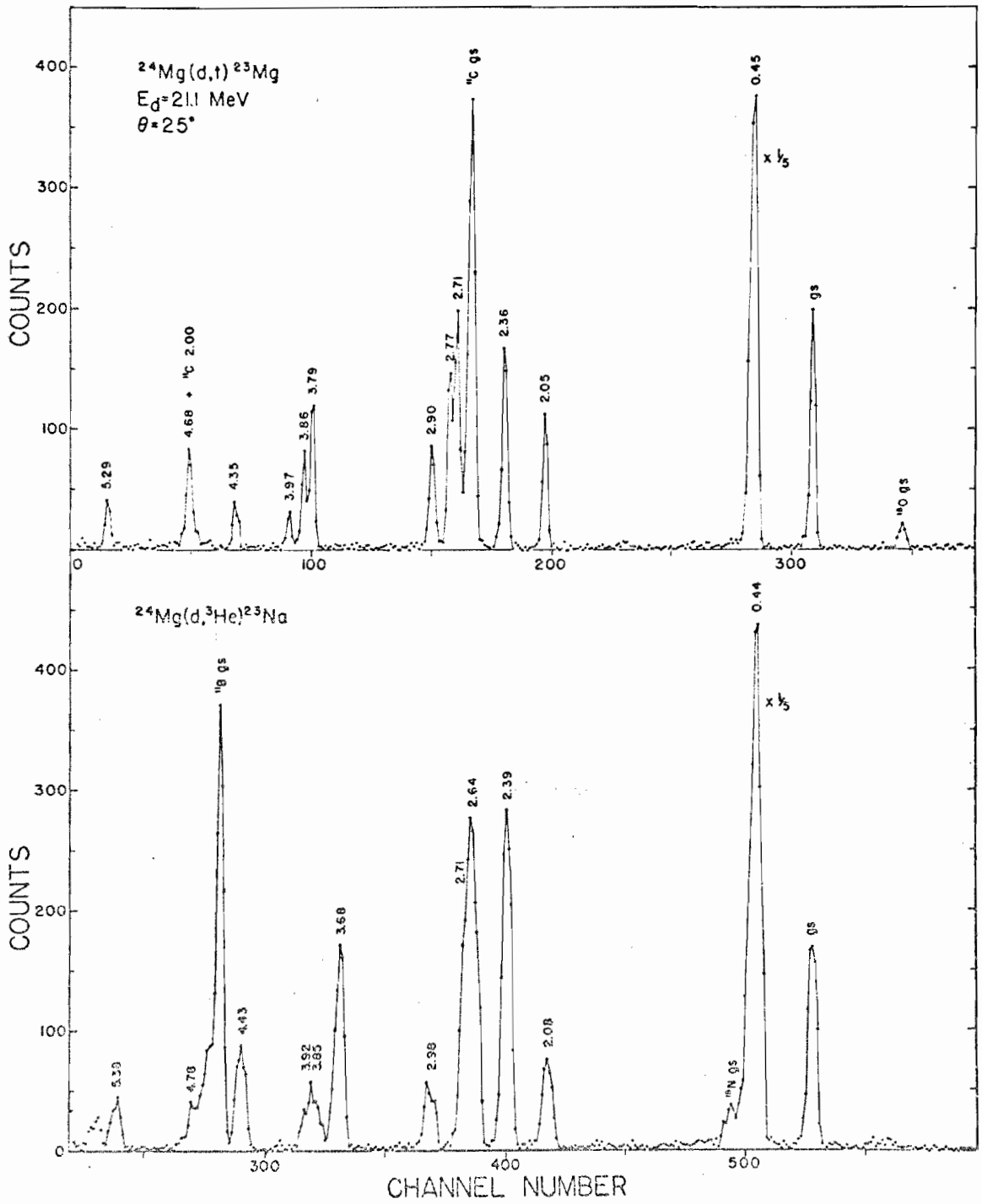
^{24}Mg(d,t)^{23}Mg
E_d=21.1 MeV
θ=25°
^{11}C gs
0.45
x 1/5
gs
2.71
2.77
2.36
2.90
2.05
3.79
3.86
3.97
4.35
4.68 + ^{11}C 2.00
5.29
^{10}O gs
COUNTS
^{24}Mg(d,^{3}He)^{23}Na
^{11}B gs
0.44
x 1/5
2.64
2.39
2.71
3.68
4.43
3.92
3.85
2.98
2.08
5.33
4.78
^{11}N gs
gs
CHANNEL NUMBER

deuterons incident on ^{24}Mg at laboratory angles from 20^{o} to 155^{o} in steps of five degrees. Angular distributions for the ground-state and the first 2^{+} and 4^{+} excited states were measured. Two counter telescopes were used, each consisting of a 200 μm ΔE detector and a 2000 μm E detector. Other details of the setup were identical with those used in the (d,t) and (d, ^{3}He) measurements. The peak corresponding to the 1.37-MeV 2^{+} state in fig. 5 illustrates that inelastic cross sections at back angles frequently are larger than elastic scattering.

4. ^{23}Na(^{3}He, ^{3}He)^{23}Na Angular Distributions. In order to determine optical model parameters for the exit channel in calculations predicting the ^{24}Mg(d, ^{3}He)^{23}Na differential cross sections, the elastic cross sections were measured for ^{3}He incident on ^{23}Na at energies of 9.0 and 15.0 MeV. Measurements using a self-supporting NaF target were made in five degree increments at angles from 25^{o} to 150^{o} at 9 MeV and from 20^{o} to 105^{o} at 15 MeV. Since it was necessary to discriminate ^{3}He from alpha-particles, two counter telescopes were used with 17 μm ΔE detectors and 1500 μm E detectors. Each telescope subtended a solid angle of 0.23 X 10^{-3} steradians. The spectrum in fig. 6 shows the peaks for elastic scattering of 15-MeV ^{3}He from ^{23}Na and the various contaminants in the target. Spectra taken at different angles were normalized to the area of the ^{181}Ta peak counted in a monitor detector.

Figure 5. $^{24}Mg(d,d')^{24}Mg$ energy spectra for scattering of 21.1-MeV deuterons. Peaks in the spectra are identified by excitation values (in MeV). Note that the inelastic cross section to the first excited state (2^+) at 1.37 MeV is larger than the elastic cross section for this angle, $\Theta_{LAB} = 65^{\circ}$.

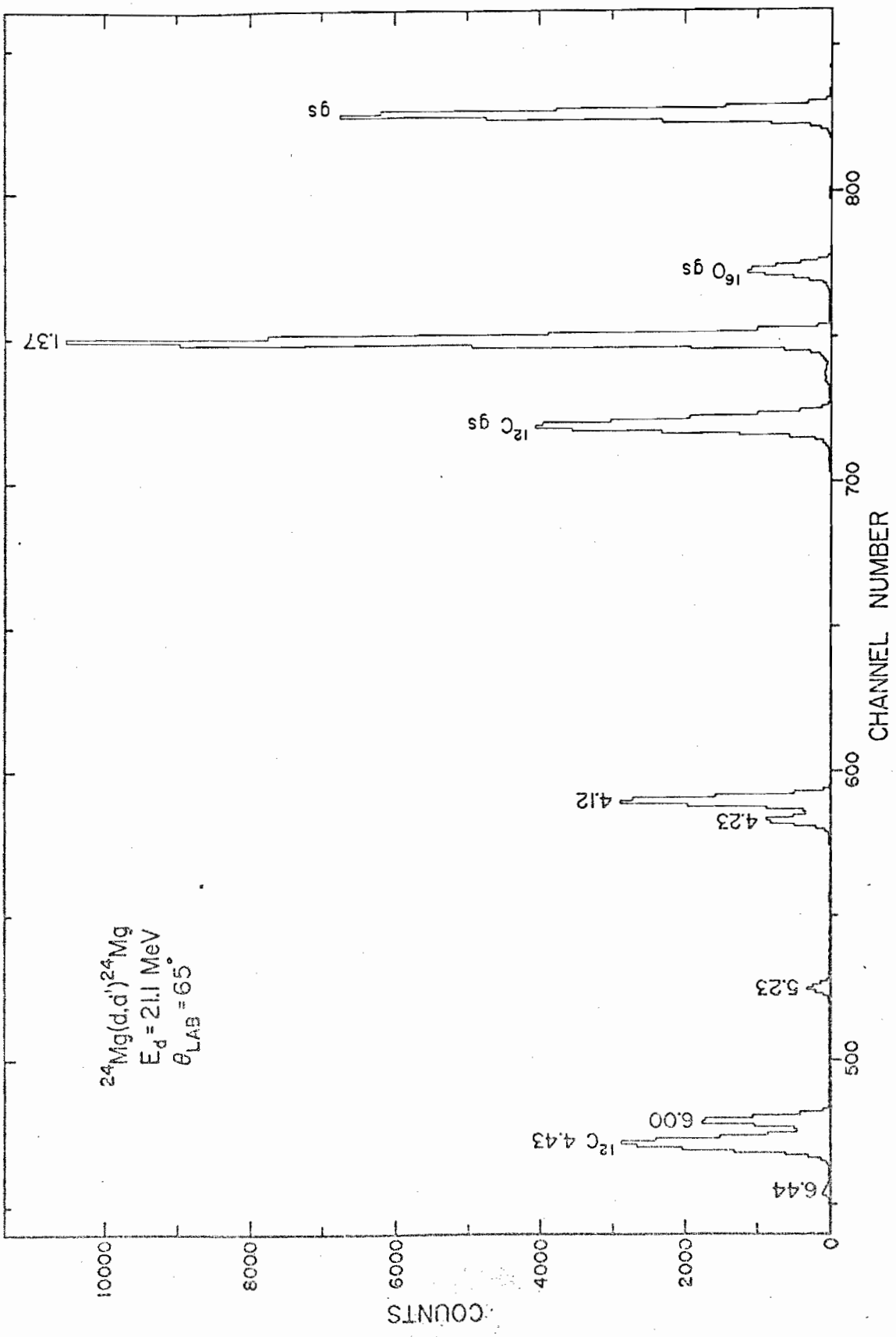
$^{24}Mg(d,d')^{24}Mg$
$E_d = 21.1$ MeV
$\theta_{LAB} = 65°$
COUNTS
CHANNEL NUMBER
0
2000
4000
6000
8000
10000
500
600
700
800
6.44
^{12}C 4.43
6.00
5.23
4.23
4.12
gs
^{12}C gs
1.37
^{16}O gs
gs

Figure 6. $^{23}Na(^{3}He, ^{3}He)^{23}Na$ energy spectrum for scattering at 15.0 MeV. The various contaminants are identified in addition to the ^{23}Na elastic peak.

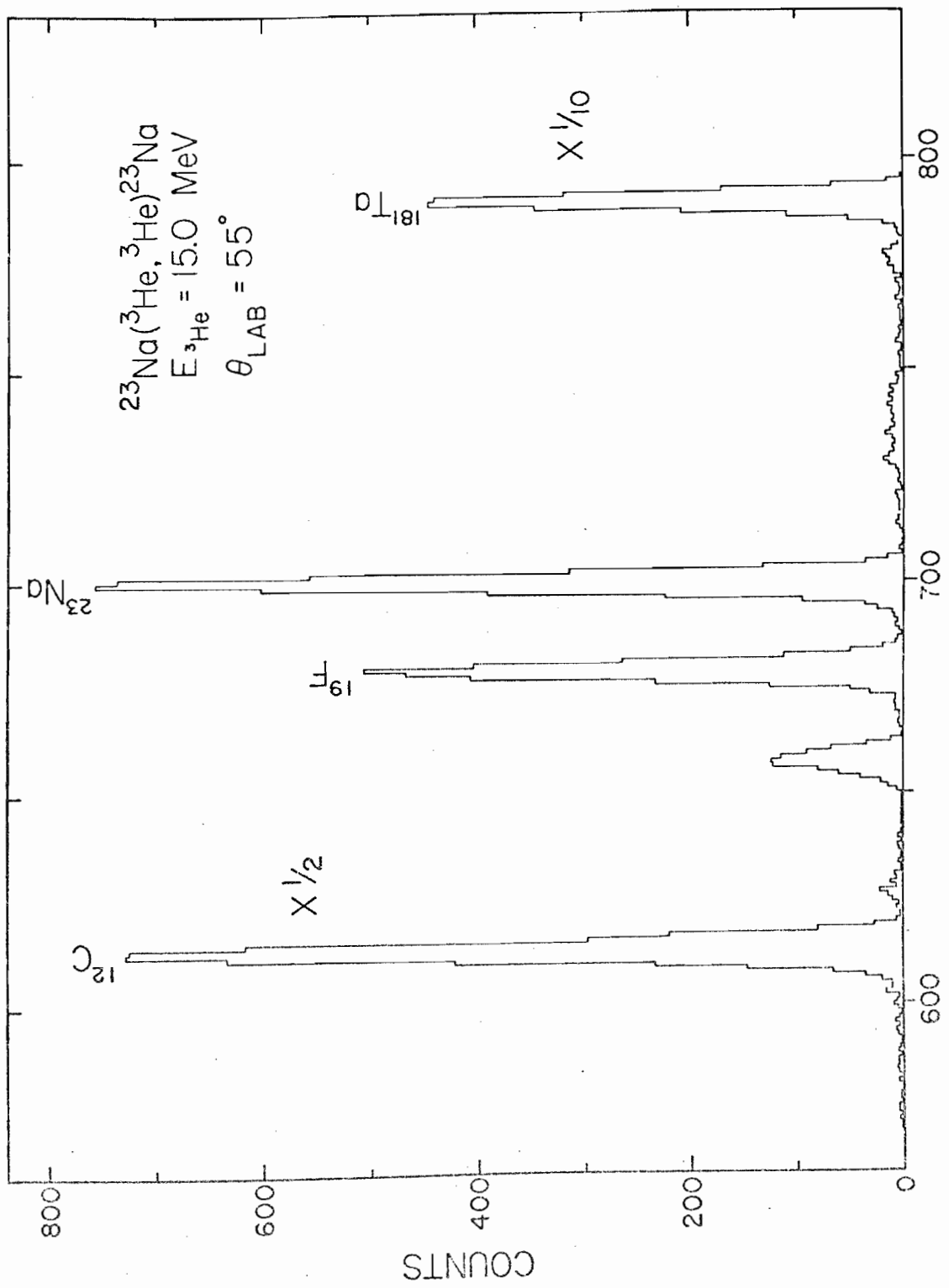
$^{23}Na(^{3}He,^{3}He)^{23}Na$
$E_{^{3}He}$ = 15.0 MeV
θ_{LAB} = 55°
^{12}C
X 1/2
^{19}F
^{23}Na
^{181}Ta
X 1/10
COUNTS
CHANNEL NUMBER
0
200
400
600
800
600
700
800

Chapter III

EXPERIMENTAL RESULTS AND DATA ANALYSIS

A. $^{24}Mg(d,d')^{24}Mg$ Angular Distributions and Coupled-Channel Calculations

The angular distributions for the elastic and inelastic scattering of deuterons from ^{24}Mg are shown in fig. 7. Note that at angles greater than 70° in the center of mass, the cross section for scattering from the 2^{+} state is greater than the elastic scattering. The deuteron energy, 21.1 MeV, was chosen to match the energy at which the (d,t) and (d, ^{3}He) differential cross sections were measured. The statistical error for each point is less than the error represented by the size of the data point.

The curves through the data points were obtained from a coupled-channel calculation using the Karlsruhe version (G. W. Schweimer et al., 1967) of JUPITOR by T. Tamura (1967). In the program the optical potentials for the calculation were chosen to have a Woods-Saxon form factor modified by a static quadrupole deformation. As discussed in Appendix B, this deformation couples the states of a rotational band within the target and enhances inelastic

Figure 7. $^{24}Mg(d,d')^{24}Mg$ angular distributions for elastic scattering and inelastic scattering from the 2^+ state at 1.37 MeV. At angles greater than 70^o in the center of mass, the cross section for the latter state is greater than the elastic scattering. The solid (broken) lines represent the coupled-channel optical model fits obtained using parameters from the Vr^n ambiguity (see fig. 8) with V = 70.6 (97.5) MeV.

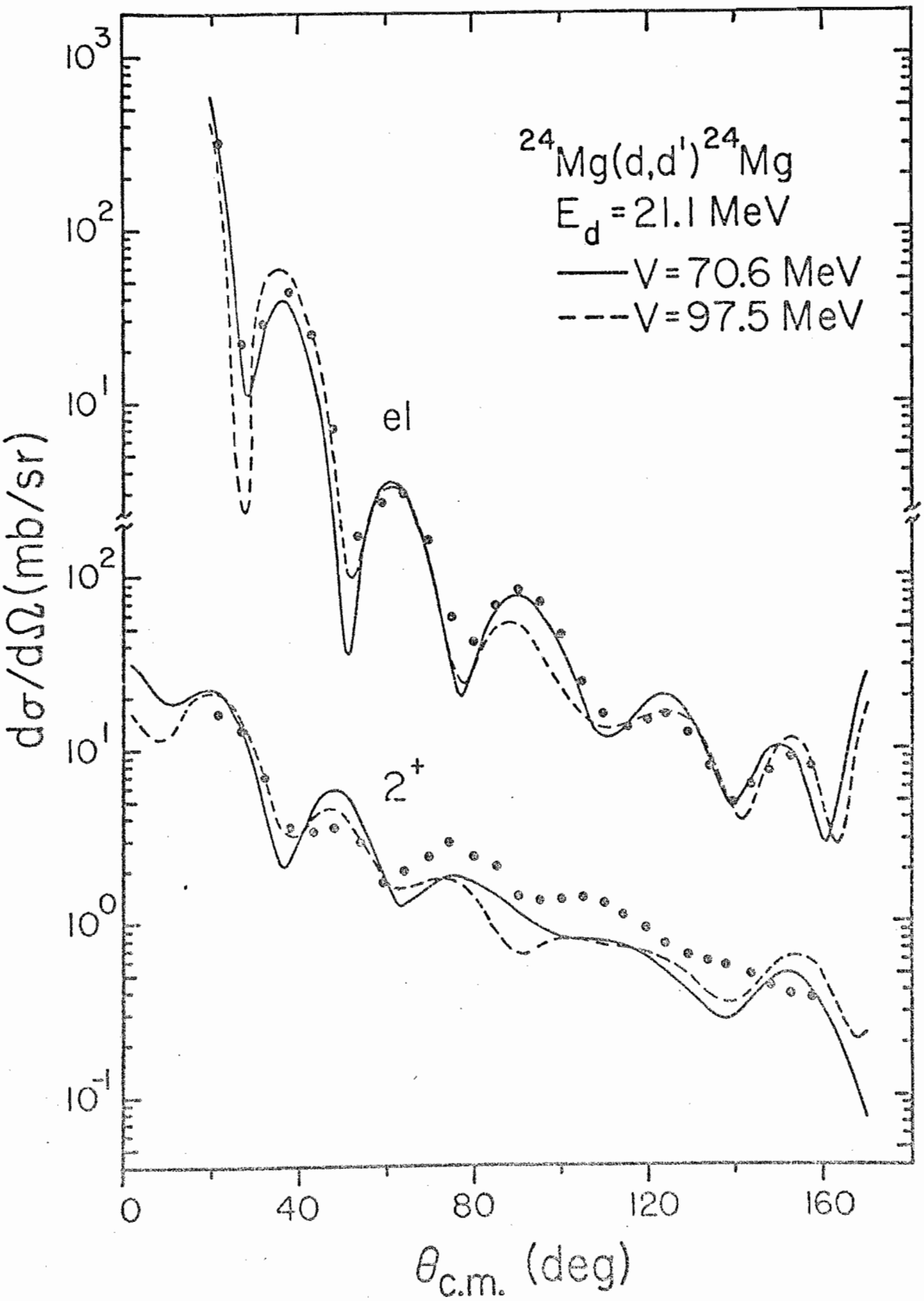
^{24}Mg(d,d')^{24}Mg
E_d = 21.1 MeV
V = 70.6 MeV
V = 97.5 MeV
el
2$^+$
$d\sigma/d\Omega$ (mb/sr)
$\theta_{c.m.}$ (deg)
10^3
10^2
10^1
10^2
10^1
10^0
10^{-1}
0
40
80
120
160

scattering from these states. Consequently, one must select optical model parameters which describe a few of the strongest inelastic transitions as well as the elastic scattering. In Section C these inelastic processes will be introduced into the description of the direct reactions.

A search routine in this version of JUPITOR automatically adjusted combinations of parameters to minimize χ^2 defined as

$$\chi^2 = \sum_{n,i} \left[\frac{\sigma^{(n)}_{exp}(\theta_i) - \sigma^{(n)}_{theory}(\theta_i)}{0.1\ \sigma^{(n)}_{exp}(\theta_i)} \right]^2$$

where n labels the cross section for the n^{th} state at angle θ_i. The search began using the parameters given by Tjin A Djie et al. (1968) for deuteron scattering from ^{24}Mg at 26 MeV. Combinations of two or three parameters were varied simultaneously until a minimum χ^2 was reached for the fits to scattering from the ground and first 2^+ state. From these calculations the deformation parameter, β, was determined to be 0.46 indicating a large prolate deformation. This value is consistant with that obtained by other authors (Tjin A Djie et al., 1968; T. Tamura, 1965; M. P. Fricke et al., 1965).

In order to explore the ambiguities of this parameter set, the real well depth was increased $\sim$7.5 MeV and the code allowed to search over all other parameters except β. A sequence of such calculations traced out the ambiguity shown in fig. 8. Coupled-channel predictions using parameters from extremeties of the continuous ambiguity are shown in fig. 7.

To investigate the difference between the parameters for this deformed potential and those for the usual spherical potential, an equivalent calculation

Figure 8. Optical model parameters for 21.1-MeV deuterons scattering from ^{24}Mg. The optical model parameters for deformed (spherical) potentials which yield a minimum χ^2 with fixed deformation $\beta = 0.46$ (0.0), are indicated by the solid (broken) line for various real well depths, V. These parameters constitute what is termed the Vr^n continuous ambiguity (see fig. 10).

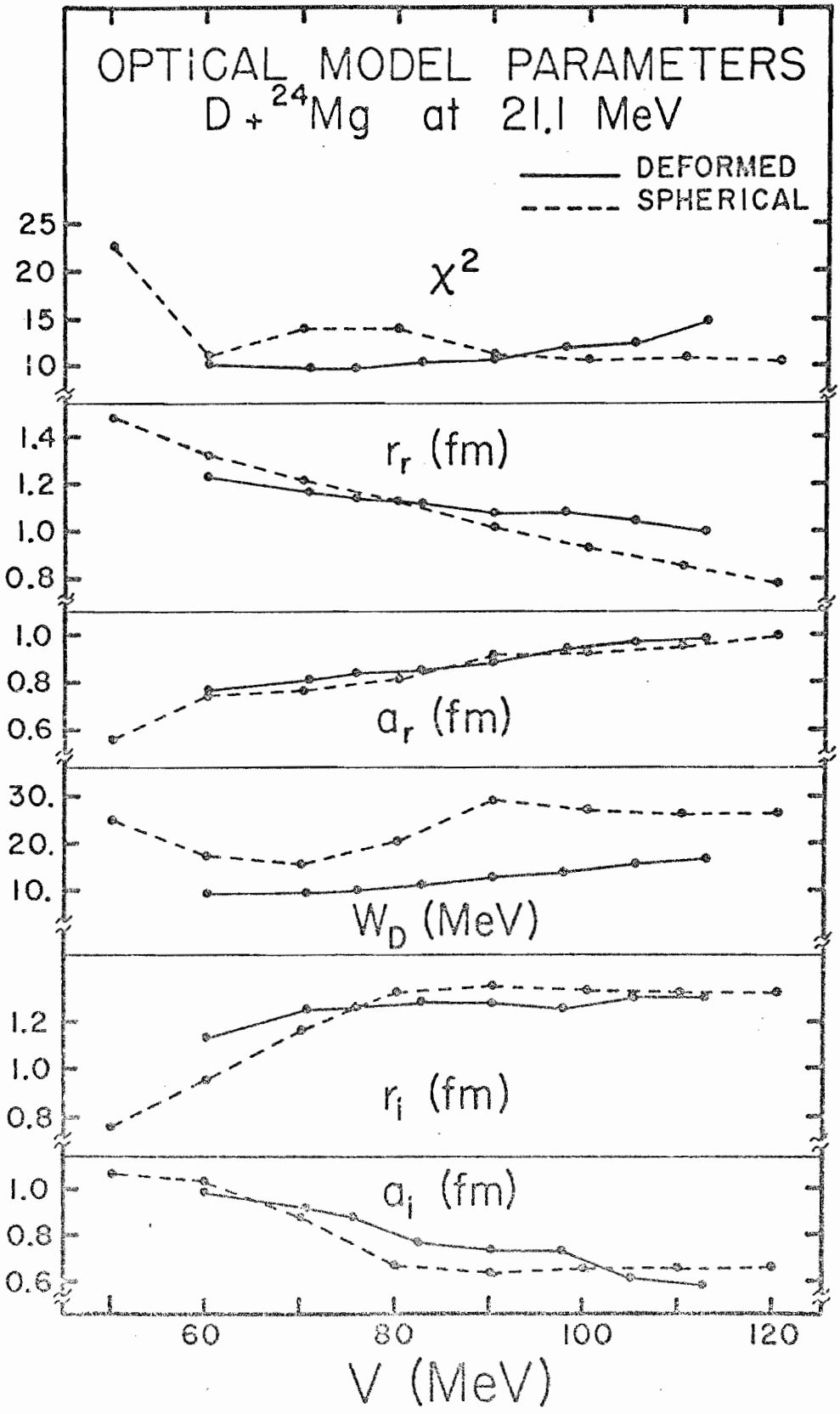
OPTICAL MODEL PARAMETERS
D + 24Mg at 21.1 MeV
DEFORMED
SPHERICAL
χ2
25
20
15
10
rr (fm)
1.4
1.2
1.0
0.8
ar (fm)
1.0
0.8
0.6
WD (MeV)
30.
20.
10.
ri (fm)
1.2
1.0
0.8
ai (fm)
1.0
0.8
0.6
60
80
100
120
V (MeV)

with a spherical potential was performed using JUPITOR and fitting only the elastic cross sections. As seen in fig. 8 the results are quite similar except that the absorption well depths for the spherical potential are ~10 MeV greater. This difference is anticipated since the coupled-channel calculation explicitly calculates an inelastic transition which must be included in the absorption potential in the normal optical model calculation. The magnitude of the difference emphasizes the great absorptive strength provided by this one channel.

Using the parameters obtained from fitting cross sections in two channels, the calculation was expanded to include the 4^+ member of the ground-state rotational band and the first 2^+ vibrational state. Although the quality of the fit to the elastic scattering is somewhat poorer, the predictions for the 4^+ and vibrational 2^+ states are quite good.

B. $^{23}Na(^3He, ^3He)^{23}Na$ Angular Distributions and Optical Model Calculations

Figure 9 shows the ^3He angular distributions for scattering from ^{23}Na at 9.0 and 15.0 MeV. These energies correspond approximately to the energies of the outgoing light particles for the ground-state transition in the (d,t) and (d,^{3}He) reactions, respectively. The statistical error for each point is less than the error indicated by the size of the data point.

Using the code SNOOPT2 (W. J. Thompson, 1970) an automatic search over the optical model parameters produced results analogous to those obtained

Figure 9. $^{23}Na(^{3}He, ^{3}He)^{23}Na$ angular distributions. The solid lines represent the optical model fits, and the corresponding well depths are indicated with each curve. The geometric parameters describing the shape of the spherical potential wells are the same for the fits at both energies.

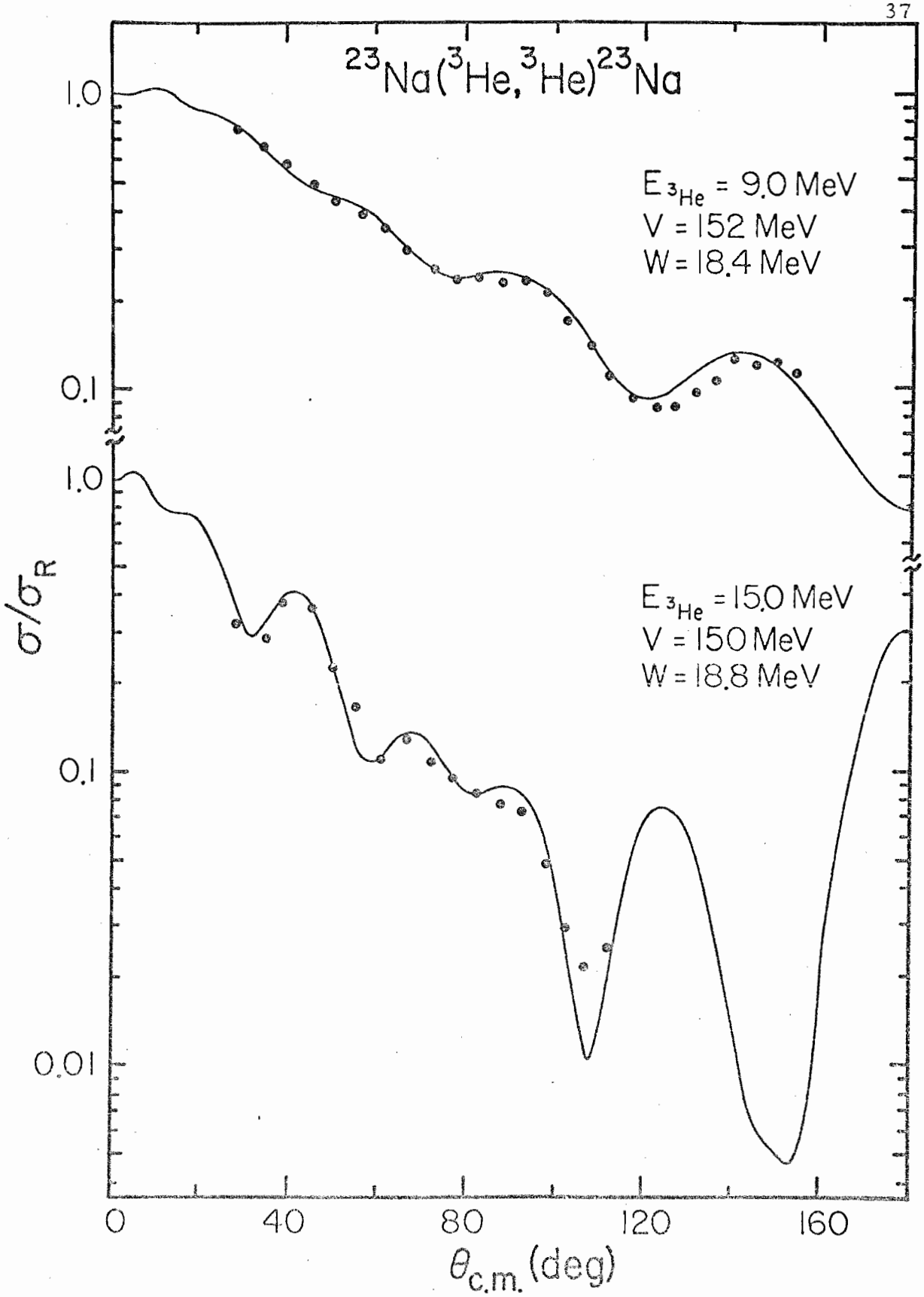
$^{23}Na(^{3}He,^{3}He)^{23}Na$
$E_{^{3}He}$ = 9.0 MeV
V = 152 MeV
W = 18.4 MeV
$E_{^{3}He}$ = 15.0 MeV
V = 150 MeV
W = 18.8 MeV
σ/σ_R
1.0
0.1
1.0
0.1
0.01
0
40
80
120
160
$\theta_{c.m.}$ (deg)

for the deuteron scattering. These calculations were performed using spherical potentials. A more complicated coupled-channel search was not attempted since the inelastic scattering at back angles was observed to be a factor of 10 weaker than the elastic scattering. The curve shown in fig. 9 for the 15.0-MeV data represents the fit for minimum χ^2 with a real well depth of 150 MeV. Using the same geometric parameters for the potentials, the well depths were adjusted to give best fit to the 9.0-MeV data shown as the other curve in fig. 9. The well depths obtained in this calculation differed only slightly from those for the 15.0-MeV data indicating the energy dependence of the optical model parameters may not be very significant over this energy range.

Fitting only the 15.0-MeV ^{3}He scattering data, a search over the continuous ambiguity yielded the results displayed in fig. 10. These calculations and results are similar to those of G. Scheklinski et al. (1970) and R. W. Zurmühle et al. (1969).

To estimate the significance of coupling among states in ^{23}Na for the ^{3}He scattering, the optical model parameters obtained from the above optical model analysis were modified for a coupled-channel calculation. Only the ground-state ($^3/_2^+$) and the 0.44-MeV ($^5/_2^+$) levels were included in the calculation. The similarities between the spherical and deformed potential parameters for the deuteron scattering suggested that it was reasonable to reduce the absorption well depth, W, and retain all the other parameters. The deformation parameter was taken to be 0.46, the same deformation as determined for ^{24}Mg. This value is in good agreement with the recent inelastic proton analysis of

Figure 10. Optical model parameters for 15.0-MeV ^{3}He scattering from ^{23}Na. The optical model parameters for spherical potentials which yield a minimum χ^2 are plotted for various real well depths, V. As may be seen from the second curve from the top, the product $Vr^{1.33}$ remains constant over the range of V shown. This feature is characteristic of what are termed Vr^{n} ambiguities.

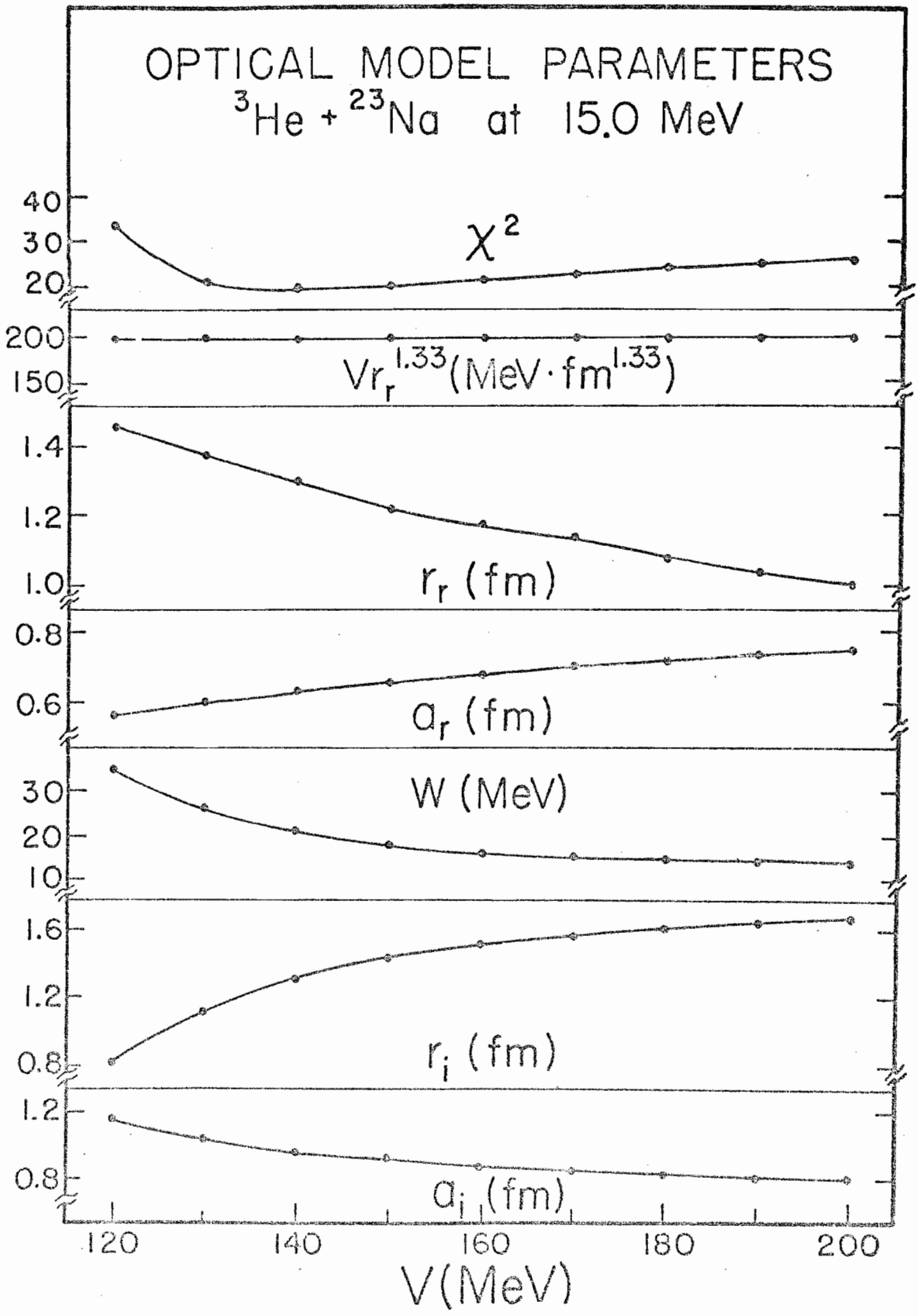
OPTICAL MODEL PARAMETERS
$^{3}He + ^{23}Na$ at 15.0 MeV
40
30
20
χ^2
200
150
$Vr_r^{1.33}$ (MeV · fm$^{1.33}$)
1.4
1.2
1.0
r_r (fm)
0.8
0.6
a_r (fm)
30
20
10
W (MeV)
1.6
1.2
0.8
r_i (fm)
1.2
0.8
a_i (fm)
120
140
160
180
200
V(MeV)

P. L. Ottaviani et al. (1970) which concluded $\beta = 0.48$ for ^{23}Na. Cross section predictions with different W indicated the full absorption well depth was necessary to describe both the observed elastic and inelastic scattering. Therefore, one must conclude the inelastic effects from low-lying coupled states constitute only a minor portion of the absorptive processes present for ^{3}He scattering at this energy.

C. ^{24}Mg(d,^{3}He)^{23}Na and ^{24}Mg(d,t)^{23}Mg Angular Distributions and Analysis

1. Experimental Results. The results from the ^{24}Mg(d,^{3}He)^{23}Na and ^{24}Mg(d,t)^{23}Mg measurements are shown in figs. 11-15 along with the fits to the data. Selected angular distributions from figs. 12-15 are reproduced in fig. 11 for comparisons with different theoretical predictions. Only the CCBA calculations are shown in figs. 12-15. For states which were well resolved in the data, the error bars indicate only the statistical error. However, doublets at 2.71-2.77 and 3.79-3.86 MeV in the (d,t) data and at 2.64-2.71 and 3.85-3.92 MeV in the (d,^{3}He) data required a Gaussian fitting procedure to extract areas for these peaks. Consequently, the errors for these distributions reflect the uncertainty in the parameterization of the doublets. The absolute normalization determined from the geometry of the counter telescopes, the beam integration and the target thickness measurement, is believed accurate within 10%. Since scattered t and ^{3}He were detected and processed with virtually identical electronic systems, there is no additional normalization factor between

Figure 11. Comparisons of DWBA and CCBA calculations. Selected angular distributions from figs. 12-15 are reproduced in this figure for comparisons with different theoretical predictions. The solid curve is the result of the full CCBA calculation which included both direct and indirect population of the final state. The DWBA calculation represented by the broken line includes only the direct transitions and was performed employing a spherical optical model potential equivalent to the deformed potential used in the CCBA calculation. Also shown (dotted line) are the results of the CCBA calculation where only the direct term was included. The number indicated for each curve is the normalization factor required for the prediction to agree with the data. This factor should be near unity (see text).

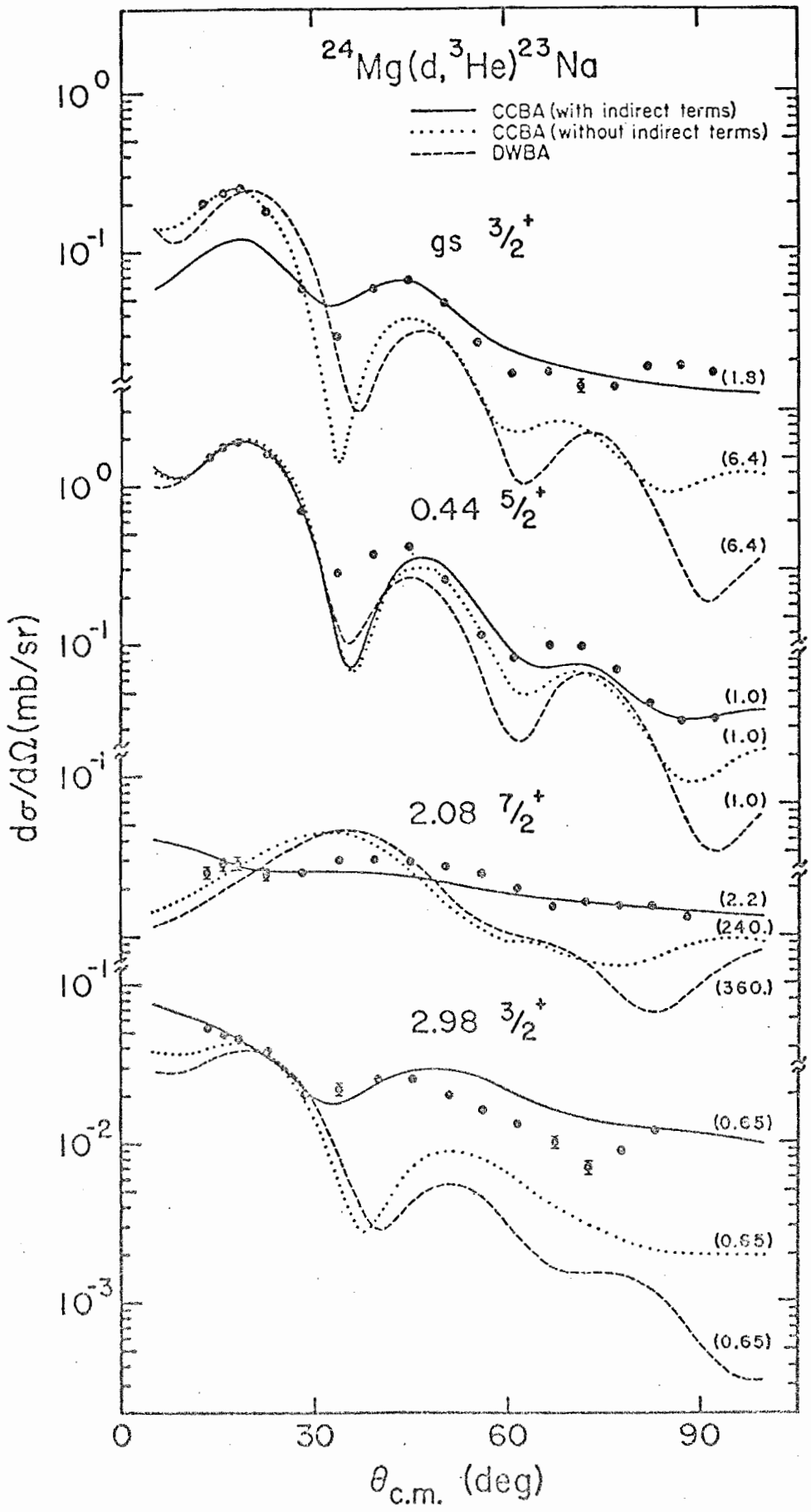
^{24}Mg(d,^{3}He)^{23}Na
CCBA (with indirect terms)
CCBA (without indirect terms)
DWBA
gs 3/2+
0.44 5/2+
2.08 7/2+
2.98 3/2+
(1.8)
(6.4)
(6.4)
(1.0)
(1.0)
(1.0)
(2.2)
(240.)
(360.)
(0.65)
(0.65)
(0.65)
dσ/dΩ (mb/sr)
θc.m. (deg)
0
30
60
90

Figure 12. $^{24}Mg(d,{}^{3}He)^{23}Na$ and $^{24}Mg(d,t)^{23}Mg$ angular distributions for transitions to the ground-state $K^{\pi} = {}^{3}/_{2}^{+}$ band. The solid curves represent the CCBA fits.

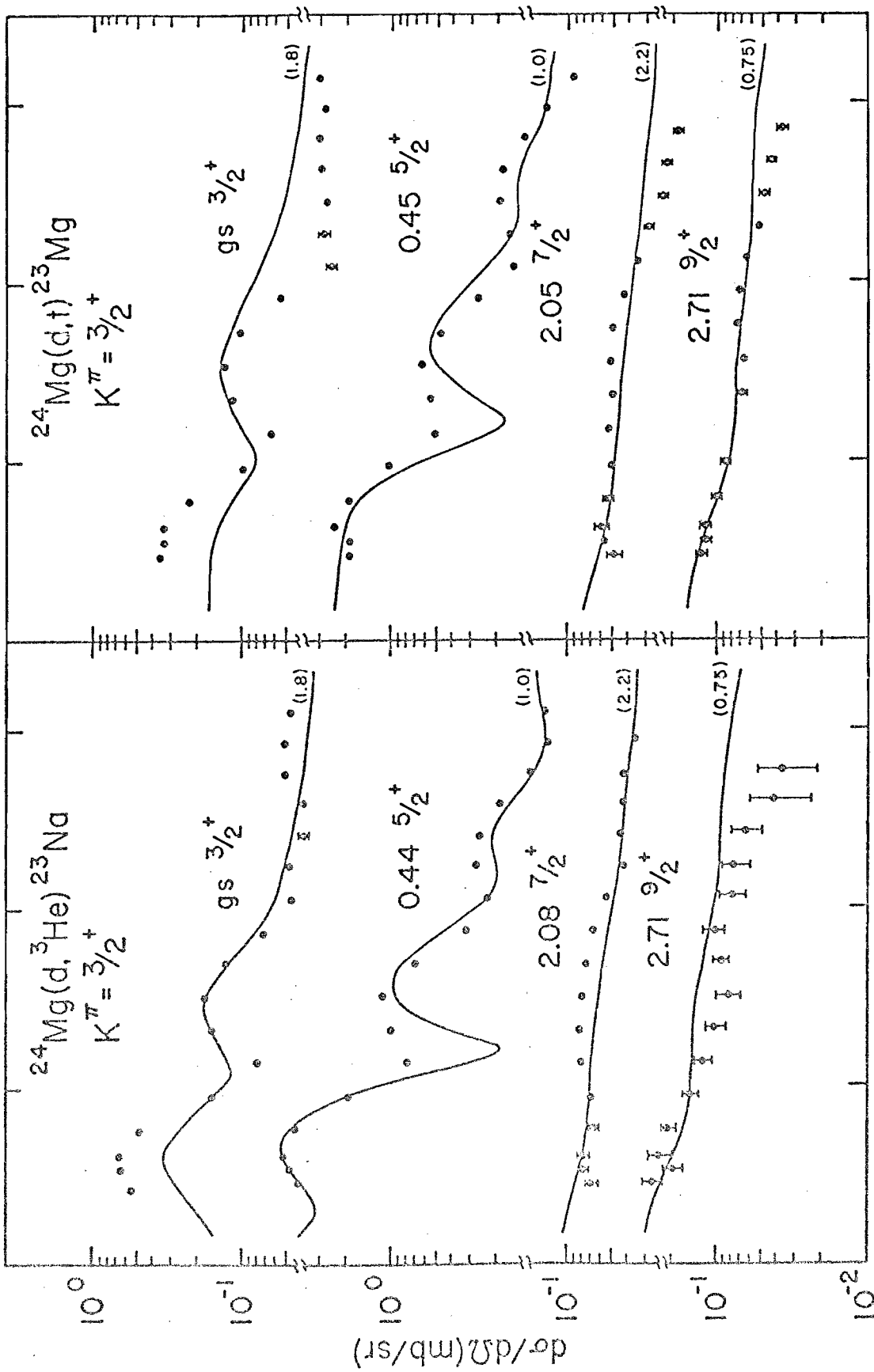
^{24}Mg(d,^{3}He)^{23}Na
$K^{\pi} = 3/2^{+}$
gs $3/2^{+}$
0.44 $5/2^{+}$
2.08 $7/2^{+}$
2.71 $9/2^{+}$
^{24}Mg(d,t)^{23}Mg
$K^{\pi} = 3/2^{+}$
gs $3/2^{+}$
0.45 $5/2^{+}$
2.05 $7/2^{+}$
2.71 $9/2^{+}$
(1.8)
(1.0)
(2.2)
(0.75)
$d\sigma/d\Omega$(mb/sr)
$\theta_{c.m.}$ (deg)

Figure 13. $^{24}Mg(d,{}^{3}He)^{23}Na$ and $^{24}Mg(d,t)^{23}Mg$ angular distributions for transitions to the first $K^{\pi} = {}^{1}/_{2}^{+}$ band. The solid curves represent the CCBA fits.

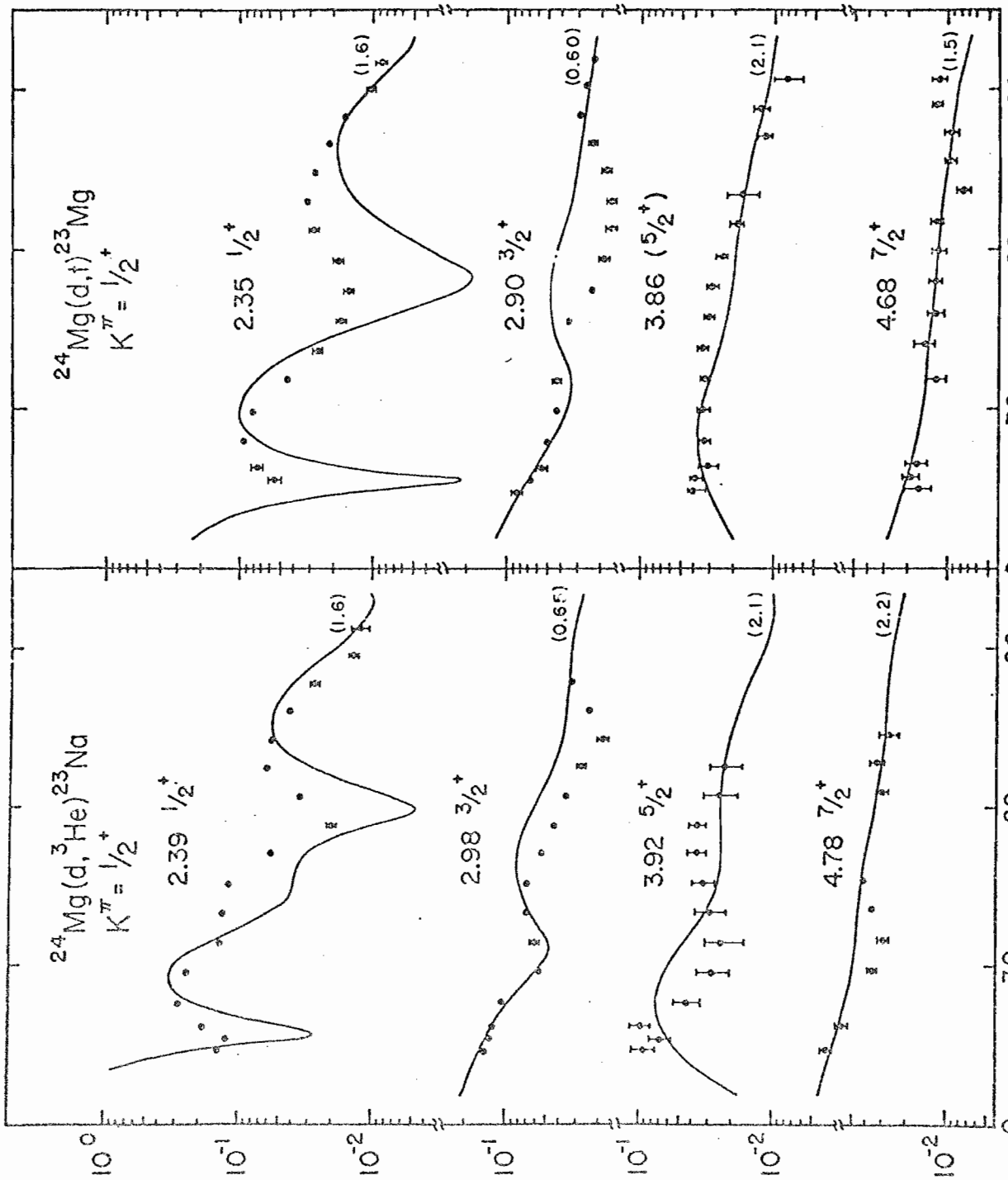
^{24}Mg(d,^{3}He)^{23}Na
$K^{\pi} = 1/2^{+}$
2.39 $1/2^{+}$
2.98 $3/2^{+}$
3.92 $5/2^{+}$
4.78 $7/2^{+}$
^{24}Mg(d,t)^{23}Mg
$K^{\pi} = 1/2^{+}$
2.35 $1/2^{+}$
2.90 $3/2^{+}$
3.86 $(5/2^{+})$
4.68 $7/2^{+}$
(1.6)
(0.65)
(2.1)
(2.2)
(0.60)
(1.5)
$d\sigma/d\Omega$(mb/sr)
10^{0}
10^{-1}
10^{-2}
0
30
60
90
$\theta_{c.m.}$ (deg)

Figure 14. $^{24}Mg(d,{}^{3}He)^{23}Na$ and $^{24}Mg(d,t)^{23}Mg$ angular distributions for transitions to the second $K^{\pi} = {}^{1}/_{2}{}^{+}$ band. The solid curves represent the CCBA fits.

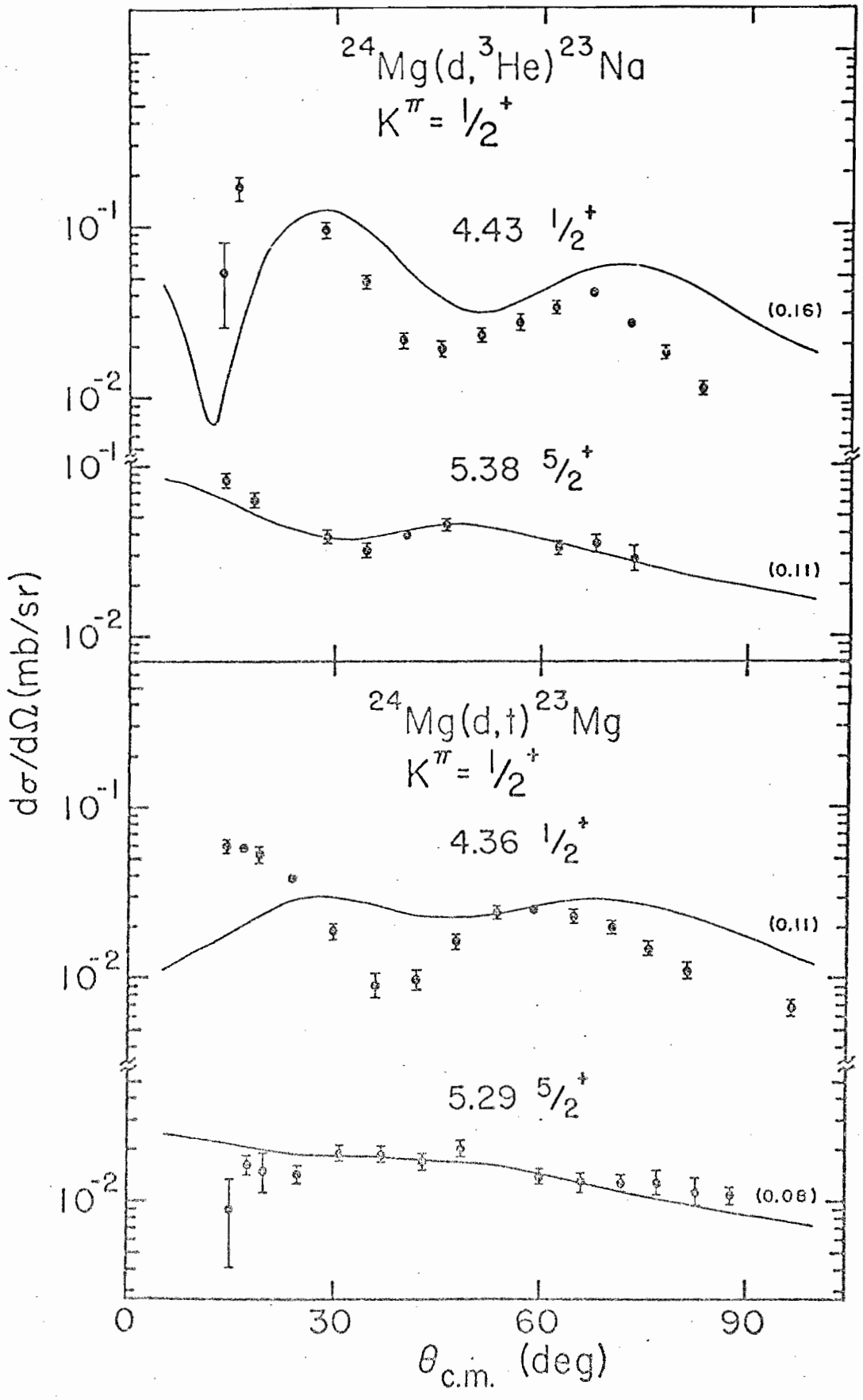
^{24}Mg(d,^{3}He)^{23}Na
$K^{\pi} = 1/2^{+}$
4.43 $1/2^{+}$
(0.16)
5.38 $5/2^{+}$
(0.11)
^{24}Mg(d,t)^{23}Mg
$K^{\pi} = 1/2^{+}$
4.36 $1/2^{+}$
(0.11)
5.29 $5/2^{+}$
(0.06)
$d\sigma/d\Omega$ (mb/sr)
10^{-1}
10^{-2}
0
30
60
90
$\theta_{c.m.}$ (deg)

Figure 15. $^{24}Mg(d,{}^{3}He)^{23}Na$ and $^{24}Mg(d,t)^{23}Mg$ angular distributions for transitions to the first $K^{\pi} = {}^{1}/_{2}^{-}$ band. The solid curves represent the CCBA fits.

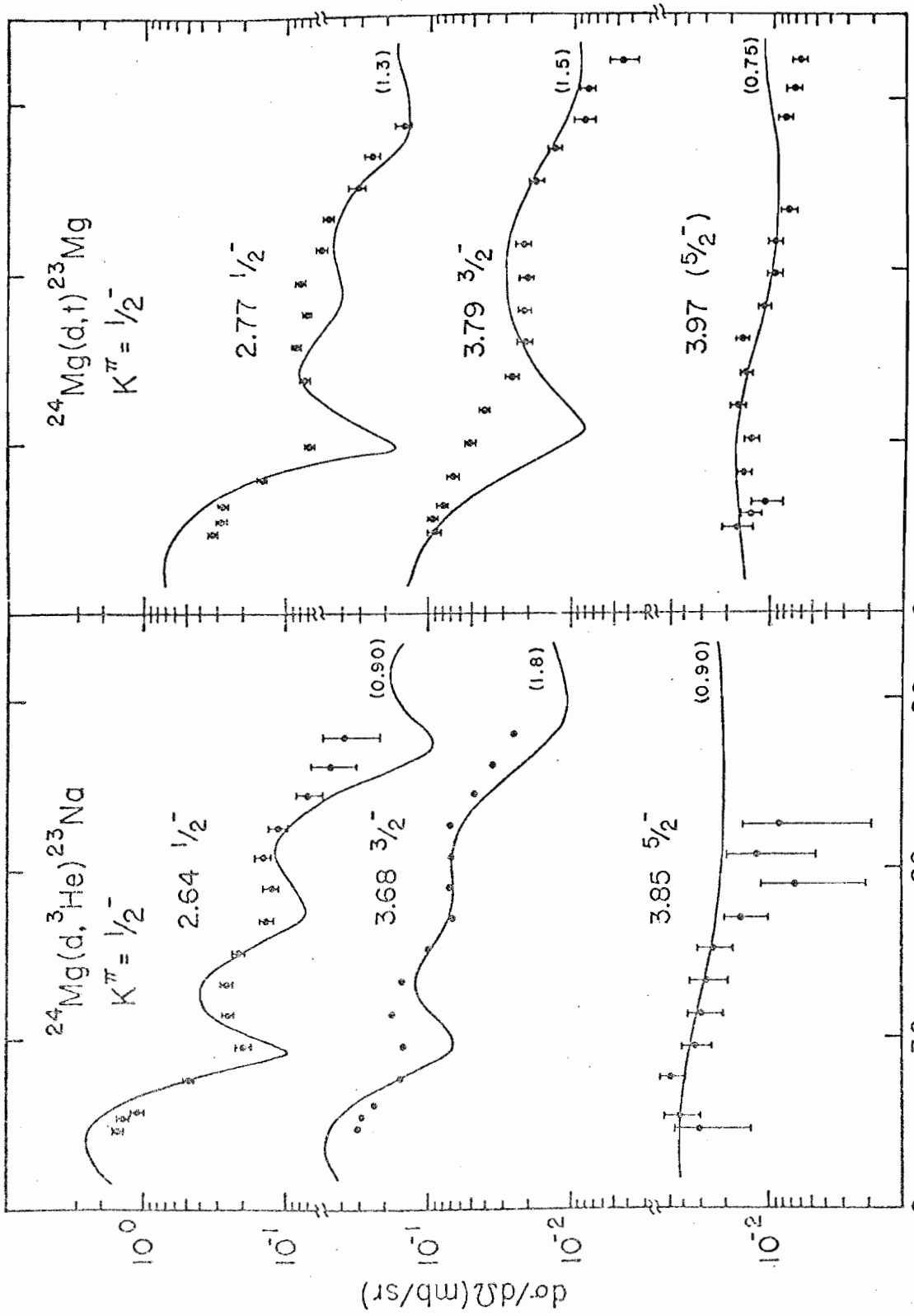
^{24}Mg(d,^{3}He)^{23}Na
$K^{\pi} = 1/2^-$
2.64 $1/2^-$
3.68 $3/2^-$
3.85 $5/2^-$
(0.90)
(1.8)
(0.90)
^{24}Mg(d,t)^{23}Mg
$K^{\pi} = 1/2^-$
2.77 $1/2^-$
3.79 $3/2^-$
3.97 $(5/2^-)$
(1.3)
(1.5)
(0.75)
$d\sigma/d\Omega$(mb/sr)
10^{0}
10^{-1}
10^{-1}
10^{-2}
10^{-2}
0
30
60
90
0
30
60
90
$\theta_{c.m.}$ (deg)

the distributions for the two reactions.

The angular distributions of states belonging to a given rotational band* are grouped together in figs. 12-15, and the corresponding bands in the mirror nuclei, ^{23}Na and ^{23}Mg, are shown beside one another. While the (d, ^{3}He) reaction cross sections differ in magnitude with those of the (d,t) reaction, they generally agree in shape.

2. DWBA Analysis. Several characteristics of the angular distributions suggest that the reaction mechanism is not the simple process treated by the usual DWBA (see Appendix B). In a single-step direct reaction one expects the angular distributions characterized by the same orbital angular momentum (ℓ) transfer to be similar in shape unless the energies of the scattered particles differ greatly. However, the data shows rather pronounced differences for expected ℓ = 2 transitions within the different bands. To check agreement with experiment DWBA calculations were performed for the (d, ^{3}He) reaction for ℓ = 2 transitions to the ground-state, 0.44 and 2.98-MeV levels using a spherical optical model potential for the incident deuterons. As shown in fig. 11, each prediction has essentially the same shape. The fit for the $^{5}/_{2}^{+}$ transition to the first excited state is rather good. Although the DWBA calculation for the ground-state (only 440 keV away in excitation energy) is reasonable at forward angles, it fails to predict the nearly isotropic behavior at back angles.

---

*In a few cases the spin assignments are not rigorous. These will be discussed in Section 5.

The prediction for the 2.98-MeV $(3/2^+)$ state does not describe the shape of any portion of the angular distribution. The poor agreement with the data indicates a failure of the usual DWBA and the necessity for an alternate description of the reaction.

Another striking feature of the data is the large cross section to the "j-forbidden" $7/2^+$ and $9/2^+$ states of the ground-state band. As will be seen in Chapter IV, the Nilsson model predicts the spectroscopic factors for these transitions to be zero if the configuration basis is restricted to the sd-shell or to be ~ 0.0003 if a $g_{7/2}$ component is included. The DWBA calculation performed for the (d, ^{3}He) transition to the $7/2^+$ state at 2.08 MeV is shown in fig. 11. The result does not give satisfactory agreement with the angular distribution and requires a spectroscopic factor two orders of magnitude larger than predicted. Since it was necessary to include all spectroscopic amplitudes into the CCBA cross section calculations (see next section), the spectroscopic amplitudes for direct transitions were included in the DWBA predictions to facilitate comparisons. An additional factor which multiplies the prediction is also indicated for each curve. If the reaction theory and spectroscopic amplitudes from the nuclear model were exact, then this factor would be unity.

Since the $g_{7/2}$ state is unbound for any reasonable spherical potential in this mass region, it was necessary to use an unrealistic well depth of $\sim$ 160 MeV to obtain the experimental separation energy for this state. Consequently, the amplitude of the wavefunction inside the well used in the DWBA analysis was unreasonably large requiring that the normalized wavefunction

have smaller amplitude in the exponential tail. Since direct reactions, pictured as taking place near the nuclear surface, are particularly sensitive to the bound state wavefunction in this region, the calculation probably has underestimated the cross section for the $^{7}/_{2}^{+}$ transfer.

As discussed in Chapter IV, a more realistic form factor may be calculated by solving the Schrödinger equation for a particle bound in a deformed potential well with a Woods-Saxon shape (E. Rost, 1966). The deformation of the core mixes higher angular momentum components into the single particle states. D. Dehnhard et al. (1967) found that the cross section calculation for the "allowed" $^{26}Mg(d,t)^{25}Mg$ $^{5}/_{2}^{+}$ ground-state transition employing the realistic form factor had virtually the same shape as that obtained using the usual spherical well potential, but was 30% lower. However, for the "forbidden" transitions the cross sections calculated with the deformed-well were three times larger. Therefore, the discrepency between the DWBA prediction and the experimental data for the $^{7}/_{2}^{+}$ level of this study is in part due to the unrealistic form factor. Even if this form factor were treated correctly, the measurement would apparently still exceed the DWBA calculation by a factor of at least 10.

3. CCBA Analysis. As discussed in Appendix B, the CCBA provides a more complete description of reaction processes for transitions between nuclei exhibiting strong collective effects. By allowing reactions to be induced by projectiles scattered from inelastic states in the incident channel, the theory includes multi-step processes ignored by the DWBA treatment. Interactions between states in the final nucleus may also be considered.

Inelastic effects contributing to the reaction angular distributions may account for the anomalous characteristics mentioned in the section above. As noted in Section A, the inelastic differential cross section for the 2^+ member of the ground-state band exceeds the elastic scattering beyond 70° in the center of mass. This inelastic process can be pictured as creating a ^{24}Mg target with spin and parity 2^+. With such a target, single nucleon transfers of total angular momentum $j = {}^1/_2, {}^3/_2$ and ${}^5/_2$ (the only possibilities for a basis restricted to the sd-shell) may produce final states with $j = {}^1/_2, {}^3/_2, \cdots, {}^9/_2$. This process is likely to be an important contribution to the population of the "j-forbidden" states, e.g. the ${}^7/_2^+$ level discussed in the DWBA analysis.

Since the deuterons scattering from the virtual 2^+ target are expressed as outgoing spherical waves (Appendix B), any directional dependence of subsequent induced reactions might be expected to be averaged over the angular distribution of the inelastic deuterons. As seen in fig. 7, the 2^+ cross section is not strongly forward peaked as is the elastic scattering. Consequently, the indirect contributions from this 2^+ state will tend to be isotropic. If the states, populated directly by the same angular momentum transfer, have different overlaps with the 2^+ target (i.e. different amounts of the indirect contributions), then, unlike the DWBA predictions, the reaction distributions may be expected to differ in shape. The states with larger indirect contributions will appear more isotropic than those where the direct term dominates.

Since the direct and indirect contributions to the cross sections add coherently, the CCBA calculation is not well suited for the extraction of spectroscopic amplitudes for the various contributions. However, the CCBA provides

an excellent means for evaluating the validity of amplitudes defined by a model through comparisons with experimental angular distributions. The predictions should give agreement for both the shape and magnitude. For the present study the spectroscopic amplitudes were calculated from the Nilsson model with band-mixing as discussed in the next chapter. The results are listed in Table VI.

The form factors for the CCBA calculations were obtained assuming a spherical-well potential with Woods-Saxon shape. As remarked in the last section, a deformed-well would yield more realistic wavefunctions but would differ greatly from those employed here for only the $g_{7/2}$ and $g_{9/2}$ transitions. Since the spectroscopic amplitudes for such transfers were usually an order of magnitude smaller than the other components of the sd-shell, they were omitted from all the calculations shown in figs. 12-15. In the calculation for the level at 2.08 MeV illustrated in fig. 11, the $g_{7/2}$ component was included to give a direct reaction contribution to the cross section in order to estimate the influence of this term. Note that the only difference between the CCBA predictions shown in fig. 12 where the direct term is neglected and that of fig. 11 is a small dip in the angular distribution near 25^{o}. This feature, in fact, produces a better fit to the data. It is tempting to suggest that the more realistic form factor, which will have a slightly larger effect, may even produce better agreement with the data. Of course the main point is that the addition of a $g_{7/2}$ direct term produced essentially a small perturbation, so that omission of these higher angular momentum components for indirect processes is a reasonable approximation.

The numerical calculations for the form factors were performed using the subroutine BIND from the DWBA code DWUCK written by P. D. Kunz (1970). The potential well was chosen to have radius $R_o = 1.25A^{1/3}$ fm, diffuseness a = 0.65 fm, spin-orbit strength $\lambda = 25.0$ and a well depth V_o, adjusted to reproduce the binding energy of the bound particle. This binding energy was taken as the sum of the experimental neutron or proton separation energies from ^{24}Mg for transitions to ^{23}Mg or ^{23}Na, respectively, plus the excitation energy of the final state.

Since there have been no systematic optical model studies of triton scattering in light nuclei, triton parameters for the CCBA analysis could not be obtained from some average potential such as is available for nuclei with mass $A \geq 40$. Of course a direct measurement is not possible as ^{23}Mg is a short-lived radioactive nucleus. Hence the same ^{3}He parameters were applied to describe the scattering in the exit channel for both the (d,t) and (d,^{3}He) reactions. This approach seems reasonable since the product nucleus and scattered projectile for one reaction form a binary system that is the charge conjugate of the other. In each reaction the nuclear interaction (represented by the Woods-Saxon potentials) is pictured to be the same, the only difference arising from Coulomb effects. Dzubay (1971) adopted this approach in the analysis of the (d,t) and (d,^{3}He) reactions on ^{32}S and obtained excellent agreement with experiment.

The optical model parameters for the CCBA analysis were selected from the parameter ambiguities of figs. 8 and 10. Comparisons of data and

CCBA calculations with ^{3}He parameters corresponding to real well depths V_{He} = 130 through 180 MeV all indicated a definite preference for deuteron parameters with $V_d \sim 100$ MeV. After choosing the optimum deuteron set with V_d = 105 MeV, additional calculations with various ^{3}He parameter sets showed the best agreement with the data when V_{He} = 150 MeV. A variety of perturbations on these optical model parameters indicated that the reasonable fits illustrated in figs. 12-15 could not be significantly improved by deviating from the elastic (and inelastic) descriptions. The parameters adopted for the analysis are listed in Table I.

The spectroscopic amplitudes, form factors and optical parameters served as input to the computer code MARS (T. Tamura, 1971) which performed the numerical computations of the CCBA. In this calculation the JUPITOR program is called as a subroutine to calculate the coupled-channel wavefunctions. The routine OVRLAP then combines the spectroscopic amplitudes and form factor with the wavefunctions, calculates the transition amplitudes defined in Appendix B and, finally, evaluates the cross sections. The input to MARS may be specified so that it performs the regular DWBA calculation. The DWBA curves shown in fig. 11 were produced in this way so that the calculations illustrated there were subjected to essentially identical numerical methods so that comparisons are meaningful.

Finally, it must be noted that the present analysis does not include any inelastic effects in the exit channel. This approximation yields a great simplification since reactions populating different final state may be considered independent. Thus one has no difficulty with the problem of interband coupling

Table I. Optical-Model Parameters

Channel	E_{lab} (MeV)	β	V (MeV)	r_o (fm)	a_o (fm)	W (MeV)	W_D (MeV)	r_i (fm)	a_i (fm)	r_C (fm)
$^{24}Mg + d$	21.1	0.46	105.	1.041	.963	...	15.0	1.31	.629	1.30
$^{24}Mg + d$	21.1	0.00	100.	0.928	0.918	...	26.7	1.32	.664	1.30
$^{23}Na + ^{3}He$	15.0	0.00	150.	1.244	.650	18.8	...	1.43	.921	1.40

Note (a): The deformation parameter, β, is denoted as 0.0 for channels where inelastic scattering was neglected; (b): Optical-model parameters for $^{23}Na + ^{3}He$ were also adopted for the $^{23}Mg + t$ channel.

among the final states as treated by P. L. Ottaviani et al. (1970). The evidence that the inelastic ^{3}He scattering from the low-lying coupled states constituted only a small portion of the total absorption process suggests that the simplification applied here will not introduce large errors.

4. Comparison of DWBA and CCBA. As remarked earlier, the optical model parameters for deuterons shown in fig. 8 demonstrate a strong parallel between the spherical and deformed potentials. This feature enabled the selection of "equivalent" potentials, i.e. spherical and deformed potentials which describe elastic (and inelastic) scattering and which correspond to approximately the same point in parameter space along Vr^n ambiguity. The latter requirement is quite important since the cross section predictions of DWBA and CCBA vary along the ambiguity.

The DWBA and CCBA predictions displayed in fig. 11 were calculated with equivalent potentials. Although the fit to the $^{5}/_{2}^{+}$ state was acceptable, the overall DWBA analysis produced a rather poor description for reactions populating the four levels illustrated. The predictions using coupled-channel wavefunctions with only direct terms gave essentially the same poor results. However, by including the indirect terms in the full CCBA calculation, reasonable agreement was obtained for all levels. Of course, the most spectacular success of the CCBA treatment was the prediction of the correct shape and magnitude for the $^{7}/_{2}^{+}$ distribution which exhibited such violent disagreement with experiment without the indirect contributions.

Like the $^{7}/_{2}^{+}$ level, the $^{3}/_{2}^{+}$ ground-state distribution experienced a dramatic change in shape and moderate change in amplitude upon the introduction of rather large indirect components (see Table VI). This change was not a complete success since the forward stripping peak was reduced with respect to the second maximum so as to fall beneath the data. In a discussion given in Chapter V, it is shown that by increasing the amplitude of the direct contribution one calculates an angular distribution in agreement with the data.

In fig. 11 each theoretical cross section for the 0.44-MeV state produced a reasonable fit to the data. For this case the agreement can be explained in terms of the lack of indirect scattering. As seen in Table VI, this $^{5}/_{2}^{+}$ level has a very large direct term and only weak indirect contributions. Hence the reaction was essentially direct, and the good DWBA fit merely reflected the validity of that approximation for this transition.

The calculations shown for the 2.98-MeV level are similar to those for the ground-state transition. Both indicate that the indirect terms tend to make the predictions more isotropic, particularly at the back angles where the direct terms are weak.

5. J^{π} Assignments and Spectroscopic Factors. The computer code MARS which performed the CCBA calculations evaluated the expression

$$\frac{d\sigma}{d\Omega} = \frac{D_o^2 \gamma_c^2}{2s + 1} \, d\sigma_t$$

where $d\sigma_t$ is proportional to the theoretical cross section. The spectroscopic amplitudes for the transitions are included in the definition of $d\sigma_t$. The factor

D_o^2 is the normalization constant for the reaction, and is defined in the code with the values 2.99 and 3.37 for the (d, ^{3}He) and (d,t) reactions, respectively. The factor $\gamma c^2/(2s + 1)$ was unity for these reactions. All these quantities are discussed in Appendix B.

On the basis of the CCBA fits it was possible to obtain new assignments or limits for six states in ^{23}Mg through identification with the mirror states in ^{23}Na. To establish a pair of states as analogs, it was necessary that the CCBA predictions give reasonably good fits for both angular distributions. The CCBA calculations for each member of the pair employed the same direct and indirect coupling, the same spectroscopic amplitudes and, of course, the same final state J^π. The additional normalization factor, N, which is given with each curve in figs. 12-15 also had nearly the same value for mirror states.

The assignments of $^9/_2^+$, $^3/_2^+$, $(^7/_2^+)$ and $(^5/_2^+)$ were established for levels at 2.71, 2.90, 4.68 and 5.29 MeV by identification with the mirror states of known J^π at 2.71, 2.98, 4.78 and 5.38 MeV (A. R. Poletti et al., 1970). The determination of these mirror states was considerably simplified as there were no angular distributions with similar shapes and magnitudes lying near in excitation energy. However, the neighboring states at 3.86 and 3.97 MeV in ^{23}Mg had shapes that were similar and magnitudes that differed by approximately a factor of 2. This factor indicated that the 3.86- and 3.97-MeV levels were the mirror states of the $^5/_2^+$, and $^5/_2^-$ levels in ^{23}Na at 3.92 and 3.85 MeV, respectively. If these assignments were reversed, the normalization factors, N, would not agree as they should for mirror states.

As mentioned earlier, the spectroscopic amplitudes for the various direct and indirect couplings are included in the CCBA calculations. However, for the allowed transitions the angular distribution at forward angles is primarily determined by the direct transition (see Chapter V). Thus, it is possible to extract spectroscopic factors that are essentially equivalent to those obtained from the usual DWBA analysis. These factors and the J^{π} assignments are summarized in Table II. The spectroscopic factors from related experiments and the theoretical predictions of the Nilsson model are also indicated.

Table II. Spectroscopic Results of the $^{24}Mg(d,^3He)^{23}Na$ and $^{24}Mg(d,t)^{23}Mg$ Reactions and Predictions of the Nilsson Model

Energy ^{23}Na (MeV)	Energy ^{23}Mg (MeV)	Spin and Parity I^π	C^2S $(d,^3He)$ a)	C^2S (d,t) a)	C^2S $(d,^3He)$ b)	C^2S $(d,^3He)$ c)	C^2S (p,d) d)	$(2I+1)C^2S$ $(^3He,d)$ e)	Nilsson Model K^π	Nilsson Model C^2S f) Unmixed	Nilsson Model C^2S f) Mixed
0.00	0.00	$3/2^+$	0.26 g	0.33 g	0.24	0.47	0.36	0.32	$3/2^+$	0.048	0.052
0.44	0.45	$5/2^+$	2.3	2.3	3.78	2.90	2.83	2.10	$3/2^+$	1.32	2.28
2.08	2.05	$7/2^+$							$3/2^+$	0.003	0.003
2.39	2.36	$1/2^+$	0.16	0.16	0.30	0.25	0.10	0.50	$1/2^+$	0.12	0.10
2.64	2.77	$1/2^-$	1.6	2.3	2.64	2.10	1.70	0.043	$1/2^-$	1.76	1.76
2.71	2.71	$9/2^+$							$3/2^+$	0.027	0.057
2.98	2.90	$3/2^+$	0.16	0.15	0.17	0.34		1.28	$1/2^+$	0.20	0.25
3.68	3.79	$3/2^-$	0.43	0.36	0.93	0.85	0.85	0.076	$1/2^-$	0.24	0.24
3.85	3.97	$(5/2^-)$							$1/2^-$	0.00	0.00
3.92	3.86	$5/2^+$	0.013	0.013	0.02			0.27	$1/2^+$	0.072	0.006
4.43	4.35	$1/2^+$	0.070	0.048	0.12	0.08	0.05	0.006	$1/2^+$	0.41	0.43
4.78	4.68	$(7/2^+)$							$1/2^+$	0.003	0.005
5.38	5.29	$(5/2^+)$	0.055	0.041	0.49	0.42	0.27	0.074	$1/2^+$	1.49	0.50

[a] Present study. Here $C^2S = N A^2_{\ell I}(2I+1)$ where N is the additional normalization factor indicated for each curve in figs. 12-15. The $A_{\ell I}$ are the direct transition spectroscopic amplitudes listed in Table VI.

[b] E. Krämer et al. (1971).

[c] M. Arditi et al. (1971).

[d] R. L. Kozub (1968).

[e] J. R. Powers et al. (1971).

[f] $C^2S = (2I+1)\,A^2_{\ell I}$.

[g] Here $A_{\ell I} = 3A_{\ell I}$ of Table VI (see Chapter V). N is taken from fig. 18.

Chapter IV

COLLECTIVE MODEL CALCULATIONS

A. Formalism of the Collective Model

The predictions of the strong-coupling model for deformed nuclei have enjoyed considerable success in the description of the static and dynamic properties of light nuclei with $19 \leq A \leq 25$ as well as the heavier deformed nuclei. Previous studies of ^{23}Na (J. Dubois, 1967[a]) and of ^{23}Mg (L. C. Haun et al., 1970, and J. Dubois et al., 1967[b]) have shown that the Nilsson model gives improved agreement with data when bandmixing is included. Excellent accounts of the model have been given by Nilsson (1955), Davidson (1965), Webb (1968) and Haun (1968). Only the features most relevant to this study will be included here.

1. Basic Concepts. The strong-coupling model applied to an odd-A nucleus pictures the odd nucleon moving in a potential well with permanent deformation. This potential formed by all the other core nucleons is assumed to exhibit only low frequency oscillations in shape so that the odd nucleon may follow its motion adiabatically.

The total angular momentum of the nucleus, $\vec{I}$, a constant of motion,

is formed as $\vec{I} = \vec{L} + \vec{j}$ where $\vec{L}$ is the angular momentum of the core and $\vec{j}$ is angular momentum of the odd nucleon consisting of an orbital part, $\vec{\ell}$, and an intrinsic part, $\vec{s}$. The projection of $\vec{I}$ and $\vec{j}$ along the body-fixed z axis is defined to be K and Ω, respectively. In the space-fixed system the projection of $\vec{I}$ along the z′ axis is denoted as M. The coupling of these angular moments is represented in the following diagram.

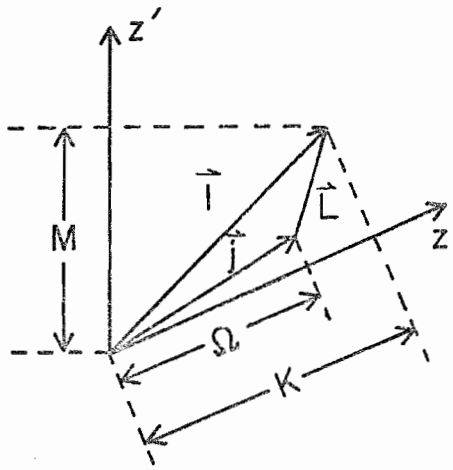

The most general deformation potential has neither spherical nor axial symmetry so that $\vec{I}$ remains the only constant of motion. However, to obtain a simple model one usually considers a potential with axial symmetry and reflection symmetry through a plane perpendicular to this axis. With this assumption K = 0. This follows since even-even spherical nuclei do not show rotational spectra and therefore do not rotate about a symmetry axis. Hence the angular momentum about a symmetry axis, L_z, is assumed to vanish so that $K = \Omega$, and Ω is a constant.

The total Hamiltonian for this system may be written as the sum of the kinetic energy of the rotational core plus the Hamiltonian for the odd particle,

$$H = H_r + H_p \qquad (1)$$

H_r may be expressed in terms of the moments of inertia, $\mathcal{I}_i$, as

$$H_r = \sum \frac{\hbar^2}{2\mathcal{I}_i} L_i^2 = \frac{\hbar^2}{2\mathcal{I}} \vec{L}^2 + \left(\frac{\hbar^2}{2\mathcal{I}_z} - \frac{\hbar^2}{2\mathcal{I}}\right) L_z^2$$
$$= \frac{\hbar^2}{2\mathcal{I}} \left(\vec{I} - \vec{j}\right)^2 \qquad (2)$$

Here the condition for axial symmetry has been applied which requires $\mathcal{I}_x = \mathcal{I}_y \equiv \mathcal{I}$. Using eq. (2) in eq. (1), H may be written as

$$H = H_{rot} + H_{part} + H_{couple} \qquad (3)$$

where

$$H_{part} = H_p + \frac{\hbar^2}{2\mathcal{I}} \vec{j}^2$$
$$H_{rot} = \frac{\hbar^2}{2\mathcal{I}} (\vec{I}^2 - 2I_z^2) \qquad (4)$$
$$H_{couple} = -\frac{\hbar^2}{2\mathcal{I}} (I_+ j_- + I_- j_+)$$

The $I_\pm$ and $j_\pm$ operators are identified with the raising and lowering operators defined by $t_\pm = t_x \pm i t_y$.

To calculate wavefunctions for the total Hamiltonian, one first solves the separable problem obtained by omitting the coupling term,

$$(H_{rot} + H_{part}) \Phi^I_{MK} = E_{IK} \Phi^I_{MK} \qquad (5)$$

The appropriate symmetrized wavefunction may be expressed (R. R. Roy et al., 1967, and S. G. Nilsson, 1955) as

$$\Phi^I_{MK} \equiv |IMK(=\Omega)\rangle = \sqrt{\frac{2I+1}{16\pi^2}} \left[\phi_\Omega(\vec{r}) D^I_{MK}(\theta,\phi) + (-1)^{I-j} \phi_{-\Omega}(\vec{r}) D^I_{M-K}(\theta,\phi)\right] \qquad (6)$$

where $D^{I}_{MK}(\theta, \phi)$, eigenfunctions of H_{rot}, express the rotation of the body-fixed coordinates of the core relative to the laboratory reference frame. The single particle wavefunction ϕ_{Ω} satisfies

$$H_{part}\,\phi_{\Omega}(\vec{r}) = E_{o}^{\Omega}\,\phi_{\Omega}(\vec{r}) \tag{7}$$

where the radius vector $\vec{r}$ is defined in the body-fixed frame. E_{o}^{Ω} is the binding energy of the particle within the system defined by H_{part}. From the properties of the D^{I}_{MK} given in Rose (1957), we may conclude

$$E_{IK} = E_{o}^{\Omega} + \frac{\hbar^2}{2\mathcal{I}}\left[I(I+1) - 2K^2\right] \qquad I \geq K \tag{8}$$

The E_{IK} of eq. (8) define the energy spectrum of a rotational band built upon a single particle state of energy E_{o}^{Ω}.

2. Nilsson Wavefunctions. The solution to the bound state problem represented by eq. (7) was discussed by Nilsson (1955). In this model the Hamiltonian for the odd nucleon is written

$$H_{part} = H_{o} + C\,\vec{\ell}\cdot\vec{s} + D\,\vec{\ell}^{\,2} \tag{9}$$

where

$$H_{o} = \frac{p^2}{2m} + \frac{m}{2}\left[\omega_{x}^{2}(x^2+y^2) + \omega_{z}^{2}z^2\right]$$

H_{o} is the Hamiltonian of a particle in a anisotropic harmonic oscillator potential with frequency parameters $\omega_{x} = \omega_{y}$ (for axial symmetry) and ω_{z}. The constants C and D are additional parameters of the model. After some algebraic manipulations, H_{part} may be expressed as

$$H_{part} = H^{HO}_{diag} + H^{HO}_{couple} \tag{10}$$

where H^{HO}_{diag} is the Hamiltonian for the isotropic harmonic oscillator. The wavefunction ϕ_Ω may be expanded as

$$\phi_\Omega = \sum_{j'} C_{j'\Omega} | N j' \Omega \rangle \tag{11}$$

The harmonic oscillator states, $| Nj\Omega \rangle$, forming the basis need not be restricted to a single oscillator level, N, since H^{HO}_{couple} connects states with N differing by two. However, Nilsson did not include this major shell mixing in his calculation.

After substituting eq. (11) into eq. (7), multiplying it by $\langle Nj\Omega|$ from the left, integrating over all coordinates and collecting terms in $C_{j\Omega}$ on the right, one obtains

$$\sum_{j'} \langle N j \Omega | H^{HO}_{couple} | N j' \Omega \rangle = (E^{\Omega}_{o} - E^{N}_{o}) C_{j\Omega} \tag{12}$$

where E^{N}_{o} is defined as

$$H^{HO}_{diag} | N j \Omega \rangle = E^{N}_{o} | N j \Omega \rangle \tag{13}$$

To complete the calculation of ϕ_Ω it is necessary to evaluate the matrix elements of eq. (12) and then to perform the matrix diagonalization thereby determining the values for $C_{j\Omega}$ and E^{Ω}_{o}.

The parameters C, D, ω_x and ω_z of eq. (9) are usually defined in terms of four other parameters, κ which determines the spin-orbit splitting, μ which determines the depression of higher ℓ levels, η the core deformation, and $\hbar\omega_o$ the spacing of harmonic oscillator levels. The equations which relate the two sets of parameters are given by Nilsson (1955). The parameters are chosen for each shell to produce energy levels and wavefunctions which give

optimum agreement with experiment.

Figure 16 shows the energy levels, E_o^{Ω}, for the orbits available to a single particle as a function of the nuclear deformation η. This figure is taken from the work of A. J. Howard et al. (1965). Each level is identified by the shell model quantum numbers, ℓ_j, at zero deformation and by $\Omega^{\pi}\,[\,Nn_z\,\Lambda\,]$ at prolate deformations. A description of the pseudo quantum n_z and Λ is given by Preston (1962). The Nilsson orbit numbers are also indicated for each level illustrated in fig. 16.

3. Coupled-Channel Wavefunctions. An alternate solution to the bound state problem was developed by E. Rost (1966) using a more realistic deformed potential with Woods-Saxon shape. For this model the single particle Hamiltonian is written as

$$H_{part} = \frac{p^2}{2m} - \lambda\left(\frac{\hbar}{2m_pc}\right)^2 2\,\vec{l}\cdot\vec{s}\;\frac{1}{r}\frac{dV(r)}{dr} + V(r,\theta) \qquad (14)$$

where m_p is the proton mass. The spin-orbit term is characterized with strength λ and is taken to be spherical with

$$V(r) = \frac{-V_o}{1+\exp[(r-R_o)/a]} \qquad (15)$$

The deformed potential V(r, θ) is obtained from eq. (15) by assuming

$$r \rightarrow r_o\left[1+\beta\,Y_{20}(\theta) - \beta^2/4\pi\right]$$

so that

$$V(r,\theta) \equiv V(r_o) = V\left(r/\left[1+\beta\,Y_{20}(\theta) - \beta^2/4\pi\right]\right) \qquad (16)$$

Figure 16. Energy levels of the Nilsson model. This diagram shows the energy levels, E_o^{Ω}, for a single particle in a Nilsson potential as a function of the deformation η. Each level is identified by the shell model quantum numbers, ℓ_j, at zero deformation, the $\Omega^{\pi}\left[Nn_z\Lambda\right]$ at prolate deformation and the Nilsson orbit numbers. The solid lines in the figure represent the positive parity orbits and the dashed lines the negative parity orbits. This figure was taken from the work of A. J. Howard et al. (1965).

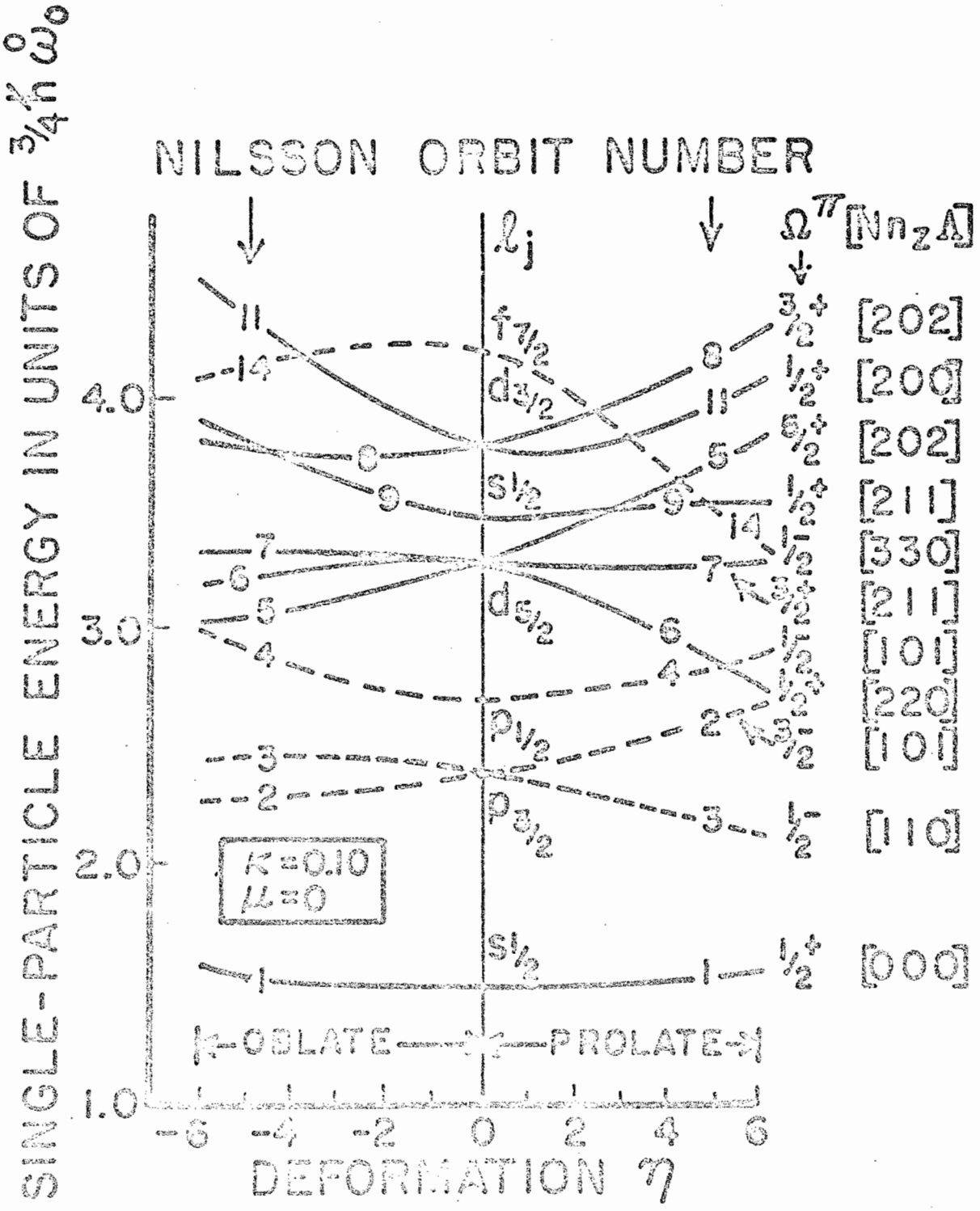
NILSSON ORBIT NUMBER
SINGLE-PARTICLE ENERGY IN UNITS OF $\frac{3}{4}\hbar\omega_0$
ℓ_j
Ω^π [Nn$_z$Λ]
$f_{7/2}$
$d_{3/2}$
$s_{1/2}$
$d_{5/2}$
$p_{1/2}$
$p_{3/2}$
$s_{1/2}$
$\frac{3}{2}^+$ [202]
$\frac{1}{2}^+$ [200]
$\frac{5}{2}^+$ [202]
$\frac{1}{2}^+$ [211]
$\frac{1}{2}^-$ [330]
$\frac{3}{2}^+$ [211]
$\frac{1}{2}^+$ [101]
$\frac{1}{2}^+$ [220]
$\frac{3}{2}^-$ [101]
$\frac{1}{2}^-$ [110]
$\frac{1}{2}^+$ [000]
κ=0.10
μ=0
κ-OBLATE
PROLATE-κ
4.0
3.0
2.0
1.0
-6 -4 -2 0 2 4 6
DEFORMATION η

The deformation parameter β , is analogous to η of the last section. This expansion differs from that presented for the scattering potentials in Appendix B in that eq. (16) preserves a constant volume. The potential $V(r, \theta)$ may be written as

$$V(r, \theta) = V_{diag}(r) + V_{couple}(r, \theta)$$

so that the single particle Hamiltonian may be expressed as

$$H_{part} = H^{WS}_{diag} + H^{WS}_{couple}$$

in analogy with the result for the Nilsson model.

One could now obtain the bound state wavefunction ϕ_Ω by expanding in terms of the usual normalized Woods-Saxon wavefunctions of the spherical operator H^{WS}_{diag} as in eq. (11). However, since the high angular momentum wavefunction of the basis could be unbound, Rost chose to expand ϕ_Ω as

$$\phi_\Omega = r^{-1} \sum u_{j'\Omega}(r) |j'\Omega\rangle \qquad (17)$$

where $|j'\Omega\rangle$ represents the angular momentum part of each term. Substituting eq. (17) into the Schrödinger eq. (7), multiplying it by $\langle j\,\Omega|$ from the left and integrating over the angular coordinates, one obtains the set of coupled differential equations

$$\left\{ -\frac{\hbar^2}{2m}\left(\frac{d^2}{dr^2} - \frac{l(l+1)}{r^2}\right) - \lambda(j^2 - l^2 - s^2)\left(\frac{\hbar}{2m_p c}\right)^2 \right.$$
$$\left. \times \frac{1}{r}\frac{dV(r)}{dr} + V_{diag}(r) - E_0^{\Omega} \right\} u_{j\Omega}(r) \qquad (18)$$
$$= -\sum_{j'} \langle j\Omega | V_{couple}(r, \theta) | j'\Omega \rangle u_{j'\Omega}(r)$$

The radial wavefunctions $u_{j\Omega}(r)$ obtained from the numerical solution of eq. (18) are generally not normalized to unity. For comparison with the Nilsson model, one defines $C_{j\Omega}$ for this model as

$$C^2_{j\Omega} = \int_0^\infty [u_{j\Omega}(r)]^2 dr$$

where the sign of $C_{j\Omega}$ must be determined from the value of ℓ and numbers of nodes in the radial wavefunction $u_{j\Omega}(r)$. Rost found that the coefficients $C_{j\Omega}$ and eigenenergies E obtained from this coupled-channel calculation do not differ greatly from those obtained from the simpler Nilsson model.

The great significance of this model is that one obtains "realistic" wavefunctions for the higher angular momentum components which would be unbound in any equivalent spherical Woods-Saxon potential. Also by considering a finite well as opposed to the harmonic oscillator potential which has no unbound states, the wavefunctions ϕ_Ω are well suited for use as form factors in DWBA calculations. In fact when the coupled-channel calculation was performed to obtain a form factor, the well depth of the deformed potential was adjusted to predict the experimental separation energy of the bound state, and therefore to exhibit the correct asymptotic form of $u_{j\Omega}(r)$. The amplitude of a DWBA prediction is most sensitive to this critical region.

4. Wavefunctions with Bandmixing. Having developed expressions for wavefunctions, $\mathcal{J}^{I}_{MK}$, which describe rotational bands without mixing, the "rotational-particle-coupling" or bandmixing term, H_{couple}, is now included in the interaction Hamiltonian. To calculate the total wavefunctions, $\mathcal{J}^{I}$, which

satisfy

$$H \underline{\Phi}^{I} = (H_{rot} + H_{part} + H_{couple}) = E_I \underline{\Phi}^{I} \qquad (19)$$

one expands $\underline{\Phi}^{I}$ in terms of $\underline{\Phi}^{I}_{MK}$ so that

$$\underline{\Phi}^{I} = \sum_{K'} \alpha_{IK'} | I M K' > \qquad (20)$$

Following the procedures applied for the calculation of the $C_{j\Omega}$ for Nilsson wavefunctions, one obtains α_{IK} and the energies, E_I, through solving the eigenvalue problem represented by

$$\sum_{K'} <I M K| H_{couple} | I M K'> \alpha_{IK'} = (E_I - E_{IK}) \alpha_{IK} \qquad (21)$$

The matrix element of eq. (21) is given by Davidson (1965) as

$$<I M K| H_{couple} | I M K'> = -\frac{\hbar^2}{2\mathcal{I}} \sum_j C^*_{j\Omega'} C_{j\Omega} \qquad (22)$$

$$\times \{ [\delta_{K',K-1} + (-1)^{I-j} \delta_{K',-K+1}] \sqrt{(I+K)(I-K+1)(j+K)(j-K+1)}$$

$$+ \sqrt{(I-K)(I+K+1)(j-K)(j+K+1)}\ \delta_{K',K+1} \}$$

The second term contributes only for bands with $K = 1/2$ and the matrix element is written as

$$<I M 1/2 | H_{couple} | I M 1/2> = (-1)^{I+1/2} \frac{\hbar^2}{2\mathcal{I}} (I + 1/2)\, a$$

where the "decoupling parameter" a is defined as

$$a \equiv \sum_j (-1)^{j+1/2} (j + 1/2) | C_{j\,1/2} |^2$$

Inclusion of this diagonal term in the expression for the energy level spectrum for $K = {}^{1}/_{2}$ bands can reorder the level sequence.

Equation (22) shows that H_{couple} connects two rotational bands of the same parity for which $\Delta K = 1$. This interaction is expected to be important for bands lying near in energy (Kerman, 1956).

5. Spectroscopic Factors for Stripping Reactions. As seen in the discussion in Appendix B, the wavefunction for the final nucleus produced in the stripping reaction A(a,b)B may be expanded as

$$\Phi^{I_B M_B} = \sum_{lj} A_{lj} \left(\Phi^{I_A} \otimes \phi_{lj} \right)_{I_B M_B} \tag{23}$$

$$= \sum_{lj} A_{lj} \sum_{M_A' m_j'} \left(I_A j M_A' m_j' \mid I_B M_B \right) \Phi^{I_A M_A'} \phi_{lj}^{m_j}$$

where (ABab | Cc) is a Clebsch-Gordan coefficient. Multiplying eq. (23) by $\Phi^{I_A M_A}$ from the right and integrating over ξ, the internal coordinates of A, one obtains

$$\int \Phi^{I_B M_B}(\xi, \vec{r}) \, \Phi^{I_A M_A}(\xi) \, d\xi = \sum_{lj} A_{lj} \left(I_A j M_A m_j \mid I_B M_B \right) \phi_{lj}^{m_j} \tag{24}$$

The spectroscopic amplitude, A_{lj}, measures the overlap of the final state with the initial state coupled to the transferred nucleon.

If the target is assumed to be an even-even nucleus with a rotational wavefunction given by

$$\Phi^{I_A} = \sqrt{\frac{2I_A+1}{16\pi^2}} \left[D^{I_A}_{M_A K_A} + (-1)^{I_A+K_A} D^{I_A}_{M_A -K_A} \right] \tag{25}$$

then, using eqs. (20) and (25) in eq. (24), one may identify that

$$A_{lj} = \rho \sqrt{\frac{2I_A+1}{2I_B+1}} \sum_K \alpha_{I_B K} C_{jK} \left(I_A j K_A K_B - K_A \mid I_B K_B \right) \tag{26}$$

where ρ is $\sqrt{2}$ if $K_A = 0$ and unity otherwise. This result is essentially that obtained by Satchler (1958) except that mixed wavefunctions were applied here.

Following the work of S. Yoshida (1961) and S. T. Belyaev (1959), a more realistic wavefunction for the target can be produced by including admixtures of pairs of particles in higher Nilsson orbits, which would imply that the lower orbits are not completely filled. The result of such a treatment changes the spectroscopic amplitude so that for stripping,

$$A_{lj} = \rho \sqrt{\frac{2I_A+1}{2I_B+1}} \sum_k \alpha_{I_B K} U_k C_{jK} \left(I_A j K_A K_B - K_A \mid I_B M_B \right) \tag{27}$$

The factor U_K^2 represents the probability of band K being empty. For the inverse reaction (i.e. a pickup reaction) U_K^2 is replaced with V_K^2, the probability that band K is filled. Clearly, $U_K^2 + V_K^2 = 1$.

B. Numerical Calculations for ^{23}Na and ^{23}Mg

Following the suggestions of earlier studies (Haun et al., 1970;

Figure 17. ^{23}Na and ^{23}Mg energy level diagrams and collective model predictions. The spin and parity assignments for ^{23}Na are taken from A. R. Poletti et al. (1970), and those for ^{23}Mg are obtained from the present study and the work of L. C. Haun et al. (1970). The energy spectrum predicted by the Nilsson model with bandmixing is also illustrated.

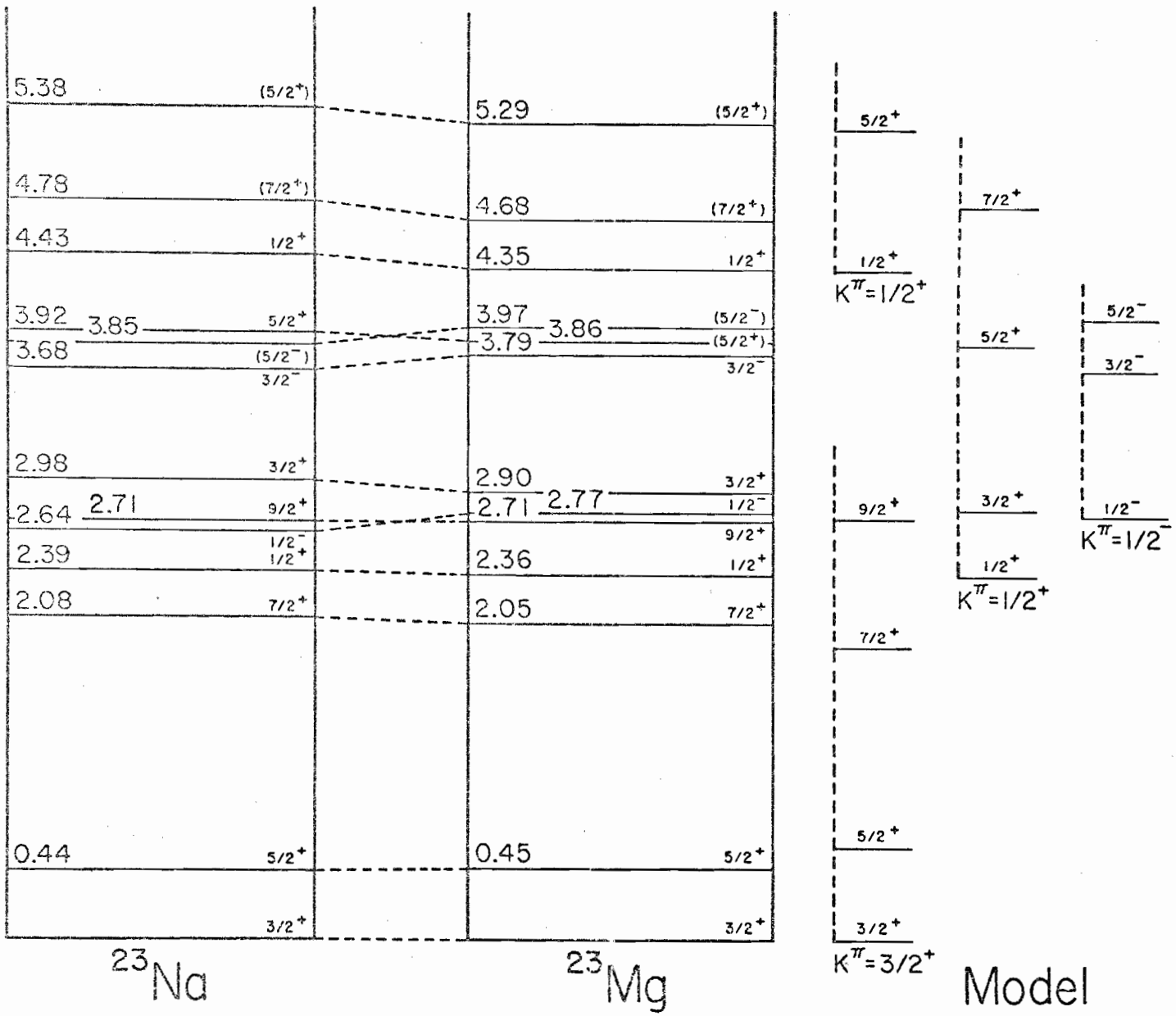
5.38 (5/2+)
4.78 (7/2+)
4.43 1/2+
3.92 3.85 5/2+
3.68 (5/2−)
3/2−
2.98 3/2+
2.64 2.71 9/2+
1/2−
2.39 1/2+
2.08 7/2+
0.44 5/2+
3/2+
23Na
5.29 (5/2+)
4.68 (7/2+)
4.35 1/2+
3.97 3.86 (5/2−)
3.79 (5/2+)
3/2−
2.90 3/2+
2.71 2.77 1/2−
9/2+
2.36 1/2+
2.05 7/2+
0.45 5/2+
3/2+
23Mg
5/2+
1/2+
Kπ=1/2+
9/2+
7/2+
5/2+
3/2+
Kπ=3/2+
7/2+
5/2+
3/2+
1/2+
Kπ=1/2+
5/2−
3/2−
1/2−
Kπ=1/2−
Model

Dubois, 1967[a]), the level structure of the ^{23}Na and ^{23}Mg nuclei are described by rotational bands built upon various Nilsson single-particle levels as shown in fig. 17. The ground-state and lowest $K^{\pi} = {}^{1}/_{2}^{+}$ band are pictured as one particle in the ${}^{3}/_{2}^{+}\,[211]$ or ${}^{1}/_{2}^{+}\,[211]$ orbit, respectively, moving about a ^{22}Na core (see fig 16). The second $K^{\pi} = {}^{1}/_{2}^{+}$ band consists of one particle from the ${}^{1}/_{2}^{+}\,[220]$ orbit of the core moved up and paired with the nucleon in the ${}^{3}/_{2}^{+}\,[211]$ level. Such a configuration is termed a hole-state. The other positive parity bands considered for this model are formed by particles in orbits ${}^{5}/_{2}^{+}\,[202]$ and ${}^{1}/_{2}^{+}\,[200]$. Only one negative parity band need be included in the description of the low-lying states. It was pictured as a hole in orbit ${}^{1}/_{2}^{-}\,[101]$.

Applying the formalism developed in Section A, wavefunctions and spectroscopic amplitudes were calculated for the low-lying states of ^{23}Na and ^{23}Mg. For the positive parity bands, the coefficients $C_{j\Omega}$ defining the unmixed wavefunctions were taken from the work of Dehnhard et al. (1967). They employed the coupled-channel calculation due to Rost with a deformed Woods-Saxon potential with depth $V_o = 57$ MeV, radius $R_o = 1.25A^{1/3}$, diffuseness $a = 0.65$ fm, spin-orbit strength $\lambda = 25.0$ and deformation parameter $\beta = 0.35$. Even parity states from the $1d_{5/2}$ to the $1g_{9/2}$ shell were used as the basis for the expansion. The resulting coefficients are listed in Table III. The $C_{j\Omega}$ for the negative parity states (also listed in Table III) were calculated from the Nilsson model with $\eta = 4$, $\kappa = 0.10$ and $\mu = 0.16$ using a basis from the p-shell.

Values for the rotational energy parameters $A = \hbar^2/2\mathcal{I}$ and band head energies E_o^{Ω} were taken as parameters for each band in the band mixing calculations, and were adjusted to give a reasonable description of the experimental

Table III. Values of the Nilsson Coefficients, $C_{j\Omega}$

$\Omega^{\pi}[Nn_z\Lambda]$ / l_j	$1/2^+[220]$ [a]	$3/2^+[211]$ [a]	$1/2^+[211]$ [a]	$5/2^+[202]$ [a]	$1/2^+[200]$ [a]	$1/2^-[101]$ [b]
$s_{1/2}$ $(p_{1/2})$ [e]	-0.452	0.0	-0.548	0.0	-0.705	0.938
$d_{3/2}$ $(p_{3/2})$ [e]	-0.180	-0.193	-0.711	0.0	0.665	0.347
$d_{5/2}$	0.864	0.970	-0.425	0.993	-0.222 [c]	0.0
$g_{7/2}$	-0.028	-0.044	-0.086	-0.042	0.099 [d]	0.0
$g_{9/2}$	0.130	0.138	-0.080	0.115	-0.048	0.0

[a] Dehnhard et al. (1967) using deformed Woods-Saxon potential.

[b] Calculation with simple Nilsson model using anisotropic harmonic oscillator potential.

[c] Listed by Dehnhard et al. (1967) as + 0.222

[d] Listed by Dehnhard et al. (1967) as + 0.99

[e] P-shell basis for negative parity states

energy spectrum for ^{23}Mg. Since the energy positions of the $^{5}/_{2}^{+}[202]$ and $^{1}/_{2}^{+}[200]$ bands are uncertain in ^{23}Mg, these bands were assumed to have the energies of the corresponding band identified in ^{23}Na. The search over A for each band is justified since the rotational bands of different single particle states are thought to have different deformations (Howard, 1965), and therefore may have different moments of inertia. The parameters (including the occupation probability V_K^2) used in the bandmixing calculation are listed in Table IV.

The energy levels and expansion coefficients obtained from the diagonalization of eq. (21) are listed in Table V. Comparisons with the experimental levels shown in fig. 17 indicate good agreement may be realized without using widely different A parameters.

To obtain the spectroscopic amplitudes, $A_{\ell j}$, for single nucleon transfer reactions necessary for the CCBA predictions, the bandmixing calculation was performed twice, once for target $J^\pi = 0^+$ and again for $J^\pi = 2^+$. For the inverse reaction B(b,a)A the coupled-channel code MARS required that the $A_{\ell j}$ be calculated from eq. (27) with the roles of A and B interchanged. Hence the $A_{\ell j}$ listed in Table VI differ from the usual values by a factor of $\sqrt{(2I_A + 1)/(2I_B + 1)}$.

All bandmixing calculations were performed with the code BANDMIX written by E. J. Erskine (1970).

Table IV. Parameters Used in Bandmixing Calculations

$\Omega^{\pi}[Nn_z\Lambda]$	$A = \hbar^2/2\mathcal{I}$ (MeV)	E_o^{Ω} (MeV)	V_K^2 [a]
$^1/_2^+$ [220]	0.20	4.23	1.00
$^3/_2^+$ [211]	0.21	0.0	0.70
$^1/_2^+$ [211]	0.19	2.28	0.20
$^5/_2^+$ [202]	0.18	5.50 [b]	0.08
$^1/_2^+$ [200]	0.17	6.17 [b]	0.02
$^1/_2^-$ [101]	0.19	2.77	1.00

[a] Guessed values.

[b] Adjusted to reproduce the band head energies of ^{23}Na.

Table V. Positive Parity Energy Levels and Mixing Coefficients, α_{IK}, Predicted by the Nilsson Model Including Bandmixing

Nilsson Orbit	Energy E (MeV)	Spin and Parity I^{π}	α_{IK}				
			$^{3}/_{2}^{+}[211]$	$^{1}/_{2}^{+}[211]$	$^{1}/_{2}^{+}[220]$	$^{5}/_{2}^{+}[202]$	$^{1}/_{2}^{+}[200]$
$^{3}/_{2}^{+}[211]$	0.00	$^{3}/_{2}^{+}$	0.990	-0.088	0.113	0.000	-0.021
	0.59	$^{5}/_{2}^{+}$	0.934	-0.171	0.274	0.138	-0.061
	1.91	$^{7}/_{2}^{+}$	0.943	-0.155	0.192	0.218	-0.034
	2.74	$^{9}/_{2}^{+}$	0.836	-0.242	0.427	0.221	-0.102
$^{1}/_{2}^{+}[211]$	2.37	$^{1}/_{2}^{+}$	0.000	0.996	-0.052	0.000	0.072
	2.79	$^{3}/_{2}^{+}$	0.076	0.983	0.071	0.000	-0.149
	3.88	$^{5}/_{2}^{+}$	0.192	0.957	-0.055	0.082	0.197
	4.76	$^{7}/_{2}^{+}$	0.108	0.942	0.112	0.059	-0.291
	6.82	$^{9}/_{2}^{+}$	0.224	0.900	0.039	0.203	0.311
$^{1}/_{2}^{+}[220]$	4.35	$^{1}/_{2}^{+}$	0.000	0.051	0.999	0.000	0.007
	6.51	$^{3}/_{2}^{+}$	-0.107	-0.025	0.964	0.000	0.243
	5.25	$^{5}/_{2}^{+}$	-0.185	0.108	0.900	-0.374	0.059
	10.29	$^{7}/_{2}^{+}$	-0.239	-0.138	0.945	0.081	-0.157
	7.84	$^{9}/_{2}^{+}$	-0.227	0.107	0.803	-0.531	0.100

Table V. (continued)

Nilsson Orbit	Energy E (MeV)	Spin and Parity I^{π}	α_{IK}				
			$^{3}/_{2}^{+}[211]$	$^{1}/_{2}^{+}[211]$	$^{1}/_{2}^{+}[220]$	$^{5}/_{2}^{+}[202]$	$^{1}/_{2}^{+}[200]$
$^{5}/_{2}^{+}[202]$	5.80	$^{5}/_{2}^{+}$	-0.234	-0.018	0.332	0.913	0.029
	7.11	$^{7}/_{2}^{+}$	-0.198	-0.005	-0.124	0.971	0.060
	9.34	$^{9}/_{2}^{+}$	-0.440	-0.110	0.405	0.791	0.066
$^{1}/_{2}^{+}[200]$	6.31	$^{1}/_{2}^{+}$	0.000	-0.073	-0.003	0.000	0.997
	6.76	$^{3}/_{2}^{+}$	0.060	0.157	-0.231	0.000	0.958
	7.93	$^{5}/_{2}^{+}$	0.038	-0.209	-0.036	-0.012	0.976
	8.94	$^{7}/_{2}^{+}$	0.040	0.263	0.207	-0.022	0.941
	11.09	$^{9}/_{2}^{+}$	0.072	-0.329	-0.081	-0.042	0.937

Table VI. The Spectroscopic Amplitudes, A_{lj}, Determined from the Nilsson Model with Bandmixing. The A_{lj} are given for Nucleons Coupling to the 0^+ and First 2^+ State of ^{24}Mg

Nilsson Orbit	Energy E (MeV)	Spin and Parity I^π	A_{lj} for $0^+ \otimes I^\pi$	A_{lj} for $2^+ \otimes J^\pi$				
				$1/2^{+(-)}$ a	$3/2^{+(-)}$ a	$5/2^+$	$7/2^+$	$9/2^+$
$3/2^+$ [211]	0.00	$3/2^+$	-0.109	0.027	-0.117	0.787	-0.022	0.000
	0.59	$5/2^+$	0.617	-0.076	0.140	-0.254	-0.022	0.095
	1.91	$7/2^+$	-0.019	0.000	-0.082	-0.548	0.011	0.055
	2.74	$9/2^+$	0.075	0.000	0.000	0.720	0.015	-0.069
$1/2^+$ [211]	2.37	$1/2^+$	-0.228	0.000	-0.301	-0.236	0.000	0.000
	2.79	$3/2^+$	-0.249	0.258	0.231	0.011	-0.035	0.000
	3.88	$5/2^+$	-0.033	-0.229	0.133	0.139	-0.012	-0.015
	4.76	$7/2^+$	-0.024	0.000	-0.289	-0.049	0.025	0.004
	6.82	$9/2^+$	0.001	0.000	0.000	0.031	0.010	0.004
$1/2^+$ [220]	4.35	$1/2^+$	-0.465	0.000	-0.195	0.853	0.000	0.000
	6.51	$3/2^+$	-0.089	0.454	0.113	0.233	-0.016	0.000
	5.25	$5/2^+$	0.289	-0.439	0.045	-0.524	0.001	0.060
	10.29	$7/2^+$	-0.008	0.000	-0.090	-0.086	0.010	0.009
	7.84	$9/2^+$	0.025	0.000	0.000	0.292	-0.004	-0.037

Table VI. (continued)

Nilsson Orbit	Energy E (MeV)	Spin and Parity I^π	A_{lj} for $0^+ \otimes I^\pi$	A_{lj} for $2^+ \otimes J^\pi$				
				$1/2^{+(-)}$ [a]	$3/2^{+(-)}$ [a]	$5/2^+$	$7/2^+$	$9/2^+$
$5/2^+$ [202]	5.80	$5/2^+$	0.206	-0.144	-0.016	0.048	-0.005	0.026
	7.11	$7/2^+$	-0.000	0.000	0.043	-0.091	-0.006	0.007
	9.34	$9/2^+$	0.014	0.000	0.000	0.132	-0.000	-0.012
$1/2^+$ [200]	6.31	$1/2^+$	-0.080	0.000	0.118	-0.020	0.000	0.000
	6.76	$3/2^+$	0.051	0.030	-0.065	-0.053	0.010	0.000
	7.93	$5/2^+$	0.003	-0.030	-0.057	0.006	0.004	-0.000
	8.94	$7/2^+$	-0.002	0.000	-0.030	-0.036	0.002	0.003
	11.09	$9/2^+$	0.001	0.000	0.000	0.005	-0.003	-0.000
$1/2^-$ [101]	2.77	$1/2^-$	0.938	0.000	0.347	0.000	0.000	0.000
	3.65	$3/2^-$	0.246	-0.938	-0.246	0.000	0.000	0.000
	3.98	$5/2^-$	0.000	0.938	-0.131	0.000	0.000	0.000
	6.04	$7/2^-$	0.000	0.000	0.279	0.000	0.000	0.000

[a] The negative parity for $1/2^-$ [101] band.

Chapter V

DISCUSSION AND CONCLUSIONS

A. The CCBA Analysis

In Chapter III the coupled-channel Born approximation, which includes inelastic processes in direct reactions, was shown to be necessary for a reasonable description of the (d, ^{3}He) and (d,t) reactions on ^{24}Mg. As seen in figs. 12-15, the overall agreement between the fits and experimental angular distributions for thirteen states in ^{23}Na and analogs in ^{23}Mg is quite good. This section will discuss the sensitivity of the angular distribution predictions of the spectroscopic amplitudes and show that some fits may be improved by using amplitudes differing from those of the Nilsson model. Some of the assumptions of this CCBA analysis will also be mentioned.

As remarked in Chapter III, the large indirect amplitudes predicted from Nilsson model calculations for the ground-state transitions enhance the isotropic contributions so that the forward peaking of the angular distributions are not described well. To investigate the effect of different relative amounts of direct and indirect scattering upon the shapes of these cross sections, the amplitude of the direct term was increased by a factor of three while holding

the inelastic terms constant. The results represented by the solid curves in fig. 18(a) give a considerably improved description of the data for transitions to both ^{23}Na and ^{23}Mg. This improvement indicates that the wavefunction used in the calculation of the spectroscopic amplitude was probably incorrect.

It is interesting that the angular distributions shown in fig. 18(a) may be altered at forward angles without significantly changing the structure at back angles. Since the direct and indirect terms add coherently, it is not generally possible to separate the contributions of each term to the final cross section. However, if either term is considerably smaller than the other, it is reasonable to neglect that term and to attribute the structure to a larger term. Tripling the amplitude of the direct term of the ground-state transition allowed this term to dominate the weaker indirect contributions at forward angles thereby giving the cross section the shape of the DWBA calculation in this region. However, the direct cross section decreases sharply at back angles (see fig. 11) so that the inelastic effects dominate and therefore produce a more isotropic shape for the angular distribution.

After observing that the relative magnitudes of the direct and indirect spectroscopic amplitudes have significant effects on the shapes of angular distributions, calculations were performed to determine the influence of different form factors in inelastic processes. If DWBA were to serve as a guide, one would expect little difference between transfers with the same orbital angular momentum $\vec{\ell}$ even though the total angular momentum transfers $\vec{j}$($= \vec{\ell} + \vec{s}$) were different. However, as seen in fig. 18(b), the predictions are quite sensitive to the $\vec{j}$ of the nucleon transferred. The solid and dotted curves show the

Figure 18. Comparisons of CCBA calculations for different spectroscopic amplitudes. Part (a) shows that the prediction for the ground-state transitions may be improved by increasing the spectroscopic amplitude of the direct coupling term by a factor of 3 (solid line). The unmodified fits of fig. 12 are reproduced here for comparisons (broken line). Part (b) shows the sensitivity of a $J^{\pi} = {}^{1}/_{2}^{+}$ angular distribution to the form factor assumed for the indirect coupling terms. For all cases illustrated the form factor may be expressed as $ad_{3/2} + bd_{5/2}$ where $a^2 + b^2$ is constant. The unmodified fit of fig. 13 is reproduced here (broken line).

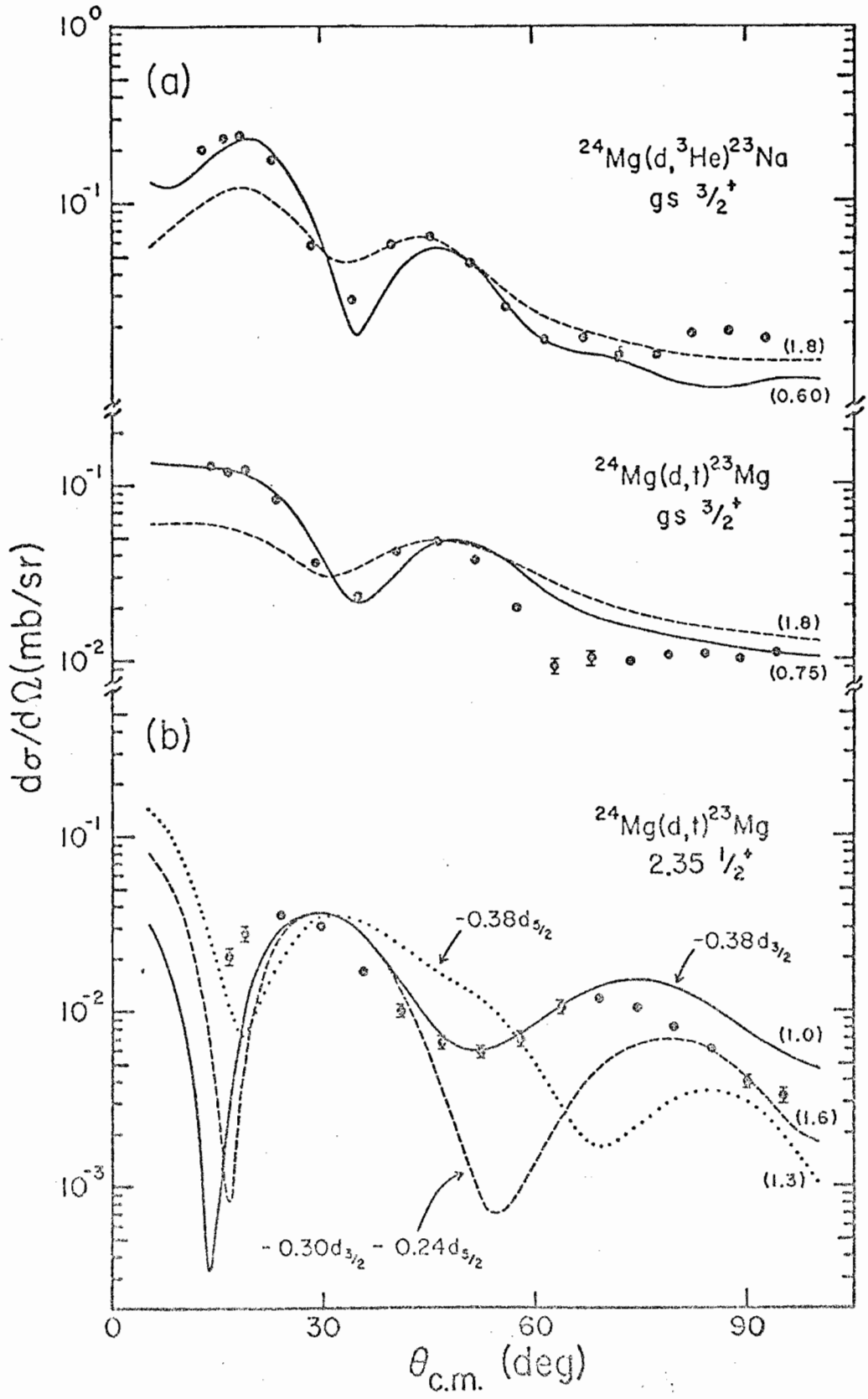
(a)
^{24}Mg(d,^{3}He)^{23}Na
gs 3/2^{+}
(1.8)
(0.60)
^{24}Mg(d,t)^{23}Mg
gs 3/2^{+}
(1.8)
(0.75)
(b)
^{24}Mg(d,t)^{23}Mg
2.35 1/2^{+}
-0.38d$_{5/2}$
-0.38d$_{3/2}$
(1.0)
(1.6)
(1.3)
-0.30d$_{3/2}$ - 0.24d$_{5/2}$
10^{0}
10^{-1}
10^{-2}
10^{-3}
dσ/dΩ(mb/sr)
0
30
60
90
θ$_{c.m.}$ (deg)

results for $1d_{3/2}$ and $1d_{5/2}$ transfers, respectively, from the 2^+ state of ^{24}Mg. The broken line is the distribution obtained using a mixture of both with amplitudes predicted by the Nilsson model. In each case the form factor may be expressed as the sum $ad_{3/2} + bd_{5/2}$ where $a^2 + b^2 = (0.38)^2$ so that the total $\ell = 2$ indirect amplitude is conserved. Indirect transfers with only the $d_{5/2}$ component give the best fit to the data.

One concludes from the two cases that some of the discrepancies between the CCBA predictions and experimental angular distributions may be explained by adjusting the spectroscopic amplitudes. A parametric study determined that the amplitude dependence on the single particle energies, E_o^{Ω}, and inverse moments of inertia A, (see Chapter IV) was small for most states. The occupation probability V_K^2 served mainly as a scaling factor for the amplitudes of states within a band. Consequently, reasonable changes in the free parameters for bandmixing (Table III) have minor effects upon the relative magnitudes of spectroscopic amplitudes for a state, and hence cannot predict the amplitudes which gave a best fit to the experimental data.

This analysis has not attempted to include the inelastic contributions through the 4^+ member of the ground-state rotational band and through the first 2^+ vibrational state of ^{24}Mg. Since the cross sections for inelastic scattering from these states are usually a factor of 5 smaller than those for the lowest 2^+ level, the cross sections for two-step reactions are expected to be smaller as well. The "forbidden" $^7/_2^+$ and $^9/_2^+$ states which are essentially populated through only inelastic processes would show the most sensitivity to these possible transitions.

This analysis has made other simplifying assumptions since additional complexities did not appear warranted in view of the success of the present treatment. The optical model potentials include no spin-orbit term. In a study of the (d,p) stripping reaction on ^{24}Mg, Mackintosh (1971) reported that inclusion of the spin-orbit terms in the entrance and exit channels changed the normalizations of the cross sections for the allowed transitions by only 20%. For the "forbidden" transitions this term damped the oscillatory behavior of the distribution and increased the magnitude of the prediction less than a factor of two.

Possible effects from compound nucleus formation are assumed to be small since the excitation energy in the compound system, 32.5 MeV, is so great. The success of the optical model for the description of the elastic and inelastic scattering (fig. 7) seems to confirm this assumption. Unfortunately, no deuteron excitation functions have been measured for ^{24}Mg at this energy to lend additional confirmation.

B. The Nuclear Structure of ^{23}Na and ^{23}Mg

The spectroscopic factors as listed in Table II were derived in what may be described as an iterative procedure. Using spectroscopic amplitudes determined from the Nilsson model with bandmixing, CCBA calculations gave a theoretical angular distribution to compare with the data. These initial fits were generally quite good as evidenced by the reasonable agreement between theory and experiment as shown in figs. 12-15. Very few of the predictions

required more than a factor of two in order to normalize the prediction to the experimental data. The spectroscopic factor was calculated as the product of the Nilsson model estimate for direct coupling and the additional normalization factor. As seen in Table II, the values obtained by this procedure are in general agreement with those determined from different reactions measured at higher energies and analyzed with DWBA.

The application of the sum rules with the experimental spectroscopic factors taken from columns 4 and 5 of Table II shows that for positive parity states, $\Sigma C^2S = 3.0$ for ^{23}Na and ^{23}Mg where the shell-model limit is $\Sigma C^2S = 4$. The remaining strength may be in the unobserved $T = {}^3/_2$ levels. The fact that the spectroscopic strength of the ground-state band, $\Sigma C^2S = 2.6$ (2.5), exceeds the limit of 2 for a single Nilsson orbit implies that bandmixing is necessary in the model for ^{23}Na and ^{23}Mg. From Table II one sees that the mixing transfers much of the strength of the ${}^1/_2{}^+[220]$ band into the ground-state band. The negative parity strength, $\Sigma C^2S = 2.0$ (2.7), for the ${}^1/_2{}^-[101]$ orbit in ^{23}Na (^{23}Mg) indicates that most of the total p-shell strength (limit $\Sigma C^2S = 6$) is associated with high excitation energies. Since this strength also exceeds the limit of 2, it emphasizes that bandmixing is required.

Only the predictions for the ${}^1/_2{}^+[220]$ band (fig. 14) with states above 4 MeV gave poor agreement with experiment. With the exception of the 4.36-MeV level in ^{23}Mg (see fig. 14), the shapes of the angular distributions for members of the band were fairly well described, but the magnitudes were a factor of $\sim$10 too large. In view of the success of fits for each of the other three bands, this failure is quite puzzling. As may be seen in Table VI the

coupling of this band with the 2^+ state of ^{24}Mg is large so that the indirect contributions are quite strong. A calculation for the $^5/_2^+$ member of this band in ^{23}Na revealed that if only the direct coupling is included, then the cross section is reduced a factor of 5 at forward angles giving much better agreement with the magnitude of the data. However, the shape of the resulting distribution exhibits a more pronounced diffraction pattern that is unobserved in the data. A similar calculation for the $^1/_2^+$ member of this band in ^{23}Mg also exhibited a decrease in the magnitude of the prediction and a stronger diffraction pattern. In this case both effects gave better agreement with the data. Thus it may be possible to choose the amplitude of the indirect coupling at some value between those used here, and obtain improved overall fits to members of this band and also predict the correct magnitude.

The general consistency of the spectroscopic factors listed in Table II suggested an investigation of the high energy limit of the CCBA analysis. Calculations were performed for several angular distributions from the ^{24}Mg (d, ^{3}He) ^{23}Na reaction at 52 MeV (Krämer et al., 1971) using appropriately modified optical model parameters similar to those given by Krämer and the deformation parameter measured in this study. The CCBA predictions were essentially identical whether or not the indirect terms were included, and furthermore, they agreed with the DWBA fit obtained by Krämer. At higher energies the CCBA analysis appears equivalent to the usual DWBA treatment.

C. Conclusions

The calculations of this present study imply that the experimental angular distributions for the $^{24}Mg(d,{}^{3}He)^{23}Na$ and $^{24}Mg(d,{}^{3}He)^{23}Mg$ reactions are generally consistant with a Nilsson strong-coupling model for ^{23}Na and ^{23}Mg if bandmixing is included. This conclusion is critically dependent on the inclusion of inelastic effects without which agreement with the data is not possible. The only notable conflicts between the collective model predictions and experimental results are the magnitudes of spectroscopic factors calculated for the transitions to the ground-state and to the members of the $^{1}/_{2}^{+}$ [220] band.

Recently McGrory and Wildenthal (1971) have obtained wavefunctions for ^{23}Na and ^{24}Mg from a truncated shell model calculation. It would be most interesting to apply these wavefunctions in the CCBA description for these reactions.

APPENDIXES

Appendix A

DESCRIPTION OF DATA ACQUISITION PROGRAMS

A. General

Many nuclear studies require particle identification. In favorable cases, the kinematics of the reaction alone may accomplish this identification, but frequently counter telescopes must be employed. This device consists of two detectors, one in which a particle deposits an energy ΔE, and the other which stops the particle collecting the remainder of the energy E. Given these ΔE and E pulses, the most common method for identification employs the fact that the range of the particle with charge Z, mass M and total energy $E_T = E + \Delta E$ is well represented by

$$R(M, Z, E_T) = \frac{M}{Z^2} R_p (E_T/M) \tag{A1}$$

where $R_p (E_p)$ is the range of a proton of energy E_p. Over a wide energy region, the proton range is given by

$$R_p (E_p) = c E_p^n \tag{A2}$$

where c and n are constants. Using (A1) and (A2) the thickness, T, of the ΔE

detector can be written as

$$T = R(E + \Delta E) - R(E)$$

$$= \frac{cM}{Z^2} \left[\left(\frac{E + \Delta E}{M} \right)^n - \left(\frac{E}{M} \right)^n \right]$$

$$= c \, (Z^2 \, M^{n-1})^{-1} \left[(E + \Delta E)^n - E^n \right]$$

so that

$$(E + \Delta E)^n - E^n = c^{-1} \, Z^2 \, M^{n-1} \, T \qquad \text{(A3)}$$

Goulding et al. (1964) were the first to develop and use this method for particle identification.

B. PART8 and MFBCT

Equation (A3) forms the basis for the computer code PART8 which was developed for on-line particle identification. The main program, written in FORTRAN IV, features input control from a typewriter, light pen and sense switches and output links through a typewriter, oscilloscope display and magnetic tape. Input from the analog to digital converters (ADC's) through the fully buffered channel (FBC), particle identification and buffered tape storage are controlled by DAP subprogram MFBCT, available in the TUNL Systems Library.

As shown in fig. A1 , the subprogram MFBCT has five no-priority routines and one interrupt section to execute different controls. A call to MFBCT prepares the interrupt section for data processing and storage, and sets up the

Figure A1. Flow diagram for the data acquisition subroutine MFBCT. The data analysis portion of the interrupt section is expanded in fig. A2.

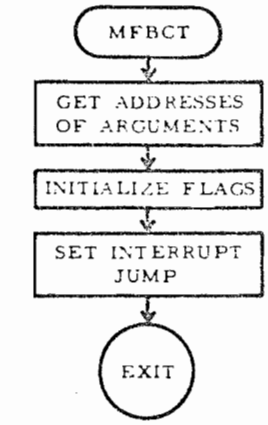
MFBCT
GET ADDRESSES OF ARGUMENTS
INITIALIZE FLAGS
SET INTERRUPT JUMP
EXIT

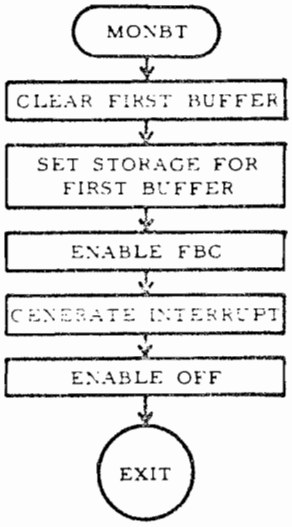
MONBT
CLEAR FIRST BUFFER
SET STORAGE FOR FIRST BUFFER
ENABLE FBC
GENERATE INTERRUPT
ENABLE OFF
EXIT

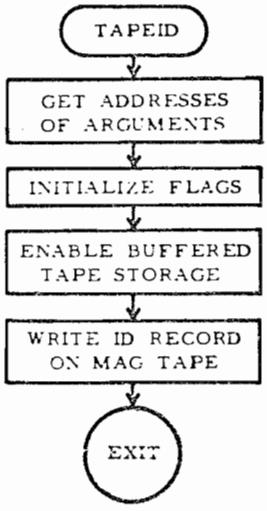
TAPEID
GET ADDRESSES OF ARGUMENTS
INITIALIZE FLAGS
ENABLE BUFFERED TAPE STORAGE
WRITE ID RECORD ON MAG TAPE
EXIT

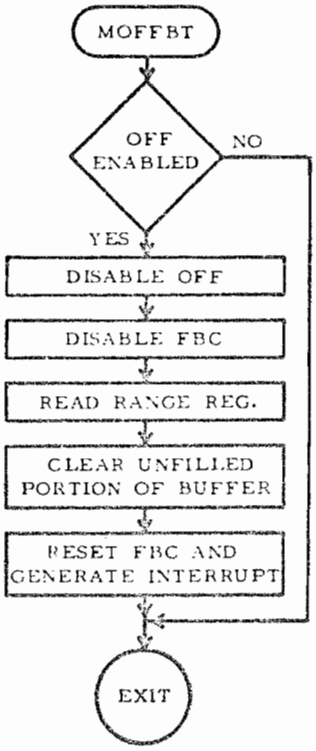
MOFFBT
OFF ENABLED
NO
YES
DISABLE OFF
DISABLE FBC
READ RANGE REG.
CLEAR UNFILLED PORTION OF BUFFER
RESET FBC AND GENERATE INTERRUPT
EXIT

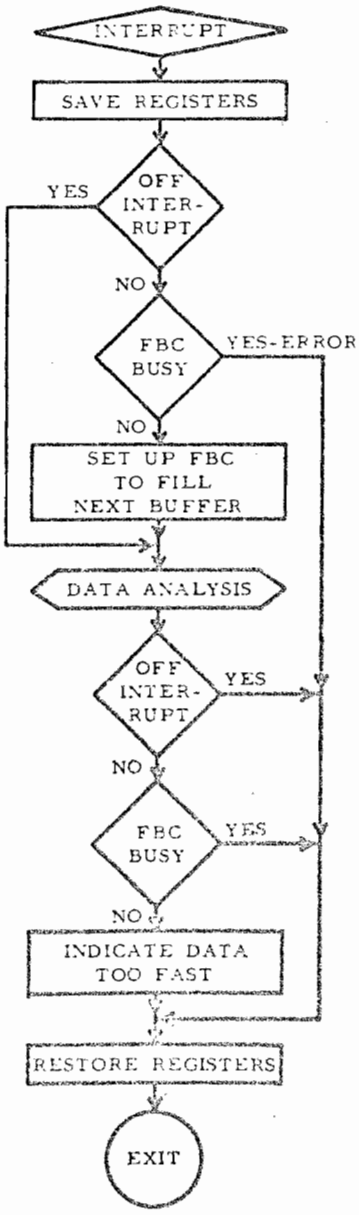
INTERRUPT
SAVE REGISTERS
YES
OFF INTER-RUPT
NO
FBC BUSY
YES-ERROR
NO
SET UP FBC TO FILL NEXT BUFFER
DATA ANALYSIS
OFF INTER-RUPT
YES
NO
FBC BUSY
YES
NO
INDICATE DATA TOO FAST
RESTORE REGISTERS
EXIT

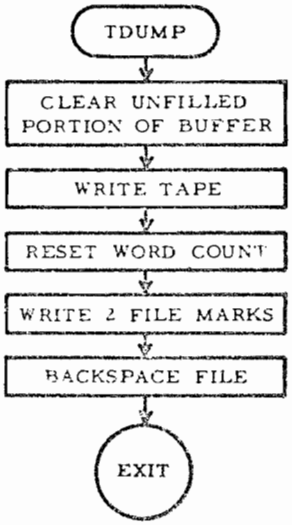
TDUMP
CLEAR UNFILLED PORTION OF BUFFER
WRITE TAPE
RESET WORD COUNT
WRITE 2 FILE MARKS
BACKSPACE FILE
EXIT

FBC interrupt jump. To start data collection one calls MONBT which sets an indicator for data storage in the first buffer, clears the buffer, enables the FBC and generates an interrupt. Note that when taking data with the FBC two storage blocks are employed, one buffer in which the FBC stores data while events in the other are analyzed.

A call to MOFFBT discontinues data taking by disabling input to the FBC. Then the FBC range register is input to the computer, and the remaining unfilled portion of the buffer is cleared. After the FBC is reset, an interrupt is generated to initiate data analysis. Note that a call to MOFFBT will be ignored unless MONBT was called last.

Interrupts are generated by the FBC when it has processed enough events to completely fill a buffer or when a call to MONBT or MOFFBT has been executed. When the computer acknowledges the interrupt, program control is transferred to the interrupt section of MFBCT where first the contents of the computer registers are saved. If the FBC or MONBT generated the interrupt, then the FBC is set up for storage in the next buffer. Flags are reset indicating which block is receiving data, and the analysis begins. When processing interrupts from MOFFBT the FBC setup is bypassed. In the analysis section which is discussed in some detail in the next section, the zeroes inserted in the data buffer by MONBT and MOFFBT are considered bad events and ignored. Unless processing a MOFFBT interrupt, a check is made after analysis to see if storage in the next buffer is complete, i.e. if the FBC is not busy. The data rate is too fast if the FBC is found not busy, and a warning flag is set indicating the condition. Finally, the computer registers are restored to their values at interrupt

time, and program control is returned to the interrupted routine.

If the data events are to be written on magnetic tape, then TAPEID must be called to enable buffered storage and write an identification record on the tape. When a buffered data run is terminated, TDUMP is called to clear the unfilled portion of the last buffer and then write it on tape followed by a file mark. After TDUMP has been called, a tape identification record must be written before buffered storage is reenabled.

C. Data Analysis in MFBCT

The data analysis routine in MFBCT, shown as a flow diagram in fig. A2, consists primarily of an evaluation of an expression like eq. (A3) followed by storage in a mass, energy versus mass or particle energy spectrum. For each event the routing bits and the numbers representing ΔE and $E + \Delta E$ are extracted from the 24 bit data word. Then the full-energy $E + \Delta E$ is corrected for the effect of the biased amplifier, and E is calculated as the difference $(E + \Delta E) - \Delta E$. Having obtained values for $E + \Delta E$ and E, the expression

$$M = (E + \Delta E)^n - E^n \qquad (A4)$$

is evaluated.

Following the work of D. D. Armstrong et al. (1969) a table look-up procedure was used to evaluate eq. (A4) since direct computation would have been too slow. After shifting off four bits from $E + \Delta E$ and E, the integer parts were used to address an entry in the range table, and the fractional parts were

Figure A2. Flow diagram for on-line particle identification. The operations and logic of the data analysis section of MFBCT are shown in detail.

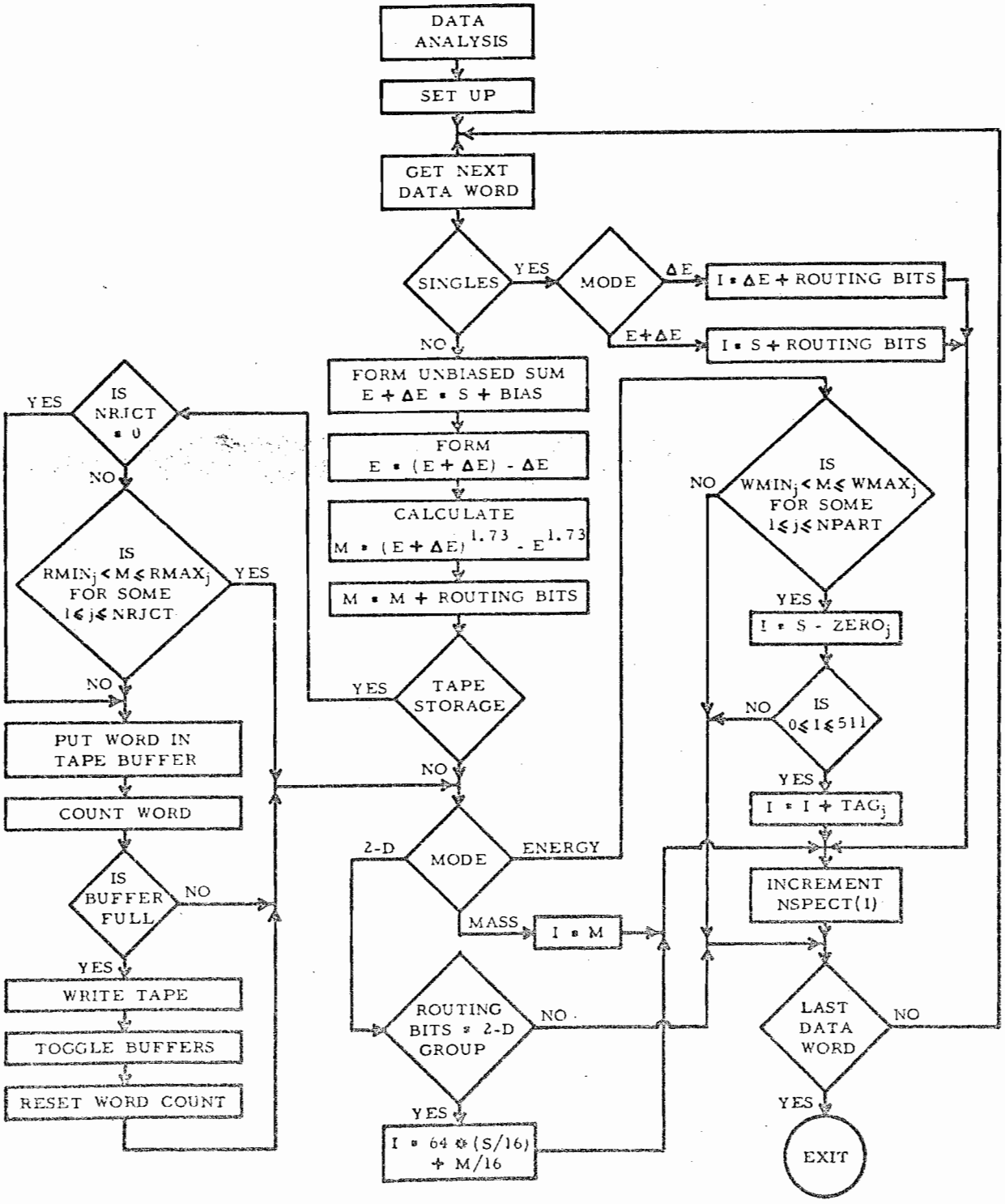
DATA ANALYSIS
SET UP
GET NEXT DATA WORD
SINGLES
YES
MODE
ΔE
I = ΔE + ROUTING BITS
E+ΔE
I = S + ROUTING BITS
NO
FORM UNBIASED SUM E + ΔE = S + BIAS
FORM E = (E + ΔE) - ΔE
CALCULATE M = (E + ΔE)^1.73 - E^1.73
M = M + ROUTING BITS
TAPE STORAGE
YES
NO
IS NRJCT = 0
YES
NO
IS RMIN_j < M ≤ RMAX_j FOR SOME 1 ≤ j ≤ NRJCT
YES
NO
PUT WORD IN TAPE BUFFER
COUNT WORD
IS BUFFER FULL
NO
YES
WRITE TAPE
TOGGLE BUFFERS
RESET WORD COUNT
MODE
2-D
ENERGY
MASS
I = M
ROUTING BITS = 2-D GROUP
NO
YES
I = 64 * (S/16) + M/16
IS WMIN_j < M ≤ WMAX_j FOR SOME 1 ≤ j ≤ NPART
NO
YES
I = S - ZERO_j
IS 0 ≤ I ≤ 511
NO
YES
I = I + TAG_j
INCREMENT NSPECT(I)
LAST DATA WORD
NO
YES
EXIT

used to linearly interpolate between that entry and the next. A variable number of bits determined by typewriter command is then shifted off the difference, thus forming M. The range table is initially calculated using n = 1.73, but this value may also be modified by typewriter input. Note that the evaluation of M is not dependent on any functional relation between range and energy. For example, empirical range data would work as well or better for particles with low energies where the range deviates greatly from the E^n behavior.

The mass parameter M is next modified by the addition of routing bits. Since the present form of MFBCT allows for as many as four telescopes, four 1024 channel mass spectra may be obtained. If the program is in the mass mode, the value M determines the channel number to be incremented. In the energy versus mass (2-D) mode, the number I, where $I = 64 \times \left[(E + \Delta E)/16\right] + M/16$ with M values corresponding to a selected telescope, determines the channel number to be incremented. In the particle energy mode, the value M is compared with particle windows to determine which particle energy spectrum is to be incremented. There may be as many as eight particle energy spectra with their corresponding windows selected from any mass spectrum and specified by use of the light pen or typewriter. Each spectra may have a different zero offset defined by typewriter command. Once the particle group has been determined, the corresponding zero offset is subtracted from $E + \Delta E$ and the resulting number determines the channel number to be incremented within the particle energy spectrum. However, if the number is negative or greater than 511, the event is ignored.

Two other data storage modes are available for single storage of ΔE or $E + \Delta E$ spectra for each telescope. These modes cannot perform mass identification or buffered tape storage and are most frequently used in setting up the electronic apparatus.

When storing data on magnetic tape, as many as eight particle windows may be selected to exclude from buffered storage those events associated with the particle windows. This feature may be employed to suppress high cross section elastic events if one is only interested in reactions. This has the advantage of reducing the amount of tape required to buffer the data. Like the mass windows for particle energy storage, the rejection windows can be selected from any mass spectrum. If it is desired to buffer all events, the number of rejection groups is specified to be zero.

The buffered tape section of MFBCT examines the calculated mass for each event and determines if it lies outside all rejection windows. If it does, it is entered in the tape storage buffer and counted. When this buffer is full, the word count is reset and storage is started in a second buffer while the first is written on magnetic tape. The dual buffer technique used here is identical with that of the FBC storage.

A version of this particle identification routine called MFBC which has no provisions for buffered tape storage is also available in the TUNL System Library.

Appendix B

THE COUPLED-CHANNEL CALCULATIONS

A. Introduction

The distorted wave Born approximation (DWBA) has been applied to the description of transmutation reactions induced by projectiles of low and medium energy. In cases where the interaction which causes these transitions is relatively weak, the first order DWBA is a reasonable approximation. However, for collective nuclei the inelastic processes frequently are stronger than the interaction for transmutations. In such cases, a higher order DWBA or coupled-channel calculation is necessary. Only the latter will be considered in this discussion.

B. The Coupled-Channel Born Approximation

The following derivation of the coupled-channel Born approximation (CCBA) is based on discussions with W. J. Thompson (1971).

To describe the stripping reaction A(a,b)B where a = b + x and B = A + x, it is assumed that the internal states of b and x are unchanged by

their interactions and that particle a is not excited by its inelastic scattering.

Since the final-state-interaction formulation of stripping is used here, the total Hamiltonian is first written for the bB system. The Schrödinger equation to be solved is given by

$$(H_B + T_{bB} + V_{bB} - E)|\Psi\rangle = 0 \tag{B1}$$

where H_B is the Hamiltonian for the internal structure of B and T_{bB} and V_{bB} are the kinetic energy and potential energy operators, respectively, for the bB system. We introduce the interaction potential U_{bB}, which will be used as a generalized optical model potential describing elastic and inelastic scattering of b from B. From eq. (B1) we write

$$(H_B + T_{bB} + U_{bB} - E)|\Psi\rangle = -(V_{bB} - U_{bB})|\Psi\rangle \tag{B2}$$

Similarly we introduce the generalized optical model potential for the aA system, U_{aA}, and we define the wavefunction describing the elastic and inelastic scattering of a from A, $|\Psi^{\circ}_{aA}\rangle$, by the expression

$$(H_A + T_{aA} + U_{aA} - E)|\Psi^{\circ}_{aA}\rangle = 0 \tag{B3}$$

where H_A and T_{aA} are analogous to H_B and T_{bB}. This wavefunction may be expanded as

$$|\Psi^{\circ}_{aA}\rangle = \phi_a \sum_i |i\rangle \phi^{\circ}_i \tag{B4}$$

where ϕ_a and ϕ°_i denote the wavefunction for the ground-state of a and the wavefunction for the relative motion, respectively. The internal wavefunction of A, represented by $|i\rangle$, must satisfy

$$H_A|i\rangle = E^*_i|i\rangle \tag{B5}$$

where E^*_i is the excitation energy of A. Equation (B3) requires that ϕ°_i satisfy

the coupled-channel equations

$$(T_{aA} - E_i)\phi_i^\circ + \sum_{i'} \langle i | U_{aA} | i' \rangle \phi_{i'}^\circ = 0 \tag{B6}$$

where $E_i = E - E_i^*$ is the kinetic energy of a_i for the inelastic scattering $A(a, a_i')A_i^*$.

In most cases the aA system gives rise to mainly elastic and inelastic scattering in a few channels. Therefore we make the Born approximation

$$|\psi\rangle \simeq |\psi_{aA}^\circ\rangle \tag{B7}$$

so that eq. (B2) may be written

$$(H_B + T_{bB} + U_{bB} - E)|\psi\rangle = -(V_{bB} - U_{bB})|\psi_{aA}^\circ\rangle \tag{B8}$$

We now expand the total wavefunction $|\psi\rangle$ as

$$|\psi\rangle = \phi_b \phi_x \sum_{f'} |f'\rangle \phi_{f'} \tag{B9}$$

where ϕ_b and ϕ_x denote the ground-states of b and x. In analogy with the expressions above, $|f\rangle$ and ϕ_f represent the internal wavefunction for B and the relative motion, respectively. Using (B9) in (B7) we find the latter must satisfy

$$\begin{aligned}(T_{bB} - E_f)\phi_f + \sum_{f'} \langle f | U_{bB} | f' \rangle \phi_{f'} \\ = -\sum_i \langle \phi_b \phi_x f | V_{bB} - U_{bB} | i \phi_a \phi_i^\circ \rangle\end{aligned} \tag{B10}$$

In the CCBA treatment we make the additional assumption that $V_{bB} \approx U_{Bb}$ so that

$$(T_{bB} - E_f)\phi_f^\circ + \sum_{f'} \langle f | U_{bB} | f' \rangle \phi_{f'}^\circ = 0 \tag{B11}$$

We have added the superscript to the ϕ_f° to indicate that it is a solution to the homogeneous equation. Equation (B2) becomes

$$(H_B + T_{bB} + U_{bB} - E)|\psi_{bB}^\circ\rangle = 0 \tag{B12}$$

where $|\psi_{bB}^\circ\rangle = |\psi\rangle$

The transition amplitude from the aA system to the f^{th} final state of B is (Wu and Ohmura, 1962)

$$T_f = \langle f\, \psi_{bB}^\circ | (V_{bB} - U_{bB}) | \psi \rangle \tag{B13}$$

so that for the CCBA

$$\begin{aligned} T_f &\simeq \sum_i \langle \phi_f^\circ\, \phi_b\, \phi_x f | V_{bx} | i\, \phi_a\, \phi_i^\circ \rangle \\ &= \sum_i \int \phi_f^{\circ *} \langle f | i \rangle \langle \phi_b\, \phi_x | V_{bx} | \phi_a \rangle \phi_i^\circ \, d\vec{r}_{Ax}\, d\vec{r}_{bx} \end{aligned} \tag{B14}$$

In the zero range approximation we assume

$$\langle \phi_b\, \phi_x | V_{bx} | \phi_a \rangle = N_0\, \delta(\vec{r}_{bx}) \tag{B15}$$

so that eq. (B14) becomes

$$T_f = N_0 \sum_i \int \phi_f^{\circ *}\left(\frac{m_A}{m_B}\vec{r}_{Ax}\right) \langle f | i \rangle\, \phi_i^\circ(\vec{r}_{Ax})\, d\vec{r}_{Ax} \tag{B16}$$

The constant N_o may be expressed as

$$N_o = \frac{D_o \nu c^2}{2s+1}$$

where c is an isospin coupling coefficient, s is the spin of particle x, ν is the number of nucleons in particle a and D_o is a unique constant for each reaction.

In terms of the transition amplitude the cross section for an unpolarized system is

$$\left(\frac{d\sigma}{d\Omega}\right)_{ab} = \frac{m_{Aa}\, m_{Bb}}{(2\pi\hbar)^2} \frac{K_{Bb}}{K_{Aa}} \frac{1}{(2J_A+1)(2S_a+1)} \sum |T_f|^2 \qquad \text{(B17)}$$

where m_{ij} and K_{ij} are the reduced mass and wave number, respectively, for the appropriate channel. All possible transition amplitudes are summed and then averaged over the initial states.

The scattering wavefunctions ϕ_i^o and ϕ_f^o are solutionsto coupled-channel equations as represented by eq. (B6). These will be discussed in the next section. For the present we wish to consider the overlap $\langle f \mid i \rangle$. One usually expands $|f\rangle$ in terms of states of good angular momentum as

$$|f\rangle = \sum_{lj} A_{lj} \left(|i\rangle \otimes \phi_{lj} \right)_f$$

where ϕ_{lj} is the single particle wavefunction for x bound to A and $\otimes$ denotes the angular momentum coupling. The overlap may then be expanded in terms of ϕ_{lj} (see Chapter IV).

C. The Coupled-Channel Optical Model

The discussion of the last section developed formal solutions for wavefunctions for the generalized optical model potentials, U, not well suited to practical calculations. In this section we introduce the emphirical potential usually employed in optical model studies, and calculate wavefunctions as expansions in terms of good angular momentum. The discussion follows the work of T. Tamura (1965).

For collective nuclei the interaction potential for an incident particle can be described by a potential $U(r, \theta, \phi)$ which is, in general, non-spherical. It is assumed that

$$U(r,\theta,\phi) = V_{Coul} - V(1+e^{x})^{-1} - iW(1+e^{x'})^{-1} - 4iW_D e^{x'}(1+e^{x'})^{-2} - V_{so}\, 2\vec{l}\cdot\vec{s}\, e^{x''}(1+e^{x''})^{-2}/a_{so}r \quad \text{(B18)}$$

where

$$x = (r - r_r A^{1/3})/a_r, \quad x' = (r - r_i A^{1/3})/a_i, \quad x'' = (r - r_{so} A^{1/3})/a_{so} \quad \text{(B19)}$$

and V_{Coul} is the Coulomb potential. The angular dependence of U is determined by the collective nature of the target. For nuclei which vibrate about a spherical shape, r_r and r_i are written as

$$r_r = \bar{r}_r f^{V}(\theta,\phi) \qquad r_i = \bar{r}_i f^{V}(\theta,\phi) \quad \text{(B20)}$$

where

$$f^{v}(\theta,\phi) = 1 + \sum_{\lambda\mu} \alpha_{\lambda\mu} Y_{\lambda\mu}(\theta,\phi) \tag{B21}$$

If the nucleus is an axially symmetric deformed nucleus, $f^{v}(\theta,\phi)$ is replaced with $f^{r}(\theta)$ where

$$f^{r}(\theta) = 1 + \sum_{\lambda} \beta_{\lambda} Y_{\lambda 0}(\theta') \tag{B22}$$

Here θ' refers to the body-fixed system.

For a vibrational nucleus $U(r,\theta,\phi)$ is expressed as a power series expansion to second order in $\Sigma_{\lambda\mu} \alpha_{\lambda\mu} Y_{\lambda\mu}$, and for deformed nuclei, $U(r,\theta,\phi)$ is expressed as a Legendre polynomial expansion. Then writing

$$U(r,\theta,\phi) = V_{diag} + V_{coupl} \tag{B23}$$

the potential V_{diag} is approximately the usual optical potential for spherical nuclei, and is diagonal with respect to channels with total angular momentum, $\vec{J}$, where $\vec{J} = \vec{j}_n + \vec{I}_n$. Here the n^{th} state of the target with angular momentum, $\vec{I}_n$, is coupled to a partial wave with total angular momentum $\vec{j}_n (= \vec{l}_n + \vec{s}_n)$. In contrast to V_{diag} the potential V_{coupl} gives coupling between channels with the same $\vec{J}$, but with different $\vec{j}_n$ and $\vec{I}_n$. Both V_{diag} and V_{coupl} contain terms obtained from the power series expansion of the Coulomb potential with $R_c(\theta,\phi) = \bar{R}_c f^{v}(\theta,\phi)$.

The Hamiltonian for the relative system may be written as

$$H = T + H_t + U(r,\theta,\phi) = T + H_t + V_{diag} + V_{coupl} \tag{B24}$$

where T is the kinetic energy of the incident particle and H_t is the Hamiltonian

for the internal motion of the target nucleus. The Schrödinger equation is given by

$$H\psi = E_l \psi \tag{B25}$$

where E_l is the center of mass energy of the incident particle. The total wavefunction ψ may be expanded as

$$\psi = r^{-1} \sum_{J_n l_n j_n} R_{J_n l_n j_n}(r) \left(\mathcal{Y}_{l_n j_n} \otimes \Phi_{I_n} \right)_{JM} \tag{B26}$$

$$= r^{-1} \sum_{J_n l_n j_n} R_{J_n l_n j_n}(r) \sum_{m_j M_n} (j_n I_n m_j M_n | JM) \mathcal{Y}^{m_j}_{l_n j_n} \Phi_{I_n M_n}$$

and

$$\mathcal{Y}^{m_j}_{l_n j_n} = \sum_{m_l m_s} (l_n s m_l m_s | j_n m_j) i^l Y^{m_l}_{l_n} \chi_{s m_s}$$

where (ABab | Cc) is a Clebsch-Gordan coefficient. In the above relations $\chi_{s m_s}$ is the spin wavefunction of the projectile and $\Phi_{I_n M_n}$ is the wavefunction of the target nucleus which satisfies

$$H_t \Phi_{I_n M_n} = \omega_n \Phi_{I_n M_n} \tag{B27}$$

Here ω_n is the energy of the n^{th} excited state and by energy conservation $E_n = E_l - \omega_n$.

Substituting eqs. (B24), (B26), and (B27) into (B25), multiplying it by $\left(\mathcal{Y}_{l_n j_n} \otimes \Phi_{I_n} \right)^*_{JM}$ from the left, integrating over the target internal coordinates and dividing by E_n, one obtains the following equation:

$$\left(\frac{d^2}{d\rho_n^2} - \frac{l_n(l_n+1)}{\rho_n^2} - \frac{1}{E_n} V_{diag} + 1\right) R_{J n l_n j_n}$$

$$= E_n^{-1} \sum_{n' l_n' j_n'} \langle (y_{l_n j_n} \otimes \Phi_{I_n})_{JM} | V_{coupl} | (y_{l_n' j_n'} \otimes \Phi_{I_n'})_{JM} \rangle R_{J n l_n' j_n'} \quad \text{(B28)}$$

where $\rho_n = k_n r$ (k_n is the wavenumber). Equation (B28) represents a set of n_c coupled equations for a particular value of J where n_c is the number of combinations of j_n, l_n and I_n such that $\vec{J} = \vec{j}_n + \vec{I}_n$ and $\vec{j}_n = \vec{l}_n + \vec{s}$.

The assumptions about the nuclear structure are contained in the matrix elements on the right hand side of eq. (B28), and the detailed evaluation of these matrix elements is given by Tamura (1965). It remains only to solve the coupled equation of (B28) and match it at an appropriate matching radius to its asymptotic solution.

Equation (B26) may alternately be written as a partial-wave expansion of the Coulomb-field wavefunctions. If no inelastic scattering were present, one obtains

$$\psi = \frac{4\pi}{k\Omega} \sum_{m_s M_I} a_{m_s} b_{M_I} \sum_{l m_l} Y^*_{l m}(\hat{k}) \sum_{j m_j J M} (l s m_l m_s | j_c m_j)$$

$$\times (j I_t m_j M_I | J M) e^{i\delta_l} f^J_{l_j}(kr) (y_{l_j} \otimes \Phi_{I_t M_I})_{JM} \quad \text{(B29)}$$

Here a_{ms} and b_{ml} describe the polarized states of the projectile and target, respectively. The function $f_{l_j}(kr)$ has the asymptotic form

$$\beta^{J}_{\ell j}(kr) \xrightarrow[r\to\infty]{} F_\ell(kr) + C^{J}_{\ell j} H_\ell(kr)$$
$$= F_\ell(kr) + C^{J}_{\ell j}\left[G_\ell(kr) + i F_\ell(kr)\right] \qquad \text{(B30)}$$

where F_ℓ and G_ℓ are the regular and irregular Coulomb wavefunctions, respectively. When inelastic scattering is present Ψ becomes

$$\Psi = \frac{4\pi}{kr}\sum_{m_s M_1} a_{m_s} b_{M_1} \sum_{\ell m_\ell} Y^{*}_{\ell m_\ell}(\hat{k}) \sum_{j m_j JM} (\ell s\, m_\ell\, m_s | j m)$$
$$\times (j I_1\, m_j\, M_1 | JM) \sum_{n\ell' j'} e^{i\delta^{n}_{\ell'}} g^{J}_{\ell j, n\ell' j'}(kr)\left(Y_{\ell' j'} \otimes \Phi_{I_n M_n}\right)_{JM} \qquad \text{(B31)}$$

where

$$g^{J}_{\ell j, n\ell' j'} \xrightarrow[r\to\infty]{} F_{\ell'}(kr)\,\delta_{n1}\,\delta_{\ell\ell'}\,\delta_{jj'} + C^{J}_{\ell j, n\ell' j'} H_{\ell'}(kr) \qquad \text{(B32)}$$

The coefficient $C_{\ell j, n\ell' j'}$ is the amplitude of an outgoing wave in the channel $(n\ell' j')$ due to an incoming wave in the channel $(1\ \ell\ j)$, and it may be determined by comparison of the solution of eq. (B26) with the asymptotic form of eq. (B31) at the matching radius. The differential cross sections for scattering leaving the target in its n^{th} state may be obtained from the scattered component of the wavefunction of eq. (B31).

LIST OF REFERENCES

M. Arditi, L. Bimbot, H. Doubre, N. Frascaria, J. P. Garron, M. Riou and D. Royer, Nucl. Phys. A165 (1971) 129.

D. D. Armstrong, J. G. Berry, E. R. Flynn, W. S. Hall, P. W. Keaton, Jr. and M. P. Kellogg, Nucl. Instr. and Meth. 70 (1969) 69.

R. J. Ascuitto and N. K. Glendenning, Phys. Rev. 181 (1969) 1396.

S. T. Belyaev, Det. Kgl. Danske Videnskab. Selskab, Mat. - Fys. Medd. 31 (1959) No. 11.

A. Bohr, Det. Kgl. Danske Videnskab. Selskab, Mat. - Fys. Medd. 26 (1952) No. 14.

A. Bohr and B. R. Mottleson, Det. Kgl. Danske Videnskab. Selskab, Mat. - Fys. Medd. 27 (1953) No. 16.

H. H. Bolotin, M. G. Strauss and D. A. McClure, Nucl. Instr. and Meth. 83 (1970) 1.

J. P. Davidson, Revs. Mod. Phys. 37 (1965) 105.

D. Dehnhard and J. L. Yntema, Phys. Rev. 160 (1967) 964.

R. J. de Meijer, H. F. J. van Royen and P. J. Brussaard, Nucl. Phys. A164 (1971) 11.

J. Dubois, Nucl. Phys. A104 (1967[a]) 657.

J. Dubois and L. G. Earwaker, Phys. Rev. 160 (1967[b]) 925.

J. Dubois, Nucl. Phys. A116 (1968) 489.

T. G. Dzubay and R. V. Poore, to be published in Phys. Rev.

J. R. Erskine, private communication (1970).

M. P. Fricke and G. R. Satchler, Phys. Rev. 139 (1965) B567.

M. Gaillard, R. Bouche, L. Feuvrais, P. Gaillard, A. Guichard, M. Gusakow, J. L. Leonhardt and J. R. Pizzi, Nucl. Phys. A119 (1968) 161.

F. S. Goulding, D. A. Landis, J. Cerny and R. H. Pehl, Nucl. Instr. and Meth. 31 (1964) 1.

L. C. Haun, unpublished Ph.D. thesis, Duke University, 1968.

L. C. Haun, N. R. Roberson and D. R. Tilley, Nucl. Phys. A140 (1970) 333.

A. J. Howard, J. P. Allen and D. A. Bromley, Phys. Rev. 139 (1965) B1135.

J. M. Joyce, R. W. Zurmühle and C. M. Fou, Nucl. Phys. A132 (1969) 629.

J. M. Joyce, W. S. McEver, R. O. Nelson, R. V. Poore and N. R. Roberson, Bull. Am. Phys. Soc. 15 (1970) 598.

I. Kanestrøm, Phys. Lett. 35B (1971) 283.

A. K. Kerman, Det. Kgl. Danske Videnskab. Selskab, Mat. - Fys. Medd 30 (1956) No. 15.

R. L. Kozub, Phys. Rev. 172 (1968) 1078.

E. Krämer, G. Mairle and G. Kaschl, Nucl. Phys. A165 (1971) 353.

P. D. Kunz, private communication (1970).

A. E. Litherland, E. B. Paul, G. A. Bartholomew and H. E. Gove, Phys. Rev. 102 (1956) 208.

R. S. Mackintosh, Nucl. Phys. A170 (1971) 353.

W. S. McEver, unpublished Ph.D. thesis, University of North Carolina at Chapel Hill, 1970.

J. B. McGrory and B. H. Wildenthal, Phys. Lett. 34B (1971) 373.

S. G. Nilsson, Det. Kgl. Danske Videnskab. Selskab, Mat. - Fys. Medd. 29 (1955) No. 16.

P. L. Ottaviani and L. Zuffi, Nucl. Phys. A151 (1970) 198.

S. K. Penny and G. R. Satchler, Nucl. Phys. 53 (1964) 145.

A. R. Poletti, A. D. W. Jones, J. A. Becker, R. E. McDonald and R. W. Nightingale, Phys. Rev. 184 (1969) 1130.

A. R. Poletti, J. A. Becker and R. E. McDonald, Phys. Rev. C2 (1970) 964.

J. R. Powers, H. T. Fortune, R. Middleton and Ole Hansen, Phys. Rev. C4 (1971) 2030.

M. A. Preston, Physics of the Nucleus (Addison-Wesley Publishing Co., Inc., Reading, Mass., 1962).

F. O. Purser, H. W. Newson, N. R. Roberson, E. G. Bilpuch and R. L. Walter, Fifth International Cyclotron Conference ed. R. W. Mellroy, (1969) 13.

M. E. Rose, Elementary Theory of Angular Momentum (John Wiley and Sons, Inc., New York, 1957).

E. Rost, Phys. Rev. 154 (1966) 994.

R. R. Roy and B. P. Nigam, Nuclear Physics, Theory and Experiment (John Wiley and Sons, Inc., New York, 1967).

G. R. Satchler, Annals of Physics, 3 (1958) 275.

G. Scheklinski, U. Strohbusch, and B. Goel, Nucl. Phys. A153 (1970) 97.

G. W. Schweimer and H. Rebel, des Zyklotron-Laboratoriums (1970) (unpublished)

T. Tamura, Revs. Mod. Phys. 37 (1965) 679.

T. Tamura, ORNL report no. 4152 (1967).

T. Tamura, D. R. Bes, R. A. Broglia and S. Landowne, Phys. Rev. Lett. 25 (1970) 1507.

T. Tamura, private communication (1971).

W. J. Thompson, unpublished lecture notes (1969).

W. J. Thompson, private communication (1971).

H. R. E. Tjin A Djie, K. Mulder, F. Udo, A. Groenefeld, L. A. Ch. Koerts, A. D. Hill and P. E. Hodgson, Nucl. Phys. A106 (1968) 85.

V. H. Webb, unpublished Ph.D. thesis, Duke University, 1968.

T. Y. Wu and T. Ohmura, Quantum Theory of Scattering (Prentice-Hall, New York, 1962)

S. Yoshida, Phys. Rev. 123 (1961) 2122.

R. W. Zurmuhle and C. M. Fou, Nucl. Phys. A129 (1969) 502.

BIOGRAPHY

Ronald O. Nelson

Personal:	Born September 1, 1945, Mechanisberg, Pennsylvania
	Married; Two Daughters
Education:	B. S. in Physics and Mathematics, Florida State University (1967)
Positions:	NDEA Fellow, Duke University, 1967-1970 Research Assistant, Duke University, 1970-1971
Membership:	Phi Beta Kappa

Abstracts:

1. A Particle-Identification Method with an On-Line Computer (with J. M. Joyce, W. S. McEver, R. V. Poore and N. R. Roberson) Bull. Am. Phys. Soc. 15 (1970) 598.

2. Measurements of Spectroscopic Factors in the $^{24}Mg(d,t)^{23}Mg$ and $^{24}Mg(d,^{3}He)^{23}Na$ Reactions (with N. R. Roberson and R. A. Hilko) Bull. Am. Phys. Soc. 16 (1971) 621.